CARDIFF UNIVERSITY

Cardiff Catalysis Institute, School of Chemistry

MPhil Research Dissertation

Characterisation and catalytic testing of heteropoly acids on porous silica supports

Christopher Jones

Supervisors: Dr Karen Wilson and Prof Adam Lee

Mentor: Prof Gary Attard

Period of research: October 2011 to December 2012

DECLARATION

This work has not been submitted in substance for any other degree or award at this or any other university or place of learning, nor is being submitted concurrently in candidature for any degree or other award.

Signed …… Date ……

STATEMENT 1

This thesis is being submitted in partial fulfillment of the requirements for the degree of Master of Philosophy (MPhil).

Signed …… Date ……

STATEMENT 2

This thesis is the result of my own independent work/investigation, except where otherwise stated. Other sources are acknowledged by explicit references. The views expressed are my own.

Signed …… Date ……

STATEMENT 3

I hereby give consent for my thesis, if accepted, to be available for photocopying and for inter-library loan, and for the title and summary to be made available to outside organisations.

Signed …… Date ……

Acknowledgements

I would like to thank Prof Adam Lee, Dr Karen Wilson and colleagues for welcoming me into their group, offering technical help and useful discussions, and generally creating a friendly working environment. I am particularly grateful to Dr Chris Parlett and Mark Isaacs, who provided invaluable assistance in using the laboratory equipment; and to Clare Morton, Vicky Bemmer, James Graham, Lee Durndell and Emily Douglas, for their useful advice and support throughout the project.

Thanks must also be extended to researchers at the Rutherford Appleton Laboratory, Harwell, for their assistance in TEM work; and to Dr Pramod Kerai and colleagues at Surface Measurement Systems, Alperton, for providing our group with an inverse gas chromatography (IGC) system and training in its operation. Finally, I would like to express my gratitude to the Engineering and Physical Sciences Research Council (EPSRC) for providing funding for this project via a Leadership Fellowship awarded to Prof Lee.

Research summary

The aim of this investigation was to rationalise the catalytic activity of heteropoly acid $H_3PW_{12}O_{40}$ (HPW) on porous silicas. To avoid leaching, activities were evaluated for a reaction involving non-polar reagents: the isomerisation of neat alpha-pinene. Activities were found to depend on the nature of the support: per unit mass, the mesoporous silicas SBA-15 and KIT-6 deliver higher rates of conversion than fumed silica at HPW concentrations below 50 wt.%, but become less effective at higher loadings. These trends were attributed to changes in porosity, as thermogravimetric analysis and inverse gas chromatography studies showed little variation in silanol density or hydrophobicity.

For each catalyst, the density of HPW crystallites was measured by powder X-ray diffraction; their loading, by energy-dispersive X-ray spectroscopy; and the pore volume and area, by nitrogen porosimetry. From these values, an estimate was obtained for the support area rendered inaccessible by pore blocking. When normalised for accessibility and support area, reaction rates were found to be independent of the support at loadings below 40 wt.%. The plots appear linear, with gradients corresponding to a turnover frequency (expressed per quantity of accessible catalyst) of 1700 mol mol_{HPW}^{-1} h^{-1}. Thus, the activity of HPW on these and similar supports should be predictable from loading and porosimetry measurements alone. Catalyst particle growth appears not to affect accessibility, suggesting that most HPW exists as monolayer deposits. Further evidence for such structures is supplied by the strong “interfacial” W 4f signals in X-ray photoelectron spectra of the catalysts, representing HPW in direct contact with the support.

Studies were also undertaken to assess the suitability of the catalysts for biodiesel synthesis. UV-vis and EDX measurements showed near-total leaching of HPW in methanol under typical reaction conditions. However, exchanging a fraction of protons for caesium ions almost totally prevented leaching, with only partial loss of catalytic activity.

Contents

1. Introduction

1.1 Heteropoly acid (HPA) catalysts

Heteropoly acids (HPAs), such as 12-phosphotungstic acid ($H_3PW_{12}O_{40}$, HPW), have been utilised as catalysts in a range of industrially important processes.[1] HPAs are stronger acids than conventional catalysts such as H_2SO_4 (Table 1), as they incorporate the conjugate anion of an inorganic acid within a neutral metal-oxide cage, which distributes the anion charge over a larger area.[2] For example, HPW incorporates a phosphate ion in a tungsten(VI) oxide cage, sharing a small formal charge (3-) over an external surface of 52 atoms.

Acid	HOAc	CH_3CN			$(CH_3)_2CO$			C_2H_5OH		
	pK_1	pK_1	pK_2	pK_3	pK_1	pK_2	pK_3	pK_1	pK_2	pK_3
$H_3PMo_{12}O_{40}$	4.68	–	–	–	2.0	3.6	5.3	1.8	3.4	5.3
$H_4SiW_{12}O_{40}$	4.87	1.9	5.9	7.9	2.0	3.6	5.3	2.0	4.0	6.3
$H_3PW_{12}O_{40}$	4.70	1.7	5.3	7.2	1.6	3.0	4.1	1.6	3.0	4.1
CF_3SO_3H	4.97	5.5	–	–	2.7	–	–	–	–	–
HNO_3	–	–	–	–	3.6	–	–	3.6	–	–
HCl	8.40	–	–	–	4.0	–	–	–	–	–

Table 1 Acid dissociation constants for HPAs and other acids at 25°C, from ref. 2.

HPW is an example of the most stable form of HPA, the Keggin structure.[3] First proposed by J. F. Keggin in 1934,[4, 5] this compound comprises the tetrahedral oxide of a heteroatom such as phosphorus, silicon or germanium encapsulated within an oxide cluster of electron-poor transition metals such as tungsten and molybdenum. Other HPAs are similar in structure but larger, comprising two or more heteroatoms (Fig. 1). It is also possible to produce HPAs in which one or more of the metal atoms in the cage are substituted for atoms of a different element, reducing the symmetry of the cage.[6]

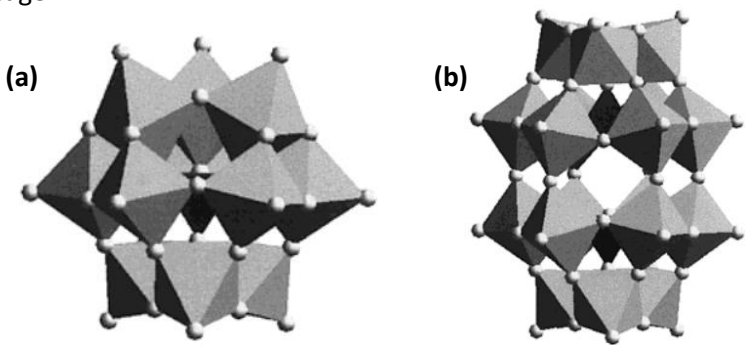

Fig. 1 (a) Keggin and (b) Dawson units, from ref. 3. Octahedra represent metal oxide units. Protons and the central heteroatom-oxide moiety are not shown.

HPAs are readily soluble in polar solvents and may thus be employed as homogeneous catalysts for liquid-phase processes, including alkene hydration, esterification and polymerisation reactions.[1, 7-9] Indeed, HPAs frequently deliver competitively high reaction rates, yields and selectivities, and may even generate products not accessible via other acid-catalysed routes, as in the synthesis of diphenylmethane from benzene and formalin.[10] Though decomposition occurs in some solvents at pH values above 2, dissolved HPAs in highly acidic solutions are typically stable for several years and are easily recycled.[11] In contrast, conventional inorganic acids such as H_2SO_4 must be separated and recycled by means of wasteful extraction processes involving expensive ion-exchange resins, large volumes of solvent and additional reagents that may degrade sensitive products.[12]

The solubility of HPAs in polar solvents is a significant obstacle to their application as heterogeneous catalysts.[13] A common solution is to replace a proportion of the protonated sites with cations such as Cs^+,[14-16] NH_4^+ [16] and Ag^+,[17] generating insoluble salts with some acid groups remaining for catalysis.[18] It has been postulated that the large guest cations are substituted in place of similarly sized $[H_5O_2]^+$ species,[19] which have been shown by infrared,[20, 21] neutron scattering[22, 23] and NMR analysis[24] to exist between Keggin units and act as intermediaries for proton transfer (Fig. 2). Salt formation typically leads to aggregates smaller than those in the pure acid, yet a high concentration of surface acid sites is retained due to localisation of protons in an outer shell of pure HPW.[25, 26] Thus, partial salts of HPW can exhibit greater activities than the pure acid, despite possessing fewer bulk acid sites. It should be emphasised that only certain cations produce enhance activity in this way: ions with small radii, such as K^+, typically yield large particles with high solubility.[17, 18]

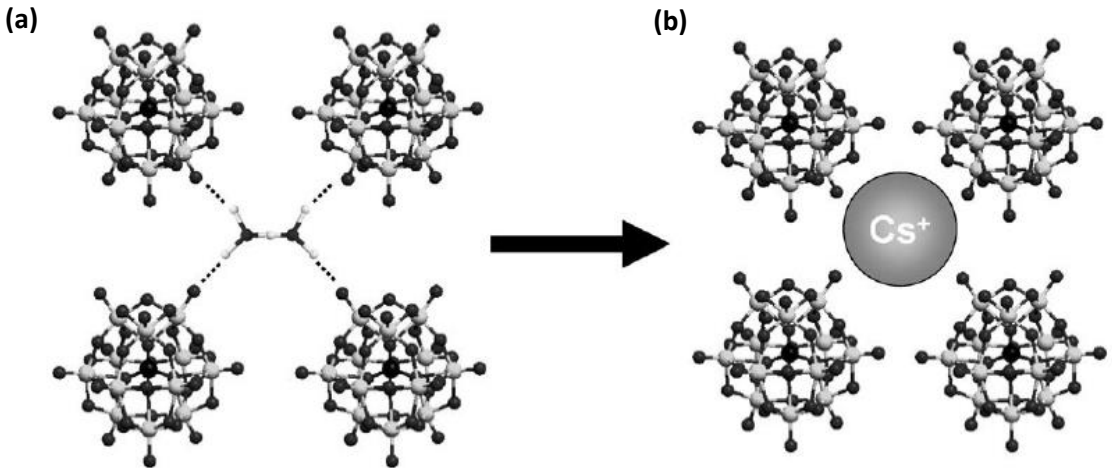

Fig. 2 Proposed substitution of $[H_5O_2]^+$ ions in crystalline HPAs (a) by caesium ions (b), from ref. 19.

For a material to function effectively as a heterogeneous catalyst, a large proportion of its catalytic sites must be accessible to reagents. Unfortunately, both HPAs and partial salts of HPAs exhibit low

surface areas (< 50 m^2g^{-1}), so a large proportion of the acid sites in these materials are unavailable for surface reactions.[16] In the caesium salts, mesopore and crystallite size may be improved by careful choice of impregnation conditions, caesium precursor and caesium/HPW ratio,[15, 27] but even the maximum surface area enhancements are modest (80-120 m^2g^{-1}). To harness HPAs as competitive heterogeneous catalysts, a means of reducing particle size and increasing surface area must be found.

1.2 Supported catalysts

To improve the accessibility of acid sites, HPW or its salts may be dispersed over support materials with higher surface areas and larger, more ordered pores. Use of supports may additionally increase the stability of the catalyst; reduce leaching; improve cost-effectiveness by augmenting the activity of the catalyst per unit mass; and provide a more or less hydrophobic surface for differential binding of reagents and products. In some situations, HPAs may also be usefully added to a support to enhance the activities of other catalytic species; for example, a study of silica-supported rhodium and manganese catalysts for syngas conversion showed that doping with certain HPAs leads to increased conversions and selectivities.[28]

Mesoporous supports are commonly obtained by hydrothermal treatment of natural minerals such as zeolites.[29] However, the pores of such materials are typically small (< 5 nm) and variable in size, and are therefore a poor choice for supporting Keggin units (diameter 1.2 nm). Large pore diameters are especially necessary if a catalyst is to be applied to reactions involving large molecules, as efficient diffusion requires that pores be significantly wider than the mean free path of the diffusing molecules.[30-32]

More ordered and tuneable pore networks can be achieved through direct synthesis, utilising cylindrical or laminar micelles as templates[33, 34] (Fig. 3). The earliest known and best studied ordered mesoporous materials are silicas such as SBA-15,[35] formed by acid-hydrolysis of aqueous sodium silicate or tetraethoxysilane in the presence of Pluronic P-123, a tri-block copolymer surfactant. Exhibiting hexagonally packed one-dimensional channels 5 – 12 nm in diameter, surface areas of 700 – 1200 m^2g^{-1} and pore volumes of 0.7 – 1.2 $cm^3\ g^{-1}$,[35] this material is a useful as a catalytic support even for reactions involving bulky substrates. Alternative supports with differently shaped or connected pores have also been achieved. For example, conducting the hydrolysis with P-123 in a water-butanol mixture yields KIT-6, a material with three-dimensional networks of channels.[36]

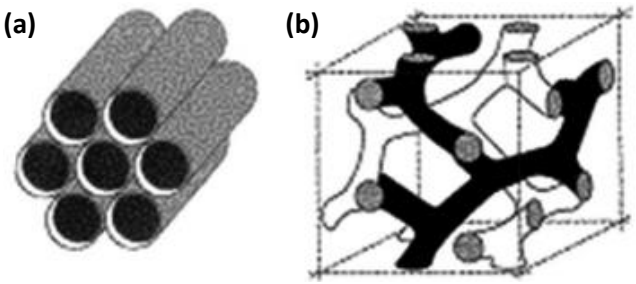

Fig. 3 Schematic representations of the pore structures in (a) SBA-15 and (b) KIT-6, adapted from ref. 34.

Studies of HPAs on mesoporous silicas have indicated that adsorption onto the support significantly reduces leaching in polar media.[37] Binding likely occurs as an ionic interaction between Keggin anions and protonated silanol groups on the silica surface, which subsequently act as proton donors for acid-catalysed reactions. As HPA loading is increased, a monolayer of the catalyst is formed on the silica, with crystallisation of bulk HPA in the pores only at high loadings[38, 39] (typically above 30 wt.%; Fig. 4). Though the rates of reactions involving small, polar reagents may increase with multilayer HPA deposition, reactions of bulky and non-polar substrates typically proceed at a maximum rate when a single layer of supported Keggin units is present on the support surface. It should be noted that catalytic performance may be influenced by a number of other factors. For example, low loadings of HPW on silica have been found to be hydrothermally unstable, whereas acid strength,[40] pore blockage and susceptibility to leaching all increase with loading. Varying the solvent used in impregnation of the support or exposing the catalyst to calcination treatments may also affect the structure and properties of HPW deposits.[41]

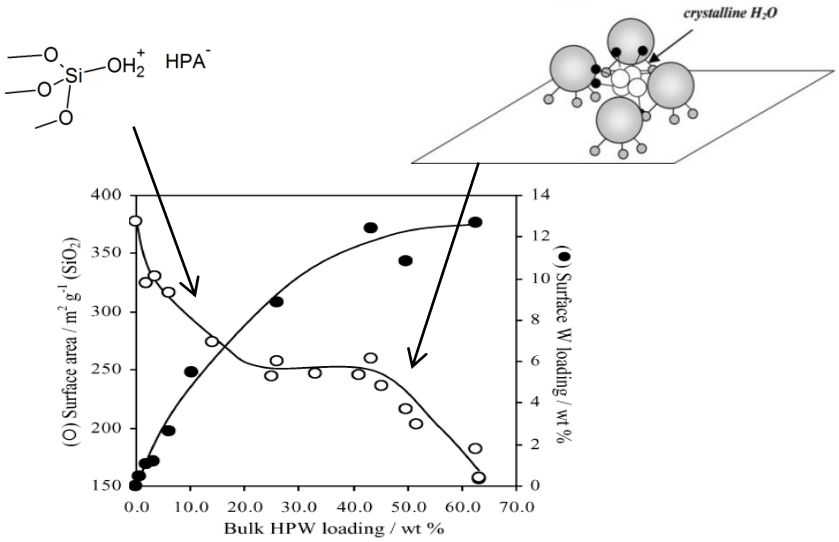

Fig. 4 Variation of surface area and coverage with bulk HPA load on fumed silica, adapted from ref. 38. Data from porosimetry and X-ray photoelectron spectroscopy (XPS) are shown, with schematic representations of the proposed catalytic species at low and high loadings.

Though silica-supported HPAs have demonstrated high activities for a range of processes, leaching in polar media is a persistent obstacle to their commercial use. Susceptibility to leaching correlates approximately with the isoelectric point of the support: silica, a relatively acidic material, exhibits a weak interaction with HPAs, whereas more basic materials such as titania, alumina, zirconia and even activated carbon are relatively strongly binding.[42] However, the large pore sizes and surface areas of mesoporous silicas are relatively difficult to reproduce in other materials, and highly basic supports have also been found to deactivate HPAs by destabilising the Keggin anion.[43]

To reduce leaching in silica supports, the material may be modified by addition of species to which HPAs can bind more strongly. For example, the pore surface can be functionalised with propylamine moieties, which are more basic than free silanol groups;[44] or coated with nanoparticles of other support materials, such as zirconia.[45] Functional groups may also be added to tune properties such as hydrophobicity, acidity or redox activity (Fig. 5).[46] However, such modifications usually reduce the surface area and pore size of the catalyst, obstructing transport and adsorption of bulky substrates.

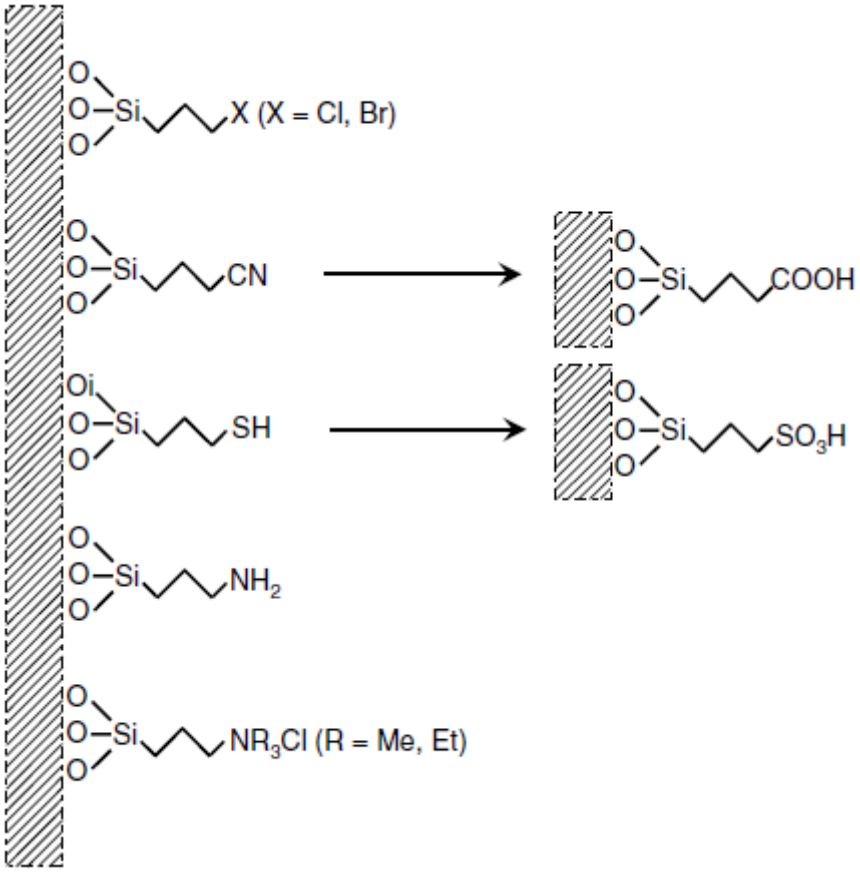

Fig. 5 Potential functional groups that may be added to silica surfaces, from ref. 46.

One strategy to reduce leaching without blocking pores is to synthesise the support in the presence of HPA, such that the catalytic species becomes incorporated into the pore wall. Silica-HPA

composites have been shown to effectively catalyse cracking and esterification reactions involving large molecules such as benzoic acid, tert-butanol and 1,3,5-triisopropylbenzene,[47] and in one study exhibited three times the activity of a homogeneous HPA catalyst.[48] Formation of SBA-15-type frameworks in the presence of HPAs has also been shown to occur more rapidly than the conventional synthesis and result in a structure with greater hydrothermal stability and surface area.[49] However, it is often challenging to predict and optimise the structures of co-precipitated catalysts: for example, Dufaud *et al*. found that silica-encapsulated HPW catalysts must be stabilised by calcination (Fig. 6).[48] Furthermore, the effective loadings of such materials are likely to be relatively low, since a substantial fraction of catalytic sites are contained in the bulk of the support and thus inaccessible to reagents.

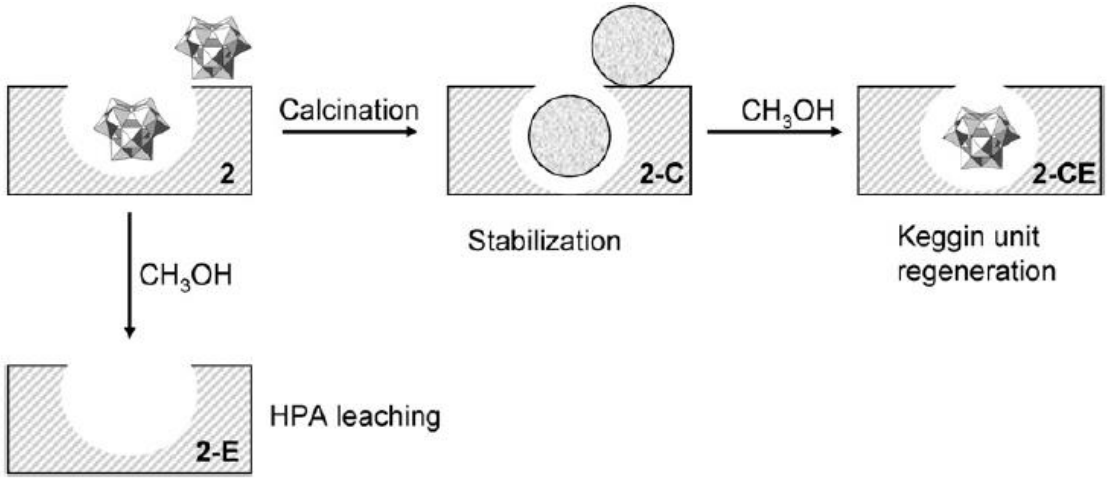

Fig. 6 A reported procedure for the preparation of silica-encapsulated HPA catalysts, indicating the importance of the calcination step for prevention of HPA leaching. Image is reproduced from ref. 48.

As in the bulk compounds, using partial salts in place of fully protonated HPAs should also improve stability to leaching. Since fully protonated HPAs on silicas already exhibit high surface areas and reduced solubilities, maximum activities might be expected at lower metal loadings than are needed in the bulk HPA. Indeed, recyclable supported HPA catalysts have been produced not only with large cations such as caesium,[15, 50] but also with smaller cations such as magnesium and aluminium, which give readily soluble HPA salts in the absence of a support.[51] HPA salts have been supported on a variety of materials and implemented effectively in both acid-base and redox processes,[52] yet the exact interactions between the cation, Keggin anion and support remain unclear.

1.3 Development of catalysts for biodiesel synthesis

Fuels derived from renewable biological feedstocks have attracted strong interest as sources of energy for industry and transport. In the light of the decreasing availability of fossil fuels and

growing concerns as to their environmental impact, European governments have committed to replacing at least ten percent of conventional transport fuels with renewable alternatives by 2020.[53] While large-scale production of biofuels has begun,[54] there is a need to develop production methods with reduced cost and environmental impact, and to avoid competition for food crops by enabling the utilisation of non-edible feedstocks.[55]

The original aim of this project was to develop supported HPA catalysts for biodiesel synthesis. Conventional biodiesels consist of fatty acid methyl or ethyl esters.[56] Such esters are synthesised either by direct esterification of free fatty acids (FFAs) or by transesterification of natural glycerol esters, primarily triglycerides (Fig. 7). Transesterification is effected most readily by base catalysis, but the presence of FFAs can lead to catalyst deactivation and soap formation.[57] Thus, commercial biofuels are usually generated by a two-step process: initially, FFA esterification with methanol or ethanol in the presence of an acid such as HCl, then remaining glycerides are transesterified in the presence of a base such as NaOH or NaOMe.[58]

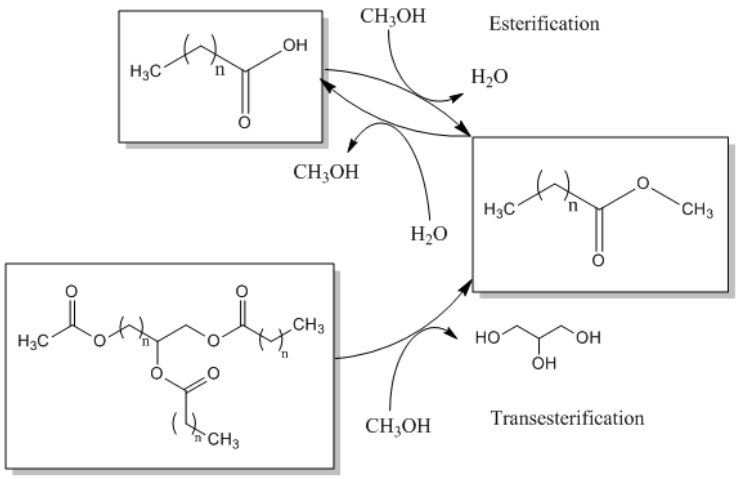

Fig. 7 Reaction schemes for esterification and transesterification. The long-chain saturated carboxylic acids shown represent one of many classes of fatty acid; n denotes the number of methylene units in the chain, typically between 6 (caprylic acid) and 24 (cerotic acid). Note that the product esters may be hydrolysed by water, so solid catalysts with more hydrophobic surfaces are likely to deliver higher yields.

Homogeneous catalysis, involving acids or bases dissolved in the reacting alcohol, carries a number of drawbacks. The catalyst must be continuously added, and soap and other neutralisation products must be removed by multiple washing and separation steps. Moreover, glycerol, a major by-product of transesterification, is often difficult to purify after the homogeneous process, so cannot be commercialised to offset the cost of biofuel production.[59] In contrast, heterogeneous catalysts can be readily separated from the reaction mixture and reused, or even employed in a continuous,

packed bed process.[60] Soap formation does not occur and the resulting fuel is easier to separate, so the cost of purification and water effluent load is reduced. Finally, glycerol from the reaction is of a usefully high grade. Though heterogeneous processes often require higher temperatures and pressures, and a larger methanol-to-oil ratio than homogeneous methods, the use of solid-state catalysts nonetheless offers the potential for simpler, cheaper and less wasteful biofuel production.

Like their homogeneous counterparts, solid-state base catalysts exhibit substantially higher activities for transesterification reactions than the alternative acid catalysts.[61] For this reason, most current research focuses on this type of catalyst. However, heterogeneous bases are readily deactivated in the presence of FFAs, so feedstocks must still be subjected to an initial pre-treatment step involving acid-catalysed esterification.[62] Solid-state acid catalysts, though generally less active, offer the advantage of tolerating even low-quality feedstocks with high concentrations of FFAs, and effect esterification and transesterification processes simultaneously.[63] Economical assessments have indicated that of all the potential biofuel manufacturing routes, heterogeneous acid-catalysis involves the simplest infrastructure, lowest capital investment and highest rate-of-return.[64, 65]

HPAs on silica have previously been reported as effective heterogeneous acid catalysts for biodiesel production,[37, 66-68] but results in this and other studies[41] suggest that extensive leaching of HPW occurs under typical esterification reaction conditions (section 3.8). Thus, to evaluate the activities of supported HPAs operating purely as heterogeneous catalysts, a reaction involving only non-polar reagents was investigated: the solvent-free isomerisation of alpha-pinene, a bridged cyclic hydrocarbon.[38, 69-72] Under acidic conditions, alpha-pinene is converted to other polycyclic compounds camphene and beta-pinene; monocyclic compounds limonene, para-cymene, terpinolene and alpha- and gamma-terpinenes; and assorted oligomers formed by alkene-alkene coupling (Fig. 8). Camphene and limonene are the major products initially, but other products become increasingly abundant as the reaction progresses. Since strong acids favour formation of monocyclic species, the selectivities of catalysts may be used to gauge the strengths of their acid sites.[40, 70]

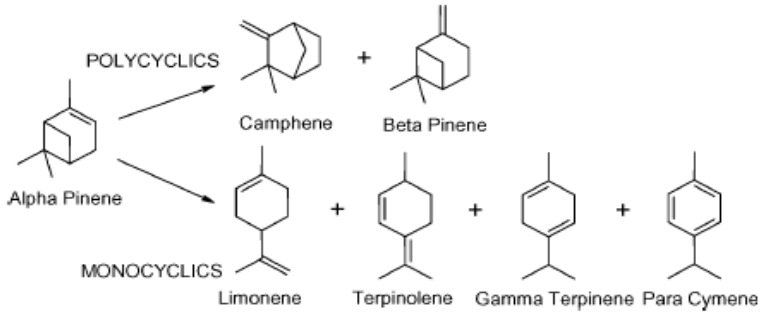

Fig. 8 Major products of alpha-pinene isomerisation, from ref. 38.

Studies by Newman *et al*., focussing on HPW supported on fumed silica, have shown that conversion of alpha-pinene scales approximately with the proportion of HPW interfacing directly with the support[38, 69] (Fig. 9). The latter quantity was measured by X-ray photoelectron spectroscopy (XPS, section 3.5). Conversions also correlated strongly with the concentration of accessible surface acid sites, gauged by combining porosimetry and ammonia titration data. Thus, maximum conversions were obtained near the loading at which monolayer formation reaches completion (approximately 40 wt.%). Similar trends might be expected for conversion of FFAs and triglycerides to biodiesel: like the alpha-pinene reaction, these processes involve bulky, largely non-polar substrates which can only access surface acid sites in HPW deposits, so activity should begin to fall when multilayer deposition becomes significant.

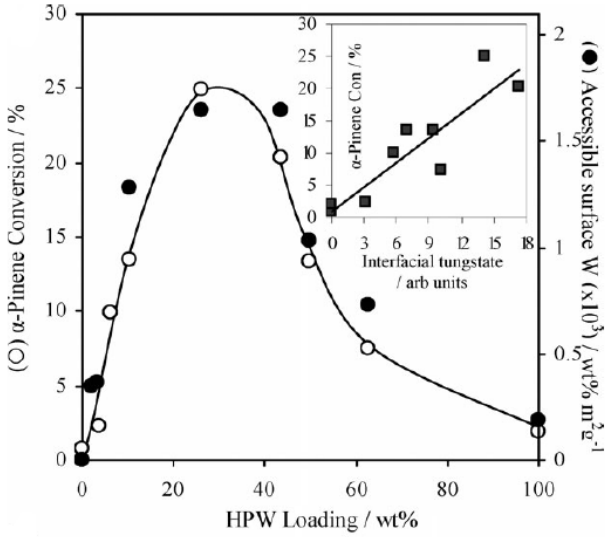

Fig. 9 Variation of activities and accessible surface sites with loading, from ref. 38.

Acid-catalysed isomerisation of alpha-pinene is a useful proxy for investigating the potential usability of supported HPW catalysts for biodiesel synthesis. Since neat reagent is used, high conversions are easily achievable even using catalysts with low activity, and the absence of leaching allows the observed activities to be attributed entirely to heterogeneous catalysis. Data obtained from this reaction may not exactly reflect the behaviour of catalysts when applied to biodiesel synthesis; however, the observed trends provide a useful starting point for explaining variations in activity towards more complicated processes such as esterification, in which phenomena such as leaching and redistribution of HPW may be significant.

1.4 Effects of pore blocking on catalytic activity

Materials with mesoporous frameworks, such as SBA-15 and KIT-6, are favoured as catalytic supports due to their large surface areas.[73] Dispersing an active species over a larger area allows it to be deposited in the form of smaller particles or thinner layers, rendering more catalytic sites

accessible to reagents. Unfortunately, enclosed pores with large surface areas are often narrow, and therefore easily blocked by excess support deposits,[74] damage to the pore wall[75] or solid reaction products.[76, 77] A particularly common problem is the formation of coke, a carbonaceous deposit, during reactions involving hydrocarbons. This process, known as coking, dramatically lowers the activity of the afflicted catalyst by blocking active sites and restricting diffusion through the support.[78-80]

Pores may also be blocked by the catalytic particles themselves. An obstruction is especially likely if, as in this study, the size of the catalytic species is similar in magnitude to the radius of the pore. Other factors that favour blocking are a high catalyst loading; enlargement of catalytic particles during reaction; and a lack of strong interactions with the support, to facilitate high dispersions.[81] Pore blocking is often unavoidable, but may be mitigated by careful experimental design: for example, Bonne *et al*. found that nanoparticles of titania (anatase) on SBA-15 are more highly dispersed if they are prepared from a more dilute precursor solution and calcined at a low temperature (Fig. 10).[82]

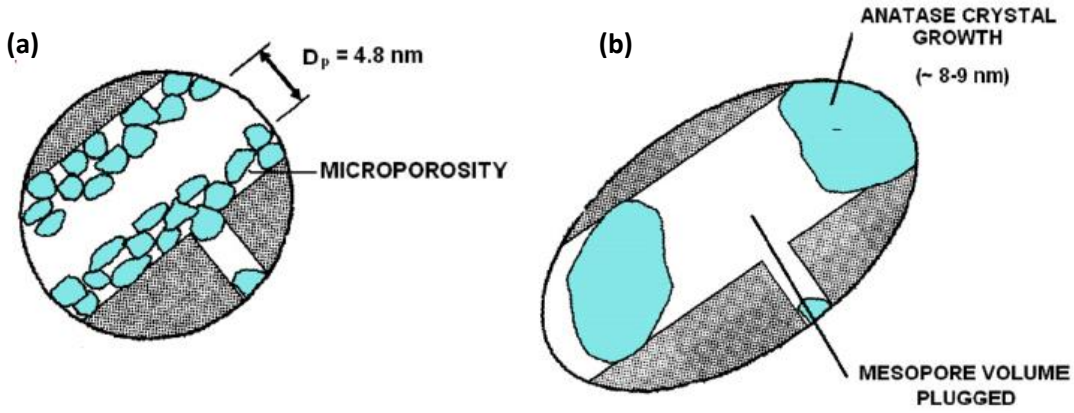

Fig. 10 Representations of pore blocking in SBA-15 by titania nanoparticles, adapted from ref. 82. The different structures were achieved by impregnation of the support with a titania precursor followed by calcination at (a) 400°C or (b) 600 – 800°C. D_P denotes the mean pore diameter after impregnation.

Porosimetry (section 3.4) is the main technique for investigating changes in the accessibility of pores.[83] Normally, ordered mesoporous materials exhibit a type-IV absorption-desorption isotherm with significant hysteresis. Barrett-Joyner-Halenda (BJH) analysis of the data typically indicates that pore sizes are narrowly distributed and unimodal. However, if pores become constricted, two or more "steps" may be observed in the isotherm, and the distribution of pore sizes is likely to be wider with a greater number of peaks (Fig. 11).[74] It should be noted that for a given adsorbate, there exists a fixed pore radius below which desorption occurs spontaneously, rather than in response to changes in pressure. As a result, highly constricted pores may not noticeably alter the shape of a

desorption isotherm. This detail was highlighted in a study by Eggenhuisen *et al.*: nickel oxide particles on mesoporous silica supports (SBA-15 and MCM-41) displayed the hallmarks of pore blocking in porosimetry experiments using argon, but appeared unblocked when nitrogen was used.[84]

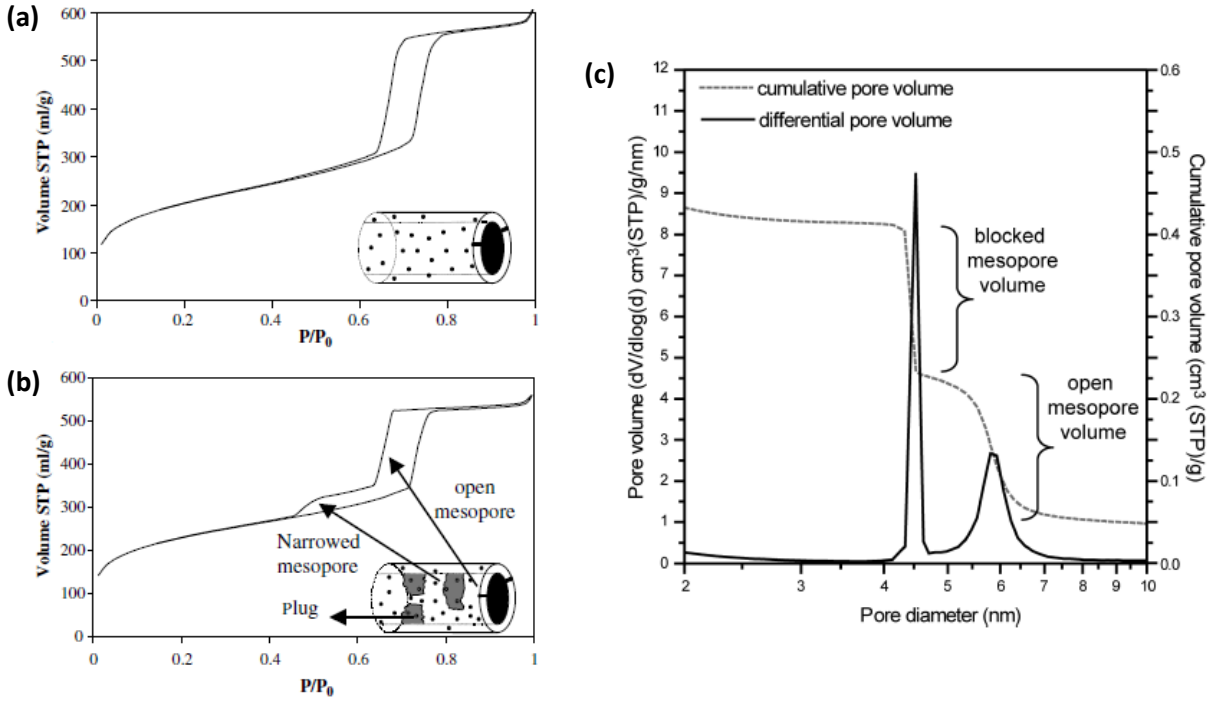

Fig. 11 Nitrogen physisorption isotherms and schematic diagrams of SBA-15 materials (a) with and (b) without pore blocking, from ref. 74. The plot (c) is the BJH pore size distribution for a typical blocked SBA-15 support, from ref. 84.

A more esoteric method for investigating blocking effects is to measure the freezing and melting temperatures of intraporous water by differential scanning calorimetry (DSC).[84, 85] Water outside pores freezes at the usual temperature of 0°C and, once frozen, may induce freezing of water in large adjacent pore spaces by heterogeneous nucleation. In smaller and less accessible pores, however, freezing occurs at much lower temperatures. The freezing point falls with decreasing pore radius, and this radius can therefore be estimated from the DSC thermogram by means of a calibration curve. In some cases, differences between freezing and melting temperatures may also provide an indication of whether pores are linear or bent.[86] DSC can provide information not accessible by porosimetry experiments, but its sensitivity is limited: the freezing point of water cannot be depressed indefinitely, so pore sizes below a particular value (approximately 4 nm for silicas) cannot be distinguished.

Attempts have been made to use both porosimetry and DSC to quantify the degree of pore blocking. In DSC, the mass of water frozen is estimated by integrating the heat flow trace and dividing by the heat of fusion. The volume of pores within a given range or radii can then be calculated using the density of water at the corresponding temperatures. This method, often termed thermoporometry, is a useful complement to BJH analysis, but cannot serve as a true measure of pore blocking since only pores occupied by water are accounted for. Although reliable results can be achieved with precautions to maximise sample soaking, minimise drying and avoid noise in the DSC thermogram, it is not possible to add water to pores which are completely encapsulated by blockages, or even to ensure that all accessible pores are filled without cavitation.

A more common measure of pore blocking is the loss of surface area arising from deposition of catalyst. Adsorption isotherms are obtained for both the supported catalyst and the pure parent support, and the surface areas per unit mass estimated by the Brunauer-Emmett-Teller (BET) method. The catalyst surface area, S_{cat}, is normalised to the mass of support by dividing by *(1-y)*, where *y* is the measured fractional loading of catalyst by weight (section 3.3). Finally, the normalised catalyst surface area is divided by the surface area of the support, S_0 (Eq. 1). The resulting value, often termed the normalised surface area (*NSA*),[84, 87-90] is an estimate of the fraction of support surface that remains accessible in the catalyst.

$$NSA = \frac{S_{cat}}{(1-y)S_0} \qquad \text{(Eq. 1)}$$

Catalyst particles in a pore may reduce the observed surface area by forming an overlayer, which reduces the effective radius of the pore, or sealing off a section of unoccupied space, so that it is no longer accessible to adsorbates. At the same time, particles contribute to the observed area by providing an additional surface, which may differ in roughness or curvature to the covered substrate.[89, 91] Unfortunately, the equation for *NSA* does not explicitly account for any of these effects, so it can only deliver a reasonable measure of pore blocking in systems where catalyst particles contribute negligibly to the surface area. If the catalyst loading is high, *NSA* values become difficult to interpret.

To better explain changes in surface area, some researchers have developed simple, quantitative models of catalyst deposition. One approach is to assume that the pore is cylindrical with radius R_1, and that a catalyst uniformly coats its surface such that the radius decreases to R_2 (Fig. 12).[87] In this "corona model", the length of the pore is preserved, so *NSA* can be equated to the ratio of radii R_2/R_1. The values R_1 and R_2 can be measured by porosimetric analysis of the pure support and supported catalyst, and R_2 can also be estimated geometrically from the loading and density of the

catalyst. The model may thus be deemed appropriate if, firstly, the expected and measured R_2 values agree; and, secondly, R_2/R_1 is equal to the estimate of *NSA* from BET analysis.

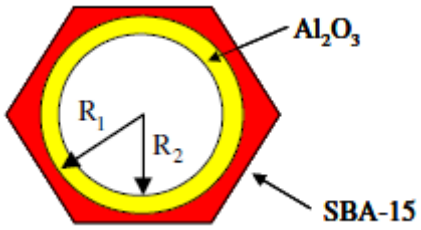

Fig. 12 "Corona model" of catalyst deposition in mesopores, from ref. 87.

In practice, simple models of catalyst deposition rarely produce accurate predictions, as they do not account for surface corrugation, variations in particle geometry or plugging of pores. Indeed, a number of studies have shown real catalyst deposits to be highly complex. For example, when Friedrich *et al*. examined 299 nickel oxide nanoparticles in single SBA-15 channels by transmission electron microscopy (TEM), particle sizes and spacing were found to obey the expected log-normal distributions.[92] However, nanoparticle densities in small channel sections were highly heterogeneous, with local loading variations exceeding 100% of the average bulk loading (Fig. 13). Similarly, Janssen *et al*. found that gold and zirconia nanoparticles on SBA-15 produce two-step isotherms in nitrogen porosimetry due to the co-existence of filled and empty pores.[93]

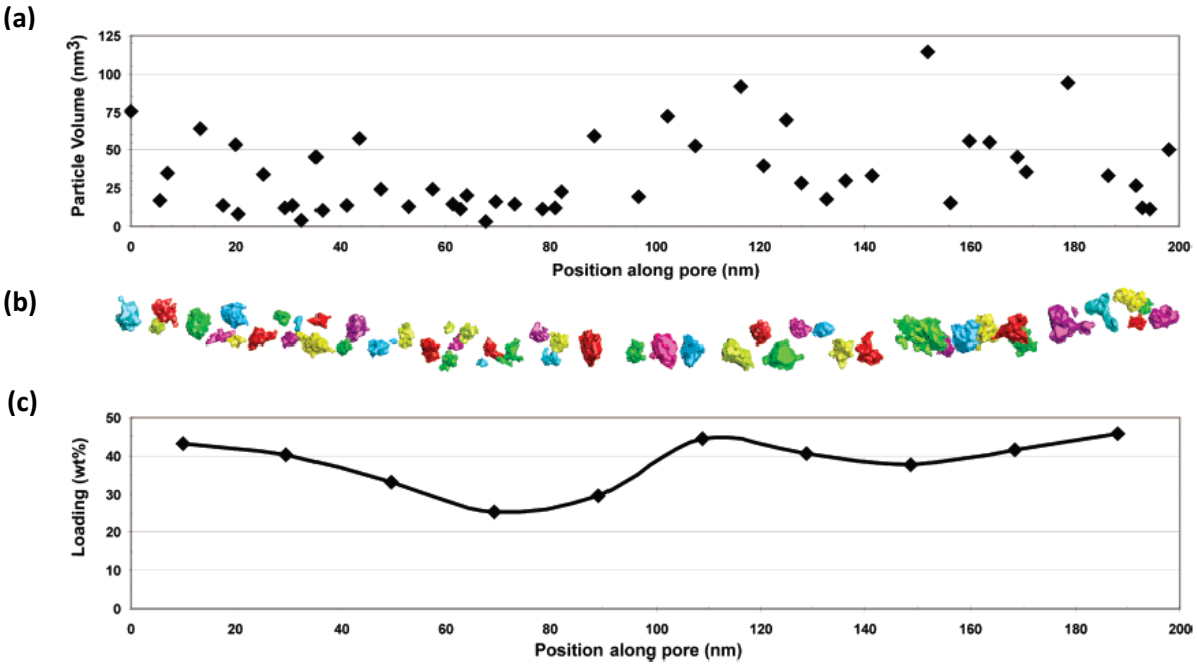

Fig. 13 TEM estimates of the (a) volumes, (b) shapes and (c) local loadings of nickel oxide nanoparticles in a single channel of SBA-15, from ref. 92.

The heterogeneity of in-pore deposition has also been observed in DSC studies. In one notable study, Eggenhuisen *et al*. found that nickel oxide nanoparticles in SBA-15 produce a DSC thermogram with two well-defined peaks: one representing pores that are open and accessible, and another representing pores heavily blocked by the guest material (Fig. 14).[84] TEM studies further indicated that nanoparticles are deposited with two different morphologies, which exhibit very different pore blocking behaviours even when present in identical concentrations.

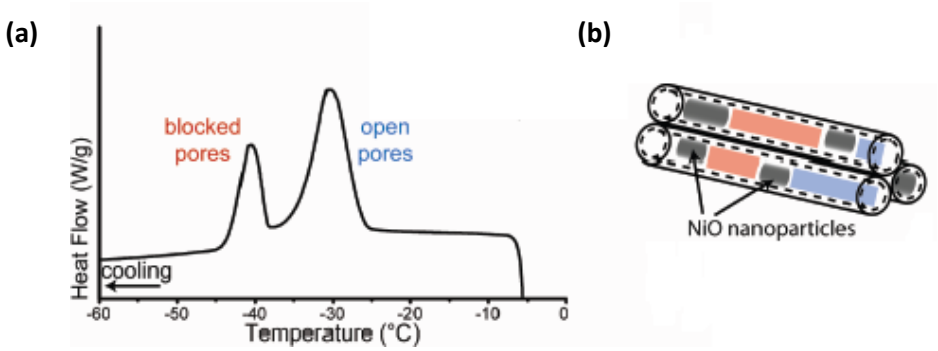

Fig. 14 (a) DSC thermoporometry trace and (b) schematic representation of nickel oxide nanoparticles in SBA-15, adapted from ref. 84. Red regions in the schematic represent inaccessible pores.

Some of the complexity of catalyst deposition may be probed experimentally. The effect of corrugation, for instance, can be gauged by comparing the BET area, a fully empirical measurement, with the area estimated from the Kruk-Jaroniec-Sayari (KJS) model, which assumes smooth, cylindrical pores.[89] It is also possible to determine the areas of some catalyst particles by extensive TEM studies[92] or, in some cases, titration with a strongly binding absorbent.[38, 94, 95] All of these techniques, however, are of limited use in quantitative analyses: failure of the KJS model could be variously attributed to surface roughness or non-cylindrical pore geometries; the accuracy of TEM analysis is diminished by small sample sizes, poor resolution at the scale of nanoparticle surfaces and a bias towards larger particles; and titration measurements may only provide an estimate of catalyst area if the adsorbate interacts exclusively at the nanoparticle surface and exhibits well-defined coverage.

The difficulties associated with area-based models of pore blocking can largely be bypassed by focussing instead on changes in pore volume. A common volume-based estimate of pore blocking, the normalised pore volume or *NPV*,[84, 89] is analogous to the aforementioned *NSA* calculation (Eq. 1):

$$NPV = \frac{V_{cat}}{(1-y)V_{sup}} \qquad \text{(Eq. 2)}$$

V_{cat} and V_{sup} are, respectively, the BJH pore volume estimates for the catalyst and pure support (expressed per mass of material), and *y* is the fractional catalyst loading by weight (section 3.3). *NPV* shares the limitations of *NSA*: volume occupied by catalyst in the pores is not explicitly accounted for, so the result of the calculation incorporates the effects of both pore filling and the creation of inaccessible voids. However, *NPV* values can be corrected far more easily, because the volumes of catalyst deposits are easily estimated from lattice parameter (section 3.2) and loading measurements (section 3.3). To the best of our knowledge, an expression for the corrected *NPV*, NPV_{corr}, has not been explicitly formulated prior to this work, although its form has been alluded to in previous studies.[84] A detailed derivation for NPV_{corr}, is supplied in section 3.4, and in section 3.7, the expression is utilised to account quantitatively for the differences in activity displayed by silica-supported HPW catalysts.

2. Experimental procedures

2.1 Instruments and reagents

All reagents were obtained from Sigma-Aldrich and used without further purification. The fumed silica selected for use as a support was the grade designated S5505, with a reported surface area of 200 ± 25 $m^2 g^{-1}$ and pore size of 0.2 – 0.3 μm (Sigma-Aldrich). Catalysts were prepared, and reactions conducted, using reagents of at least 98% purity and HPLC-grade solvents.

Energy-dispersive X-ray (EDX) spectra were obtained with an Oxford Instruments INCA Energy X-ray analysis system fitted to a Carl-Zeiss EVO-40 Scanning Electron Microscope (SEM), using the Oxford Instruments INCA software. Samples were supported on aluminium stubs backed with carbon tape. Focussing and centring of the electron beam were performed in the Carl–Zeiss SmartSEM software. An accelerating voltage of 25 kV and maximum beam current of 20 nA were used, with a fixed working distance of 9 mm. Spectra were calibrated against measurements on a pure cobalt standard, and recorded over an energy range of 0 – 20 keV, with 2K channels, a scan time of 200 seconds and 20 – 30% processing time. Typically, loadings were obtained as an average of six scans over areas of approximately 50 μm x 50 μm. Regions were selected randomly, but those containing very thick or irregular patches of material were excluded to minimise error.

X-ray photoelectron spectrometry (XPS) data were obtained using a KRATOS Axis Hsi Photoelectron Spectrometer fitted with a charge neutraliser and magnetic focusing lens employing Al K_α monochromated radiation (1486.7 eV). Spectral fitting was performed using CasaXPS version 2.3.14. Binding energies were corrected to the C 1s peak at 285 eV, and the peaks fitted using common Gaussian-Lorentzian peak shapes. The separation of W 4f doublet peaks was fixed at 1.43 eV, while the separation of the two detectable W environments was fixed at 2.1 eV. Full-width half-maxima (FWHM) were kept constant for each catalyst.

Low- and wide-angle powder X-ray diffraction (PXRD) patterns were recorded on a PANalytical X'pertPro diffractometer fitted with an X'celerator detector and Cu K_α (1.54 Å) source, and calibrated against a Si standard. Low-angle patterns were recorded for 2θ = 0.3 – 8° with a step size of 0.01°, and wide-angle patterns were recorded for 2θ = 10 – 70° with a step size of 0.02°. The average pore-wall thicknesses of pure SBA-15 samples were calculated from low-angle patterns via the Bragg equation, after zero-correction of the peak positions. In the wide-angle data, five consistently intense peaks were identified at ($h^2 + k^2 + l^2$) = 8, 10, 12, 22 and 50; HPA densities were calculated from the positions of these peaks, and volume-averaged particle sizes were also estimated by application of the Scherrer equation, with a constant correction of 0.15° for experimental line

broadening. The error in the Scherrer size was estimated as the standard error of the individual measurements for the selected peaks.

Transmission electron microscopy (TEM) was performed at the Research Complex at Harwell using a JEOL JEM-2011 TEM operating at 200 kV. The point resolution of the microscope is 1.9 Å, with a LaB_6 filament electron source. Images were recorded using a Gatan 974 CCD camera. The powder sample was dispersed in hexane and a drop of this suspension deposited on a carbon film copper grid. Hexane was chosen as the dispersant to avoid dissolution of HPA particles in the samples.

Nitrogen porosimetry was undertaken on a Quantachrome Nova 2000e porosimeter, and analysed using NovaWin software version 11. Samples were degassed under vacuum at 120°C for three hours, and analysed by nitrogen adsorption at -196°C, with equilibration times of 150 seconds for each data point. Adsorption and desorption isotherms were recorded for all parent silicas and supported catalysts. Brunauer-Emmett-Teller (BET) surface areas were calculated from the adsorption data over the relative pressure range 0.01 – 0.2, and micropore areas and volumes estimated using the t-plot statistical thickness method, with the deBoer standard curve, over a typical relative pressure range of 0.2 – 0.5. Pore-size distributions and volumes were estimated by applying the Barrett-Joyner-Halenda (BJH) method to desorption isotherms over the full range of relative pressures.

Raman spectra were recorded with a Renishaw inVia microscope using a Renishaw HPNIR laser source (λ = 785 nm) at 100% intensity. Each spectrum was recorded as the sum of 100 accumulations, at a rate of one second per accumulation. Experiments were conducted, and data analysed, using the Renishaw software WiRE.

Diffuse-reflectance Fourier-transform infrared spectroscopy (DRIFTS) was performed using a Thermo-Nicolet Avatar FTIR with Smart Collector. Before analysis, 20 mg of the dried catalyst sample was ground with 1 g potassium bromide and dried at 80^{o}C for 24 hours. Titration experiments were performed by adding pyridine dropwise until the powder no longer flowed freely, and drying the treated sample under vacuum at 120^{o}C to remove excess adsorbent. Spectra were produced from 50 acquisitions and analysed in Microsoft Excel.

Thermogravimetric analysis (TGA) and differential scanning calorimetry (DSC) data were obtained simultaneously using a Stanton Redcroft STA-780 series instrument. Experiments were conducted on 10 – 15 mg dried samples in an alumina crucible, using powdered alumina as a counterweight. All data were collected at a rate of one point per second, with a total gas flow rate of 20 ml min^{-1} and an equilibration time of at least 20 minutes before the start of analysis. Three different experiments

were performed. Firstly, the water content of pure undried HPW (98%, Sigma Aldrich) was analysed in helium by heating to 700^{o}C, at a constant ramp rate of 10^{o}C min^{-1}. Secondly, loss of surfactant (Pluronic P-123) from SBA-15 was analysed in synthetic air (20% oxygen in helium) by heating to 800^{o}C at a constant ramp rate of 10^{o}C min^{-1}. Finally, the surface silanol densities of SBA-15 and KIT-6 were measured by heating the samples in helium to 1000^{o}C at 15^{o}C min^{-1} and maintaining this temperature until no further mass loss could be discerned (typically three hours). Prior to measurement, the silica supports were heated to 120^{o}C at a ramp rate of 15^{o}C min^{-1} and maintained at this temperature for three hours, to ensure complete removal of adsorbed water.

Inverse gas chromatography (IGC) measurements were performed on SBA-15, KIT-6 and fumed silica using a Surface Measurements Systems (SMS) IGC instrument. Columns were prepared by packing a sample (typically 20 – 30 mg) into a silanised column (diameter 2 mm) between plugs of silanised glass wool. Experiments were conducted at varying temperatures (40 – 120^{o}C) using n-alkanes (C_6 – C_{10}), methanol and ethyl acetate as adsorbents, with partial pressures of 0.02-0.04 in helium. Calibration experiments were performed with methane at a partial pressure of 0.10. The flow rate was fixed at 10 sccm, the relative humidity at 0% and the solvent oven temperature at 40^{o}C. All samples were dried before analysis at 120^{o}C under a 10 sccm flow of helium, with water loss monitored via the TPD output. Data were collected via the FID and analysed in Microsoft Excel.

Preliminary leaching experiments were performed in sealed glass tube reactors in a Radleys Carousel 12 Plus Reaction Station. A sample of 50 mg catalyst was added to 10 ml methanol, and the mixture stirred at 700 rpm and 60^{o}C for four hours. The solid was recovered under suction and analysed by EDX, while leached HPA in the filtrate was detected by ultraviolet-visible (UV-vis) spectroscopy. Filtrate samples were placed in Lightpath Optical Ltd. quartz cuvettes (path length 10 mm) and analysed using a Jasco V-570 UV-vis/NIR spectrometer via the software Spectra Manager.

2.2 Catalyst preparation

Synthesis of SBA-15 silica

Pluronic P-123 (20.0 g) was dissolved in 1.6 M hydrochloric acid (750 cm^3) in a closed polypropylene bottle with stirring (350 rpm) at 35^{o}C for two hours. Tetraethyl orthosilicate (44.6 cm^3) was added and the mixture stirred at 35^{c}C for 24 hours. Stirring was stopped and the mixture heated to 90^{o}C in the closed bottle for a further 24 hours. The resulting suspension was filtered and the solid product washed with distilled water (2 x 500 cm^3) and dried under suction. The product was calcined at 550^{o}C for six hours, with a ramp rate of 1^{o}C min^{-1}. SBA-15 was obtained as a white powder (11.6 g) which was ground before further use.

Synthesis of KIT-6 silica

Pluronic P-123 (20.0 g) and n-butanol (24.6 cm^3) were dissolved in 0.56 M hydrochloric acid (780 cm^3) in a closed polypropylene bottle with stirring (350 rpm) at 35°C for two hours. Tetraethyl orthosilicate (44.6 cm^3) was added and the mixture stirred at 35°C for 24 hours. Stirring was stopped and the mixture heated to 80°C in the closed bottle for a further 24 hours. The resulting suspension was filtered and the solid product washed with distilled water (2 x 500 cm^3) and dried under suction. The product was calcined at 550°C for six hours, with a ramp rate of 1°C min^{-1}. KIT-6 was obtained as a white powder (12.5 g) which was ground before further use.

Synthesis of supported $H_3PW_{12}O_{40}$ catalysts

Solutions of 12-phosphotungstic acid hydrate (HPW) in methanol (15 cm^3) of appropriate concentrations were added to finely ground samples of SBA-15, KIT-6 or fumed silica (0.5 g) with stirring (700 rpm) at ambient temperature (~22°C). Concentrations of HPW were calculated assuming zero water content in the pure material. The suspensions were stirred at 300 rpm in sealed flasks for 18 hours, then dried by rotary evaporation at 40°C. The resulting solids were left at 60°C in static air for 24 hours, finely ground and stored under vacuum.

A series of 10 catalysts was produced on SBA-15, while 12 catalysts were prepared on the other supports. Nominal loadings were in the range 15 – 80 wt.%.

Synthesis of supported $Cs_xH_{3-x}PW_{12}O_{40}$ catalysts

Solutions of caesium chloride in methanol (20 cm^3) of appropriate concentrations were added to finely ground samples of SBA-15 (1 g) with stirring (300 rpm) at ambient temperature (~22°C). The suspensions were stirred in sealed flasks for 18 hours, then dried by rotary evaporation at 40°C. The resulting solids were left at 60°C in static air for 24 hours, finely ground and stored under vacuum.

Caesium salts were produced on the support *in situ*. Solutions of HPW in methanol (10 cm^3) of the appropriate concentration were added to the finely ground caesium-doped SBA-15 supports (0.5 g) with stirring (300 rpm) at ambient temperature (~22°C). Concentrations of HPW were selected to give Cs/HPW molar ratios of 2, taking into account the ~15 wt.% water content of the compound (as determined by thermogravimetric analysis, TGA). The suspensions were stirred in sealed flasks for 18 hours, then dried by rotary evaporation at 40°C. The resulting solids were left at 60°C in static air for 24 hours, finely ground and stored under vacuum. A series of five catalysts was produced for preliminary studies, with nominal HPW loadings in the range 10 – 50 wt.%.

2.3 Alpha-pinene isomerisation tests

Alpha-pinene isomerisation reactions were performed in sealed glass tube reactors in a Radleys Carousel 12 Plus Reaction Station. Tetradecane (0.166 g) was dissolved in neat alpha-pinene (1.702 g) and the solution stirred at 35^{o}C. A sample (~50 µl) was removed by pipette and diluted with dichloromethane (~2 cm^{3}) for analysis by gas chromatography. Catalyst (50 mg) was added to the solution stirred at 700 rpm and the reaction monitored for four hours, with the temperature maintained at 35 ± 1^{o}C. Samples were filtered and diluted as above at ten minute intervals for the first hour, and also after 90, 120, 150, 180 and 240 minutes.

Gas chromatography (GC) measurements were performed using a Varian CP-3800 gas chromatograph fitted with a CP-8400 autosampler and a 30 m x 0.53 µm DB1 capillary column. Data were analysed using the Varian software Star. Each reaction aliquot was analysed three times; the ratio of the alpha pinene and tetradecane (internal standard) peak intensities was calculated for each measurement, and a mean value obtained after discarding outliers. The mean retention factor for each aliquot was converted to a concentration of alpha-pinene by means of a calibration curve. Product concentrations were calculated in a similar manner. In practice, it was found that the initial measured alpha-pinene concentrations (before addition of catalyst) differed from the expected values, which could be estimated from the calibration curve using the known reagent starting concentrations. The reactant and product concentrations were thus scaled to correct for this error, under the assumption that all concentrations were systematically affected.

To ensure accuracy, calibration curves were constructed within two weeks of conducting a reaction. The calibration experiments were performed by preparing five mixtures of tetradecane and alpha-pinene with known concentrations, and obtaining GC measurements as above. Calibration curves were also obtained for the major products of the reaction: camphene, limonene, alpha-terpinene, para-cymene, gamma-terpinene and terpinolene. The range of concentrations for each compound was chosen to reflect the likely range of concentrations observed during a reaction.

Reaction profiles were constructed for each catalyst by plotting the measured alpha-pinene concentrations against their corresponding sampling times. In each case, the initial reaction rate was calculated as the gradient of the straight-line region of the profile, which typically occurred between 10 and 60 minutes. The rates of production of camphene and limonene were similarly calculated from the concentration-time plots for these products. Selectivities were estimated by dividing the rate of production of each product by the total rate of reaction.

3. Results and discussion

3.1 Powder X-ray diffraction (PRXD) studies of supports

Powder X-ray diffraction (PXRD) is a powerful and versatile technique which allows crystalline components of solid mixtures to be identified.[96] The sample is typically packed into a non-diffracting holder to produce a flat bed, which is illuminated by X-rays of a select wavelength. X-rays are generated in an X-ray tube, wherein a heated cathode filament releases electrons that collide with a metal target under vacuum. If a collision is inelastic, energy from the incoming electron may be transferred to an electron in a K (1s) or L (2p) orbital of the metal, causing it to be ejected from the atom. This ionisation event generates an electron hole, which is rapidly filled by an electron from a shell at higher energy. Relaxation of the outer electron causes an X-ray to be produced, with energy equal to the gap between the orbitals involved: for example, PXRD experiments typically employ X-rays from a copper source, with an energy (8.06 keV) corresponding to the difference between the K (1s) and L (2p) subshells.

A diffraction pattern is produced by changing the relative positions of the source, specimen and detector. In the Bragg-Brentano geometry, the detector is rotated around the specimen over a range of angles 2θ, while the specimen and source remain fixed. However, more complex geometries are often utilised, particularly if it is necessary to improve the intensity or quality of the X-ray beam. For example, a monochromator crystal is sometimes placed in the path of the beam to selectively focus a single wavelength from the X-ray emission spectrum into an intense beam on the detector. In one common setup, the monochromator is positioned between the specimen and the detector and moves with the detector as it rotates around the specimen.

In this study, PXRD patterns were recorded using a simple Bragg-Brentano geometry without a monochromator. To remove unwanted X-rays, such as the Kβ emissions resulting from relaxation of M (3p) electrons to the K shell, a nickel filter was placed in the path of the incident beam. Alignment of the X-rays was achieved by use of Soller slits, and a mask was employed to restrict the beam to the surface of the powder sample. Finally, divergence and anti-scatter slits were utilised to restrict the width of the X-ray beam and minimise the error in the measured reflection angles. The specimen position was fixed, and the source and detector were each rotated by an angle θ to produce the measured angular displacement 2θ (Fig. 15).

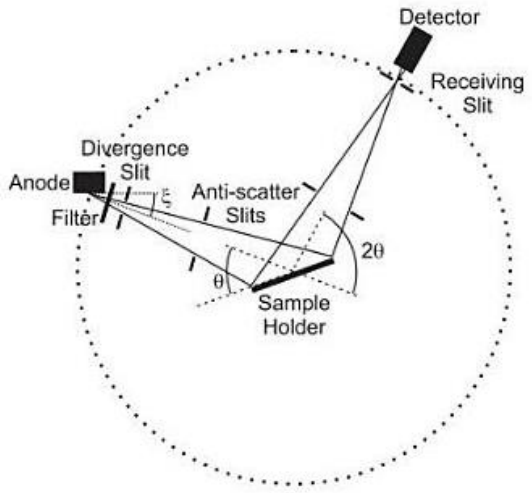

Fig. 15 Schematic representation of the diffractometer geometry employed in this study. The angle 2θ is varied by rotating the X-ray source (anode) and detector towards each other around the fixed specimen. Note that the anode is not parallel to the incident beam axis but tilted by a small angle ξ, typically 6^{o}. Image reproduced from ref. 96.

A diffraction line is produced if X-rays reflected from consecutive, equivalent planes of atoms constructively interfere. For this to occur, the path lengths of the reflected rays must differ by an integer multiple of the X-ray wavelength λ (1.5418 Å for Cu Kα radiation). This fact leads to Bragg's Law,

$$\sin\theta = \frac{\lambda}{2d_{hkl}} \qquad \text{(Eq. 3)}$$

where d_{hkl} is the spacing of lattice planes with Miller indices (*hkl*). The angle of reflection is equal to the angle of incidence, so a diffracted beam is only detectable if the angle from the source to the lattice plane is equal to the angle from the specimen to the detector. However, since a powder contains a large number of crystallites in different orientations, a small fraction of crystallites will always be in the correct orientation to produce a detectable diffracted beam. PXRD thus produces a pattern of diffraction lines corresponding to the different lattice spacings, d_{hkl}, present in the specimen. This pattern may be used to determine the crystal system and lattice type of the material, and the cell parameters can hence be calculated by identifying the lattice planes responsible for each diffraction line.

In this study, PXRD is used to investigate two types of system: crystalline HPAs or HPA salts, which produce reflections at high angles ($2\theta > 10^{o}$); and mesoporous silicas SBA-15 and KIT-6, which produce reflections at low angles ($2\theta < 10^{o}$) due to the ordered arrangement of pore channels. Generally, HPAs exhibit a body-centred cubic structure.[4,5] SBA-15 and KIT-6 exhibit hexagonal[35] and

cubic[36] structures respectively. However, typically only the (100), (110) and (200) reflections in SBA-15 are easily resolved, so the data may be processed in a similar manner to data for the other, cubic, systems. If the lattice parameter is denoted $|\vec{a}|$, then $d_{hkl} = \sqrt{N}\,|\vec{a}|$, where $N = (h^2 + k^2 + l^2)$ for cubic systems and $N = (h^2 + hk + k^2)$ for the (hk0) lines of a hexagonal lattice. Thus:

$$\sin\theta = \frac{\lambda}{2|\vec{a}|}\sqrt{N} \qquad \text{(Eq. 4)}$$

Observed values of θ exhibit an error due to effects such as misalignment of the diffractometer parts, displacement of the flat sample from the diffractrometer axis and vertical divergence of the incident beam.[97-99] This error, $\Delta\theta$, varies with θ in a complicated manner. Various approximations, assuming empirically-determined trigonometric dependencies on θ, have been proposed[100, 101] and may be used to improve initial estimates of $|\vec{a}|$ if many diffraction lines are measured. However, in the case of mesoporous silicas, typically only one to three peaks are well-resolved. For such restricted data, $\Delta\theta$ is best approximated as a constant error in θ, calculated as an average of the shifts required to bring the line positions into agreement with their predicted relationships (i.e. $\sin^2\theta \propto N$).[102] For SBA-15, the planes (100), (110) and (200) give rise to reflections at θ_{100}, θ_{110} and θ_{200}, with predicted N values of 1, 3 and 4 respectively. Thus:

$$\frac{\sin(\theta_{110} + \Delta\theta)}{\sin(\theta_{100} + \Delta\theta)} = \sqrt{3} \qquad \frac{\sin(\theta_{200} + \Delta\theta)}{\sin(\theta_{100} + \Delta\theta)} = 2 \qquad \text{(Eq. 5)}$$

and a mean value for $\Delta\theta$ may be estimated:

$$\Delta\theta = \frac{1}{2}\left[\tan^{-1}\frac{\sqrt{3}\sin\theta_{100} - \sin\theta_{110}}{\cos\theta_{110} - \sqrt{3}\cos\theta_{100}} + \tan^{-1}\frac{2\sin\theta_{100} - \sin\theta_{200}}{\cos\theta_{200} - 2\cos\theta_{100}}\right] \qquad \text{(Eq. 6)}$$

After applying this correction, Eq. 4 may be applied to any line to obtain an estimate for $|\vec{a}|$. In SBA-15, this value represents the smallest distance between parallel layers of pores. In a cross-sectional view of the pore lattice, the vector $\vec{a}$ intersects the vector, $\vec{L}$, between pore centres at an angle of 30^o (Fig. 16(a)). Thus, the distance $|\vec{L}|$ may be calculated:

$$\left|\vec{L}\right| = |\vec{a}|\sec 30^o = \frac{2}{\sqrt{3}}|\vec{a}| \qquad \text{(Eq. 7)}$$

$\left|\vec{L}\right|$ is the summation of two pore radii, R (i.e. a pore diameter) and the thickness of the wall between pores, T. Since an average value for R may be estimated by Barret-Joyner-Halenda (BJH) analysis of porosimetry data,[83] it is possible to tentatively estimate a value for the wall thickness, T, as $\left|\vec{L}\right| - 2R$.

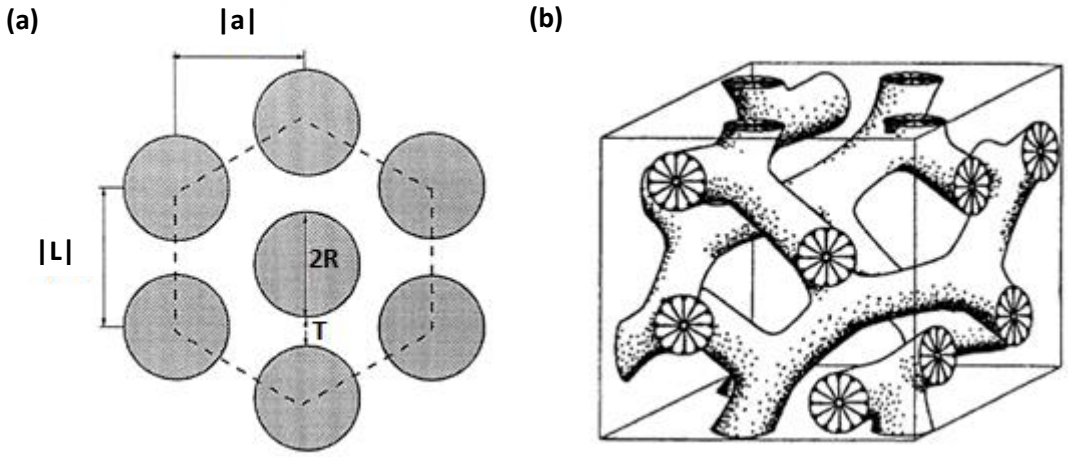

Fig. 16 (a) Diagram of the cross-section of SBA-15, indicating packing of cylindrical channels;[103] (b) Interwoven pore channels in KIT-6.[104]

The batch of SBA-15 used in this study exhibits the expected diffraction pattern, with three peaks at 2θ = 1.02°, 1.71° and 1.94° (Fig. 17). Applying Eq.6 produces a correction $\Delta\theta$ = 0.04 ± 0.01°, and Eq. 4 and Eq.7 yield $|\vec{a}|$ = 9.4 ± 0.1 nm and $|\vec{L}|$ = 10.8 ± 0.1 nm. Setting 2*R* = 5.903 nm (measured by porosimetry) gives an estimate for the wall thickness, *T*, of 4.9 ± 0.2 nm, which is within the range of values typically reported in the literature (3-6 nm).[105] It should be noted that while the peak positions should be measurable to ±0.01° (the step size of the diffraction pattern), the broadness of the peaks and evident noise likely limits the precision to one decimal place. Thus, the systematic error $\Delta\theta$ represents only a minor component of the total error in the estimates of $|\vec{a}|$, $|\vec{L}|$ and *T*.

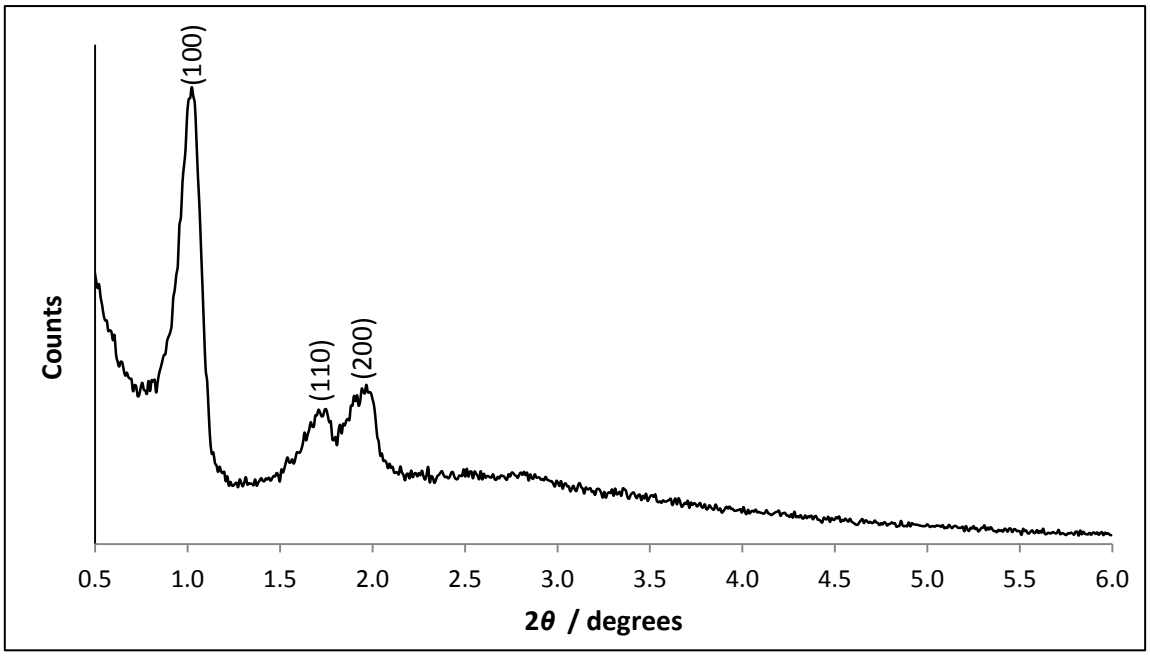

Fig. 17 Low-angle PXRD pattern for SBA-15 silica support. Bragg angles are corrected using Eq. 6.

The pattern for KIT-6 (Fig. 18), a body-centred structure (I-lattice), exhibits two discernible peaks at 1.09° and 1.24°, corresponding to the (211) and (220) diffracted beams respectively. Eq. 4 indicates that the ratio of sin θ values should be 2 / √3, and the error $\Delta\theta$ may thus be estimated by rearrangement as in Eq. 6. However, it is difficult in practice to exactly determine the position of the (220) diffraction line, so the necessary correction cannot be calculated to a satisfactory degree of accuracy. Instead, $\Delta\theta$ may be assumed to be equal to the value computed for the SBA-15 sample. This assumption leads to an estimated lattice parameter $|\vec{a}| = 21.4 \pm 0.2$ nm, which is in agreement with literature values.[35,101,103]

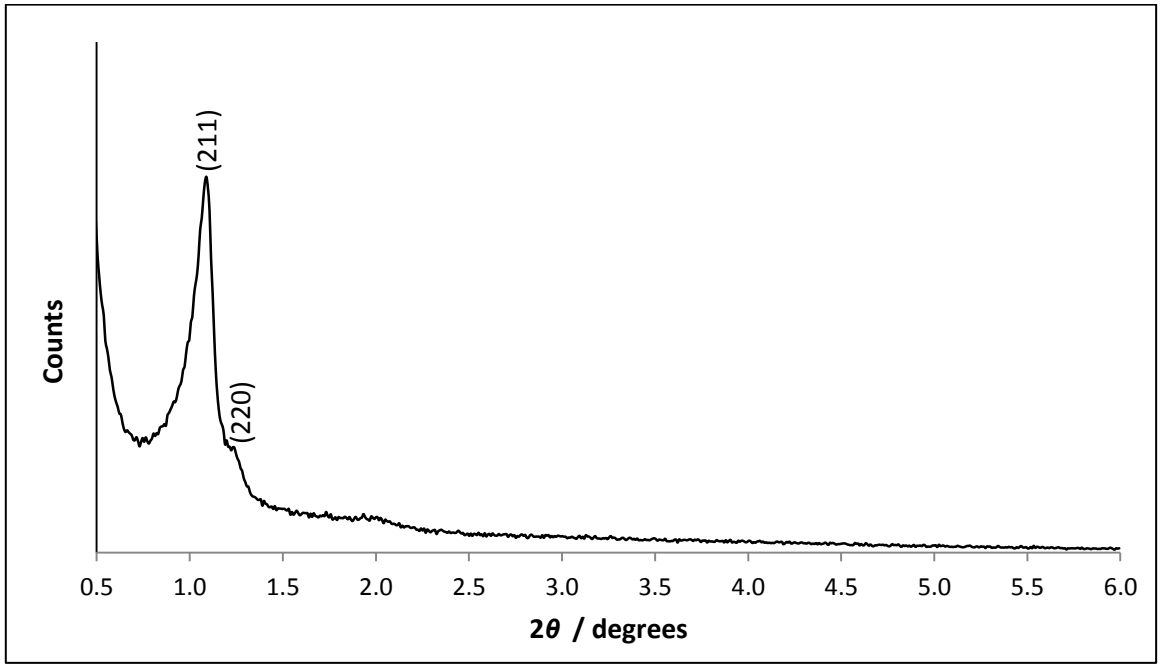

Fig. 18 Low-angle PXRD pattern for KIT-6 silica support. Bragg angles are adjusted using the correction calculated for the SBA-15 support.

In KIT-6, the distance between pores is not as simply visualised as in SBA-15, as the pore system consists of two interwoven networks of channels. However, careful analysis (Fig. 16(b)) indicates that $T = |\vec{a}|/2 - 2R$.[102] Setting $2R$ = 5.340 nm (from porosimetry data) results in a wall thickness, T, of 5.3 ± 0.2 nm, which is close to the estimate for SBA-15.[103] The similarity in the dimensions of the two pore systems is also evident in transmission electron microscopy (TEM) images of the supports (Fig. 19).

TEM images of the supports show well-ordered pore structures with no visible blockages. Porosimetry data (section 3.4) are typical of non-occluded channels, and thermogravimetric analysis shows that near-complete removal of surfactant can be achieved even by a mild thermal treatment, consisting of a linear temperature ramp to 400°C over one hour (in practice, supports were

maintained at 550°C for six hours). Nonetheless, X-ray photoelectron spectroscopy (XPS) analyses of the final supported HPW catalysts (sections 3.3 and 3.5) reveal low concentrations of carbon, which may partly correspond to residual surfactant or coke retained following calcination of the supports.

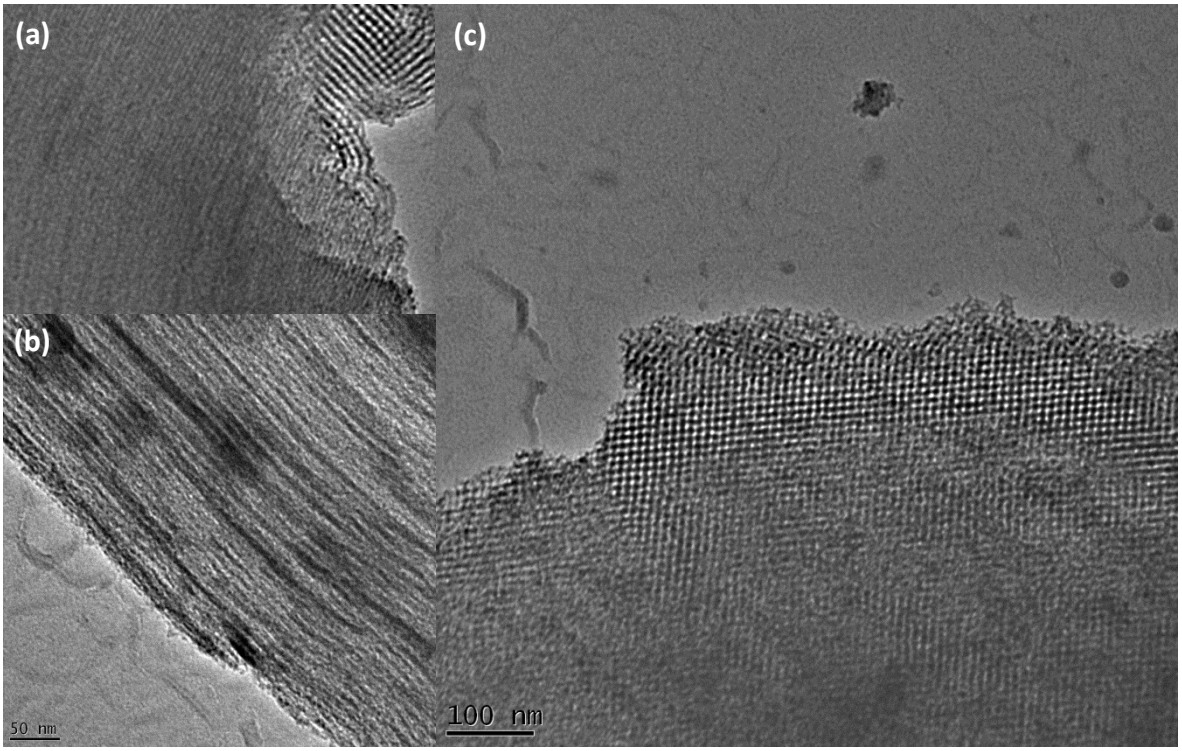

Fig. 19 TEM images of the silica supports in this study, at approximately equal scales: (a) pore network in SBA-15; (b) linear channels in SBA-15; (c) pore network in KIT-6.

3.2 Preparation of supported catalysts

In this study, impregnation solutions were prepared without an initial drying step to remove water from the heteropoly acid. Thus, HPW used for impregnations exhibits a formula $H_3PW_{12}O_{40}.nH_2O$. According to the literature,[4,5] n = 29 or 30 for HPW crystallised directly from water, but this value decreases to 6 if the crystal is dried using a desiccating agent or vacuum. Notably, hydrates with n < 6 are found to be unstable.[4] As discussed in section 1.1, infrared, NMR and neutron scattering studies[20-24] suggest that water molecules form $[H_5O_2]^+$ dimers between Keggin units, and are therefore directly involved in the mechanism of proton transfer during heterogeneous catalysis.

To accurately determine the value of n for the HPW in this study, the pure undried material was analysed by thermogravimetric analysis (TGA). A 10 mg sample was heated from 10 to ~700°C at a ramp rate of 10°C min^{-1}, and the change in mass measured. The thermogram (Fig. 20) indicates drying occurs in two rapid losses below 200°C followed by a more gradual loss up to 700°C. In the

first stage, ~9% mass is lost, corresponding to 16 water molecules; in the second stage, ~4% is lost corresponding to eight water molecules; and in the third stage, at least a further 3% is lost, corresponding to a minimum of six molecules. This pattern is consistent with rapid liberation of water from $H_3PW_{12}O_{40}.30H_2O$ to give the stable $H_3PW_{12}O_{40}.6H_2O$ (via $H_3PW_{12}O_{40}.14H_2O$) followed by gradual decomposition to unstable, less hydrated forms. The calculated mass of water in HPW was accounted for when preparing caesium salts of HPW on SBA-15, allowing particular *Cs/HPW* molar ratios to be targeted.

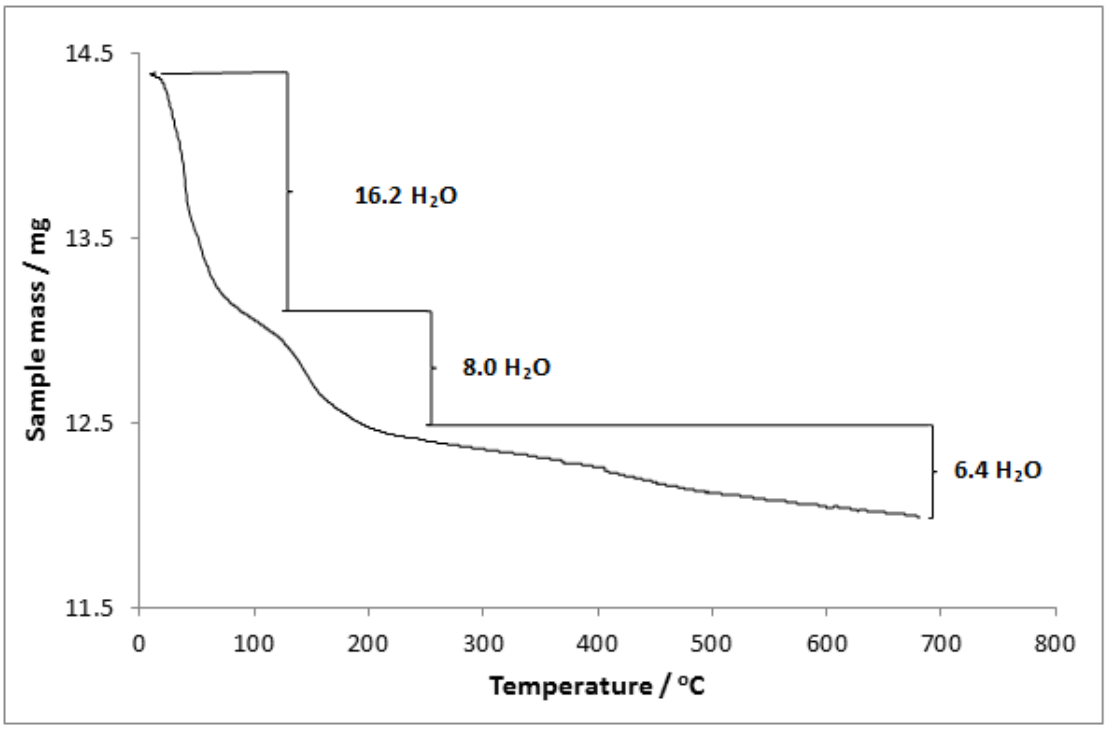

Fig. 20 TGA thermogram for the HPW hydrate utilised in this study. Mass losses are consistent with the formula $H_3PW_{12}O_{40}.30H_2O$.

Impregnations were conducted in methanol to avoid decomposition problems that have been reported in aqueous solutions.[11] To ensure that Keggin units did not undergo structural changes during impregnation, Raman spectra were obtained for the dry catalysts and compared with spectra for the pure HPW. For all catalysts, including the supported caesium salts, all major Raman absorption bands can be attributed to the presence of Keggin units; in particular, no bands due to tungsten(VI) oxide (the final product in the decomposition of HPW[11]) were observed (Fig. 21). That incorporation of caesium into the HPW lattice does not lead to substantial changes in Raman signals suggests either that the interaction of cations with Keggin anions is relatively weak (i.e. does not perturb W-O vibrations), or that substituting $[H_5O_2]^+$ species for caesium ions does not significantly alter the structure of the material.

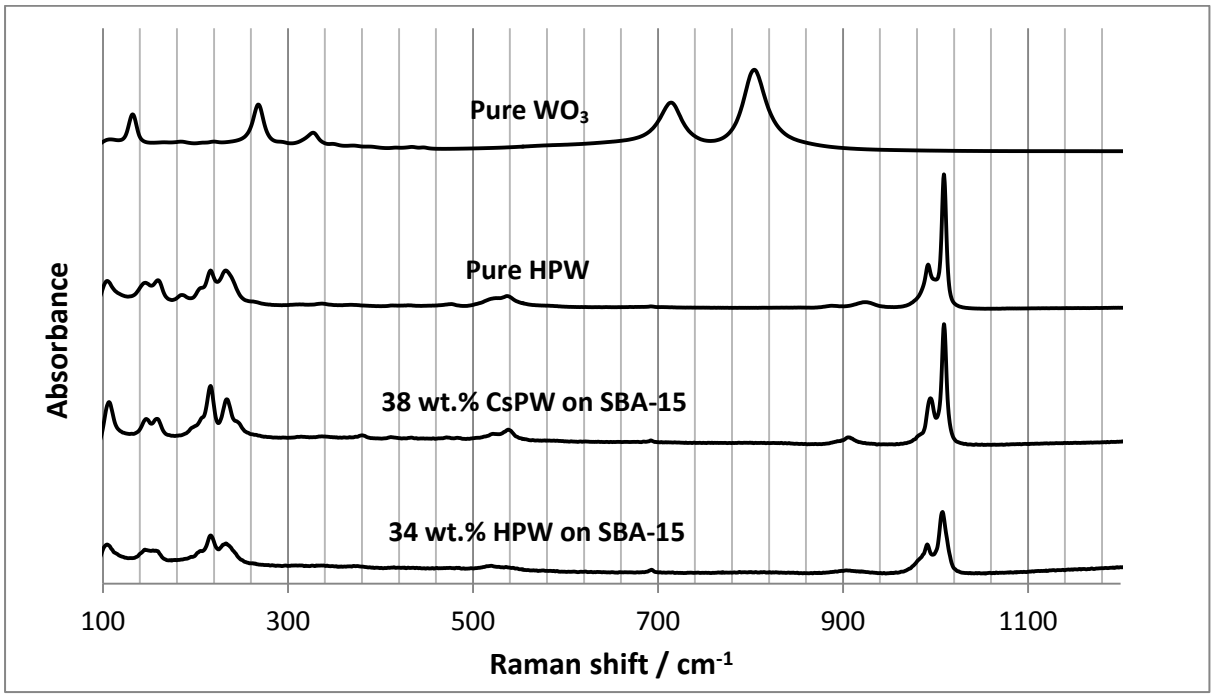

Fig. 21 Typical Raman spectra for supported HPW and caesium-HPW salts, compared with spectra for pure HPW and tungsten(VI) oxide, WO_3. Catalyst loading values are based on EDX measurements.

PXRD patterns also provide structural data. HPW exhibits a number of structures due to the variable number of water molecules in the unit cell, and the ability of the pseudo-spherical Keggin units to pack in a number of stable arrangements.[4,5] Most commonly a body-centred structure is observed, resulting in PXRD patterns where all lines satisfy the condition ($h^2 + k^2 + l^2$) = even. Notably, however, the central Keggin unit in the hexahydrate is rotated 90° relative to the units at the cell vertices (Fig. 22). As such, the cell does not exhibit perfect body-centred cubic symmetry, and low-intensity lines where ($h^2 + k^2 + l^2$) = odd may be observed.

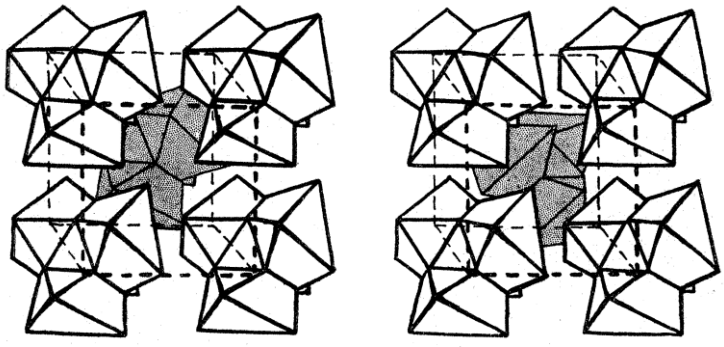

Fig. 22 Possible arrangements of Keggin units in the unit cell, from ref. 4. The central unit (grey) and four of the eight vertex units are shown. Left: a true body-centred arrangement; right: a distorted body-centred arrangement in which the central unit is rotated 90° relative to vertex units.

Like the hexahydrate of bulk HPW,[4] silica-supported HPW catalysts exhibit a diffraction pattern in which most intense lines satisfy the symmetry condition for a body-centred cubic cell (Fig. 23(a)). The supported caesium salts exhibit a similar pattern (Fig. 23(b)), but with lines shifted to significantly higher values of 2θ. This suggests that inclusion of caesium in the HPW lattice reduces the size of the unit cell, providing tentative evidence that substitution of $[H_5O_2]^+$ ions for caesium is thermodynamically favoured. Notably, no lines due to caesium chloride (the source of caesium used in this study) were observed in the final supported catalysts, confirming that all added caesium is present in the HPW salt (Fig. 23(c)).

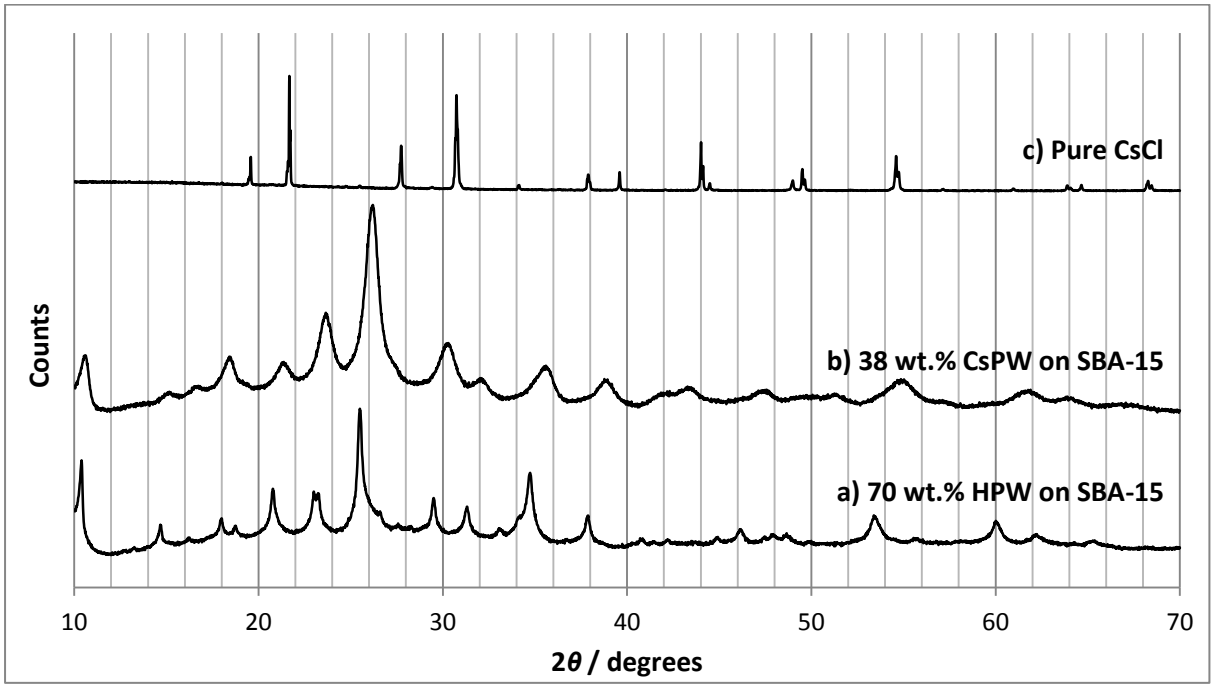

Fig. 23 Powder X-ray diffraction patterns for (a) 70 wt.% HPW on SBA-15; (b) 38 wt.% CsPW on SBA-15; and (c) pure CsCl. Loading values are based on EDX measurements.

Detailed indexing may be performed on patterns for samples with the highest loadings, as these exhibit the sharpest and most intense peaks (Fig. 24). As for the mesoporous supports, lattice parameters may be estimated by approximating the error in θ. A popular approach, the Cohen method, assumes a dependency $\Delta\theta \propto \cos^2\theta$ and delivers an estimate for $|\vec{a}|$ which minimises the deviation from this trend. [98, 100, 101] However, in this study such an approximation was found to be unreliable, as the results varied greatly if small changes were made to the subset of diffraction lines analysed.

A more satisfactory estimate of $|\vec{a}|$ was obtained by plotting the values $N = (h^2 + k^2 + l^2)$ for well-defined diffraction lines against the corresponding values of $\sin^2\theta$. According to Eq. 4, the gradient of such a plot should be equal to $(\lambda^2 / 4|\vec{a}|^2)$ while the intercept provides an estimate for the

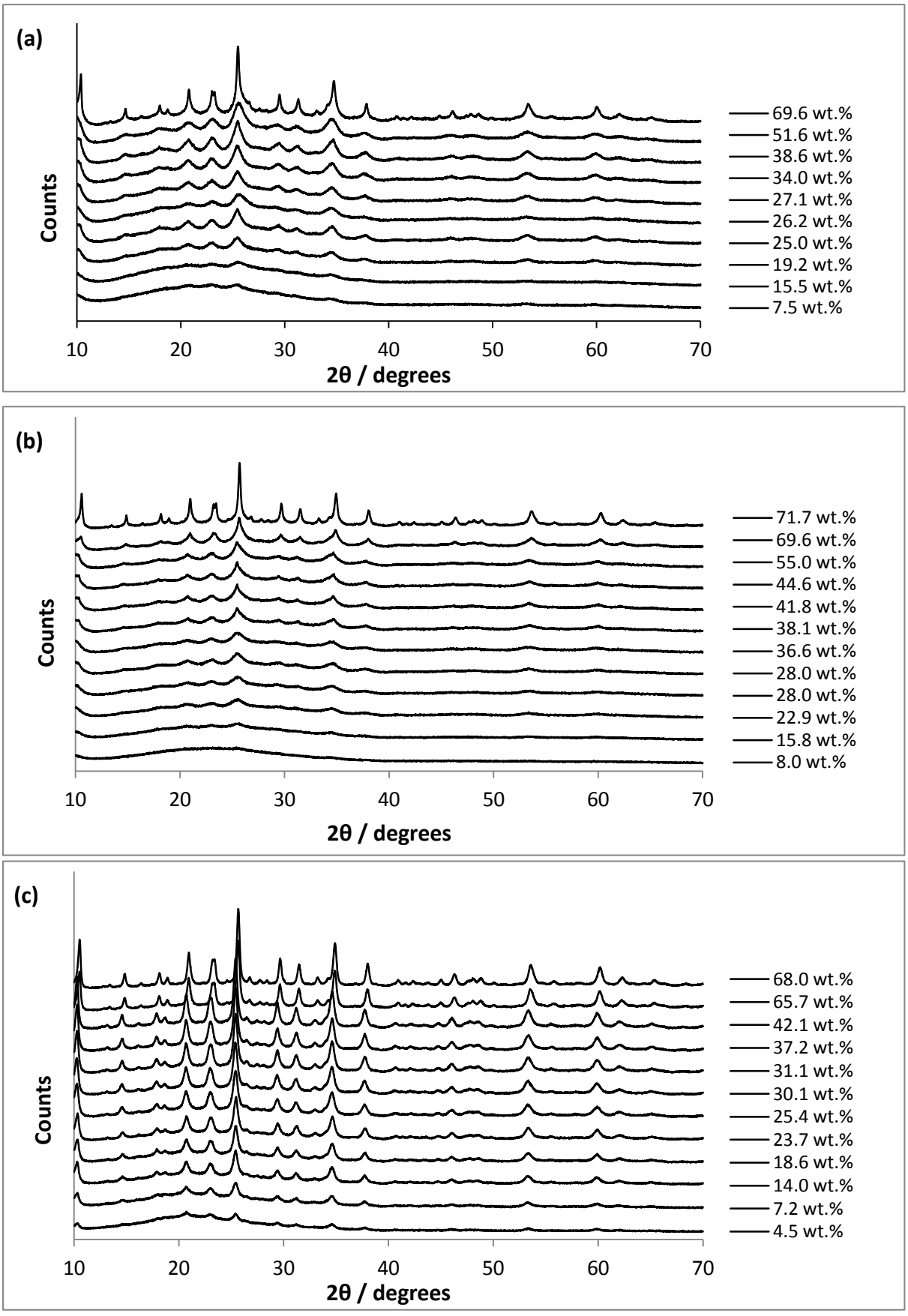

Fig. 24 PXRD patterns of HPW on (a) SBA-15, (b) KIT-6 and (c) fumed silica at a range of loadings.

average error in $\sin^2 \theta$. Except for the KIT-6 sample with a HPW loading of 8.0 wt.% (measured by EDX), all samples exhibit a number of diffraction lines indicating the presence of crystalline HPW. Lattice parameters were estimated from the five lines with highest intensity, which were assigned to reflections with N = 8, 10, 12, 22 and 50.

As loading increases, the supported HPW catalysts show slight decreases in $|\vec{a}|$, though these are comparable to the error in measurement (typically ± 0.01 Å; Fig. 25). Greatest variability is exhibited by catalysts supported on SBA-15, and the least by catalysts supported on fumed silica. In all cases, $|\vec{a}|$ is close to the reported value for HPW in its hexahydrate form (12.15 Å).[5] The observed variations may suggest that the density of HPW decreases close to the silica surface: at low loadings, a greater proportion of HPW is expected to interact directly with the support.

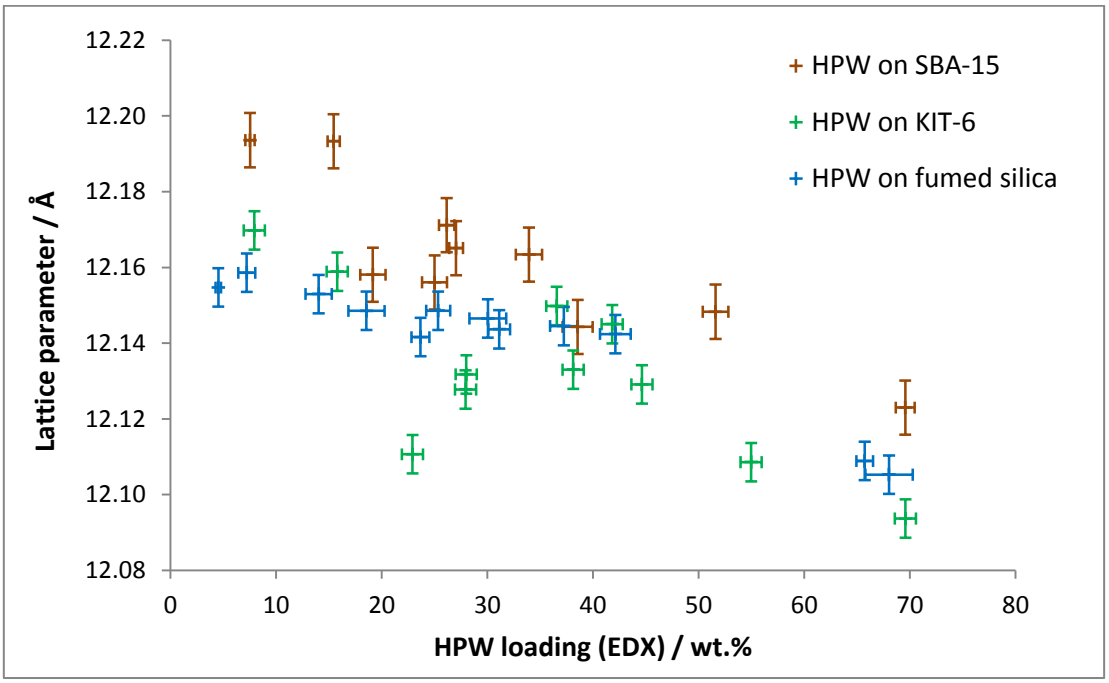

Fig. 25 Variation of lattice parameters with HPW loading in silica-supported catalysts. Loading values are estimated from EDX data (section 3.3). Errors in lattice parameters are roughly ±0.01 Å.

For the supported caesium salts of HPW, estimated values of $|\vec{a}|$ are substantially lower than the value reported for pure HPW (Fig. 26). This suggests that while the salt retains the structure of HPW, inclusion of caesium increases the density of Keggin units by 8 ± 1%. The overall increase in density, taking into account the change in molecular formula as caesium is added, is 19 ± 1%. The fact that all lines may be indexed to a single lattice also suggests that caesium is distributed uniformly between crystallites, though line broadening (e.g. due to the presence of large crystallites; see section 3.4) might prevent clusters of lines with similar positions and equal N values from being resolved.

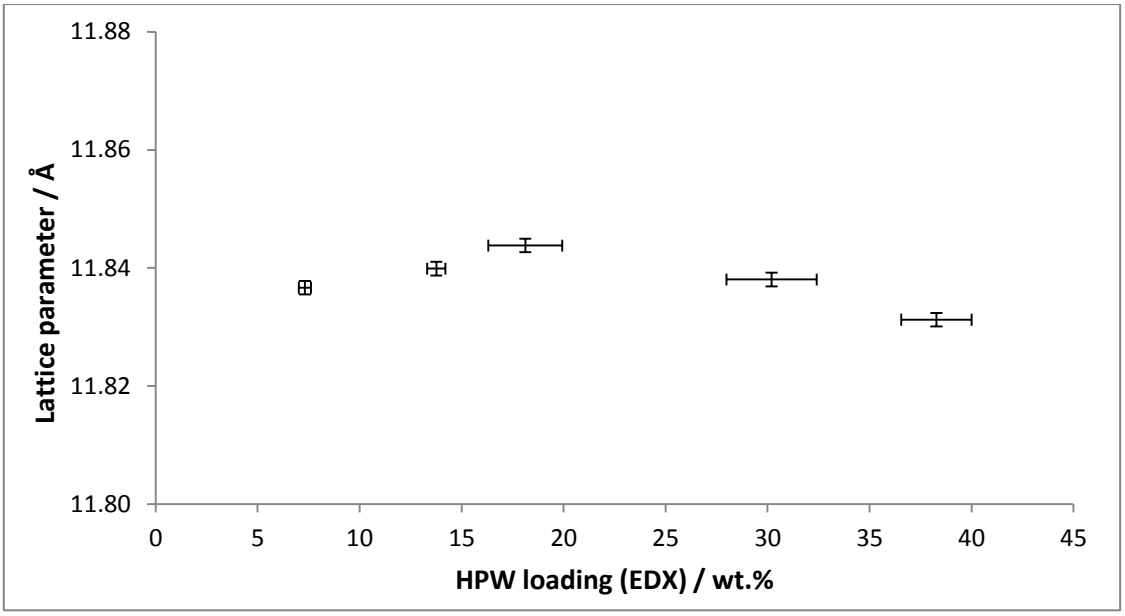

Fig. 26 Variation of lattice parameters with CsPW loading in SBA-15-supported catalysts. Loading values are estimated from EDX data (section 3.3). Errors in lattice parameters are approx. ±0.01 Å.

3.3 Quantification of catalyst loadings

The main method for determining catalyst loadings in this study was energy-dispersive X-ray spectroscopy (EDX).[106] In this technique, the composition of a sample is deduced from the pattern of X-rays emitted upon bombardment with a focussed beam of electrons. To allow compositional information to be linked to spatial features, EDX experiments are usually conducted in conjunction with an electron imaging method such as scanning electron microscopy (SEM).

In SEM, samples are dried and deposited as a thin layer on a suitable mount. The sample chamber is placed under high vacuum (typically less than 10^{-5} Torr) and subjected to an intense beam of electrons from an electron gun, which usually comprises a heated filament of tungsten or lanthanum hexaboride and an anode charged to produce an accelerating voltage of 0.2-30 kV. The electron beam is focussed to a spot 1-30 nm in diameter by condenser lenses, and redirected by deflector coils to scan across the sample area in a raster fashion. Upon colliding with the sample, the electron beam induces the emission of electrons, which can be intercepted and converted to an interpretable electrical signal by a scintillator-photomultiplier detector. The most intense and highly resolved images are achieved by the detection of secondary electrons, which are the low-energy electrons produced by inelastic collisions. However, it is also possible to detect the more energetic electrons which are backscattered following elastic collisions. Since heavier atoms scatter electrons more strongly, the contrast in backscatter images can be used to assess the compositional variation across the sample surface.

A secondary electron is generated when a sample atom is ionised by the electron beam. As in an X-ray gun (section 3.1), the energy of the incoming electron is such that an electron is ejected from a low-energy orbital, typically in the K (1s) or L (2p) shell. This generates an electron hole in the core shell, which is rapidly filled by an electron from a shell at higher energy. As the outer electron relaxes, a fixed energy is released, corresponding to the difference in energy between the outer and inner shells. The separation of shells varies between elements, so the released energy can be measured to determine the identity of the emitting atom. For example, 1739 eV corresponds to the separation of the K and L shells in silicon, and may be referred to as the Si Kα energy.

Energy may be released from an ionised atom in two ways. Firstly, the energy may be transferred to another electron in an outer shell, resulting in a second ionisation event. The newly ejected electron, the Auger electron, exhibits a kinetic energy which can be exactly related to the energy of the transition that produced it, providing an accurate indication of the source composition. Surface analysis based on this effect is termed Auger electron spectroscopy (AES). Since Auger electrons are easily reabsorbed, AES can provide a highly surface-sensitive measure of composition with excellent spatial resolution. However, such experiments must be performed under ultra-high vacuum, and spectra can be complicated by additional peaks arising from scattering and multiple ionisation events.

Instead of ejecting an Auger electron, an excited ion may release its excess energy in the form of a photon. The energy differences between the innermost shells of an atom are large, so photons are produced with wavelengths in the X-ray range, namely 0.01 to 10 nm (0.1 to 100 keV). X-rays are far more penetrating than electrons and may thus be detected at high intensity in the relatively moderate vacuum of a standard electron microscope. Moreover, while AES probes a surface layer less than 1 nm in thickness, emitted X-rays can provide an indication of the bulk composition of the sample. Indeed, the thickness over which a material can be analysed is limited only by the penetration depth of the incoming electrons, which depends strongly the accelerating voltage. For example, the penetration depth for carbon film is roughly 6 μm at a voltage of 20 kV, but lowering the voltage to 5 kV restricts penetration to 2 μm.

In EDX, X-ray emission (also termed X-ray fluorescence) is usually detected by means of a Si-Li diode cooled with liquid nitrogen. Cooling is required to minimise the conductivity of the diode, thus maximising discrimination between X-rays of different energies. The energy of an X-ray pulse is determined from the voltage measured after amplification and processing of the signal. It should be noted that processing of the diode output is necessary for good resolution, but time-consuming: a fraction of the duration of an EDX experiment must be allocated as “processing time”, wherein

newly incoming pulses “pile up” and must be corrected for in the final spectrum. For maximum resolution, the processing time must be carefully monitored, and the beam current adjusted to reduce signal pile-up to an acceptable level.

The result of an EDX experiment is a plot correlating X-ray energy with the photon count rate. Elements in the sample are identified from the positions of the spectral peaks, while loadings are estimated from the relative peak intensities. Quantification can be highly accurate, but errors may arise where the peaks of the principal elements are significantly overlapping. This problem is compounded by the presence of impurity peaks, the intensities of which may be misassigned to other elements during loading calculations. Errors may also be introduced due to differential absorption and emission of X-rays, due to compositional variation in the sample. These errors, collectively known as ZAF effects, can be roughly accounted for during data processing; however, complete correction is usually impossible, particularly if the sample is heterogeneous.

In this study, at least six EDX measurements were obtained for each sample, to provide a quantitative measure of the heterogeneity of the material. Some samples were found to be compositionally heterogeneous at the micrometre scale, and all materials exhibited variable particle shapes and sizes when imaged by SEM. Nonetheless, average loading measurements for all the catalyst series increase linearly with the nominal loadings (Fig. 27). The lack of scatter in the data suggests that discrepancies between the observed and expected loadings are mostly due to systematic errors, such as inaccurate ZAF correction factors or fractional loss of HPW during catalyst preparation.

EDX can also be utilised to obtain estimates of caesium loading in supported CsPW catalysts, allowing the molar ratio *Cs/HPW* to be calculated. This value is important because substitution of $[H_5O_2]^+$ ions by caesium ions strongly affects the activity, solubility and crystalline properties of the catalyst.[15, 16, 19, 27, 50, 52] Fig. 28 shows the variation in the *Cs/HPW* molar ratio across the series of supported catalysts synthesised in this study, as estimated from EDX; and Fig. 29 shows how nominal loadings of HPW and CsPW correlate with the EDX estimates. Clearly, *Cs/HPW* values lie consistently close to the expected value of 2, and the relationship between nominal and observed loadings is almost linear for both HPW and CsPW.

Another estimate of loading was obtained by X-ray photoelectron spectroscopy (XPS).[107] In XPS, as in EDX, the composition of a sample is determined by excitation of electrons in low-energy orbitals of the surface atoms. However, excitation in XPS is achieved by use of an intense beam of electrons, typically from an aluminium or magnesium source. As in X-ray diffractometers (section 3.1), a

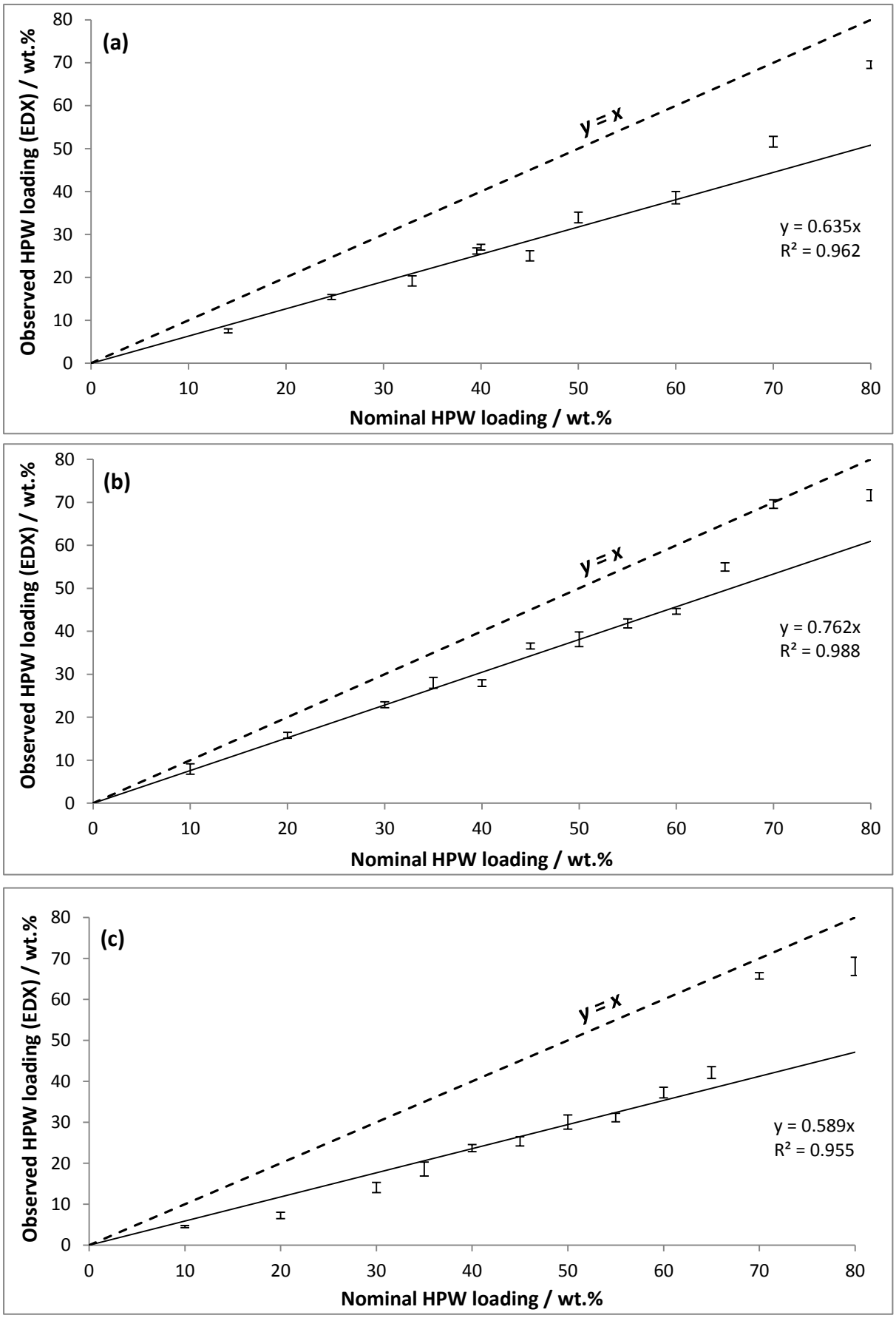

Fig. 27 Nominal and observed loadings of HPW on (a) SBA-15, (b) KIT-6 and (c) fumed silica.

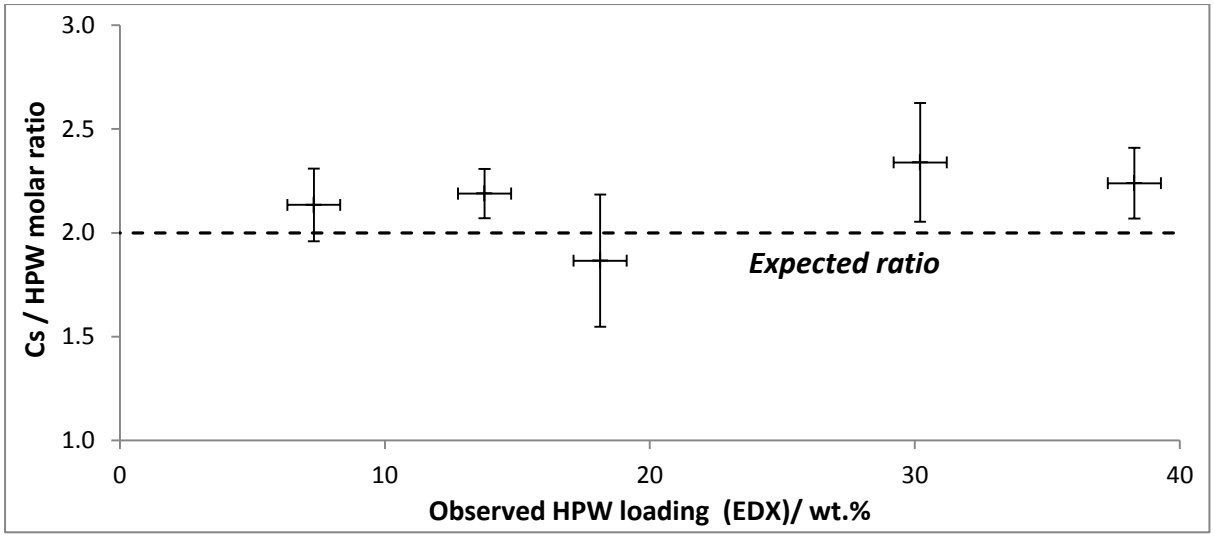

Fig. 28 Cs / HPW molar ratios of CsPW catalysts supported on SBA-15.

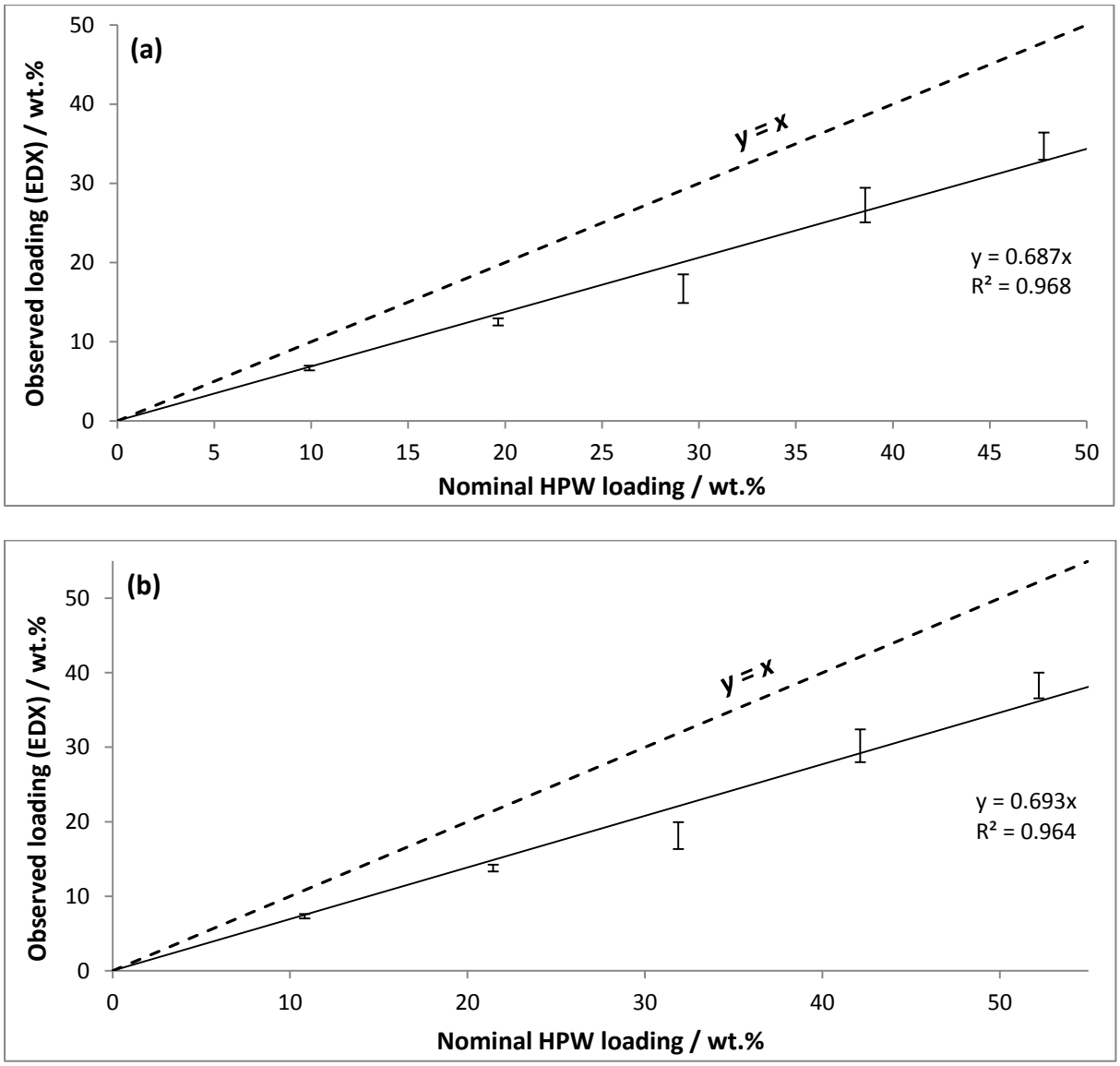

Fig. 29 Nominal and observed loadings of CsPW catalysts on SBA-15, based on (a) HPW and (b) CsPW.

monochromator may be introduced to fix the wavelength of the incident beam, and a charge neutraliser may be used to dissipate charge accumulated by non-conductive samples. An electron-energy analyser is employed to measure the kinetic energies of electrons ejected from the sample during X-ray bombardment. Since the incident photon energy is known, the binding energies of the collected photoelectrons can be easily calculated, allowing the identities and relative concentrations of the source atoms to be accurately determined.

An important difference between XPS and EDX is their sensitivity to surface composition. In EDX, the high-energy incident electrons can penetrate several micrometres into the sample, and X-rays can be detected even if they are emitted from atoms at the maximum penetration depth. In contrast, the photoelectrons in an XPS experiment are easily absorbed as they pass through the sample material, and are further dissipated as they travel the relatively large distance (typically one metre) from the sample to the detector. Indeed, an ultra-high vacuum ($< 10^{-9}$ Torr) is needed to deliver photoelectron signals with satisfactory intensity. The maximum path length of a photoelectron is dependent on the sample composition, but typically lies within the range 0.5 – 3.0 nm. Thus, while EDX provides an indication of the bulk composition of a sample, XPS can be used to characterise exclusively the layers of atoms nearest the surface.

To estimate the relative concentration of each element at the surface, a characteristic signal is integrated and scaled by a relative sensitivity factor (RSF), which varies according to the absorbing power, emission efficiency and volume of the atom irradiated. In practice, compositional information from XPS is often qualitative: since photoelectrons are very weakly penetrating, absorption effects vary significantly with the immediate environment of the emitting atom, which may be difficult to account for. Notably, in this study, loadings of the supported HPW catalysts estimated from the W 4f signals in XPS are ~60% lower than the values measured by EDX (Fig. 30). The discrepancy likely arises because the tungsten atoms in HPW are necessarily surrounded by other tungsten atoms, which are more strongly absorbing than the other atoms (silicon and oxygen) present in the catalysts. Signals from tungsten are thus more strongly attenuated than signals from other elements, causing loadings of this element to be underestimated.

If the difference between EDX and XPS results is attributable to preferential absorption of the W photoelectrons, the discrepancy might be expected to increase with particle size. However, this argument can only apply to catalysts where most of the external silica surface is exposed, allowing XPS signals due to the support to be considered constant. If HPW covers a large proportion of the surface, the signals due to Si and O will also be significantly attenuated by the overlying HPW. In

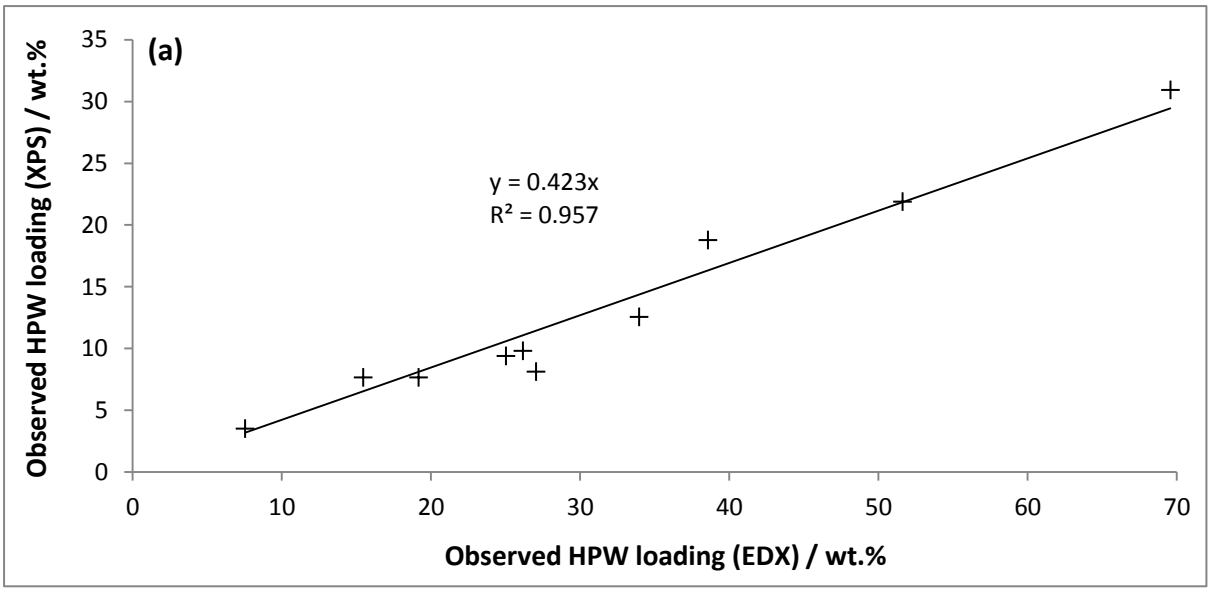

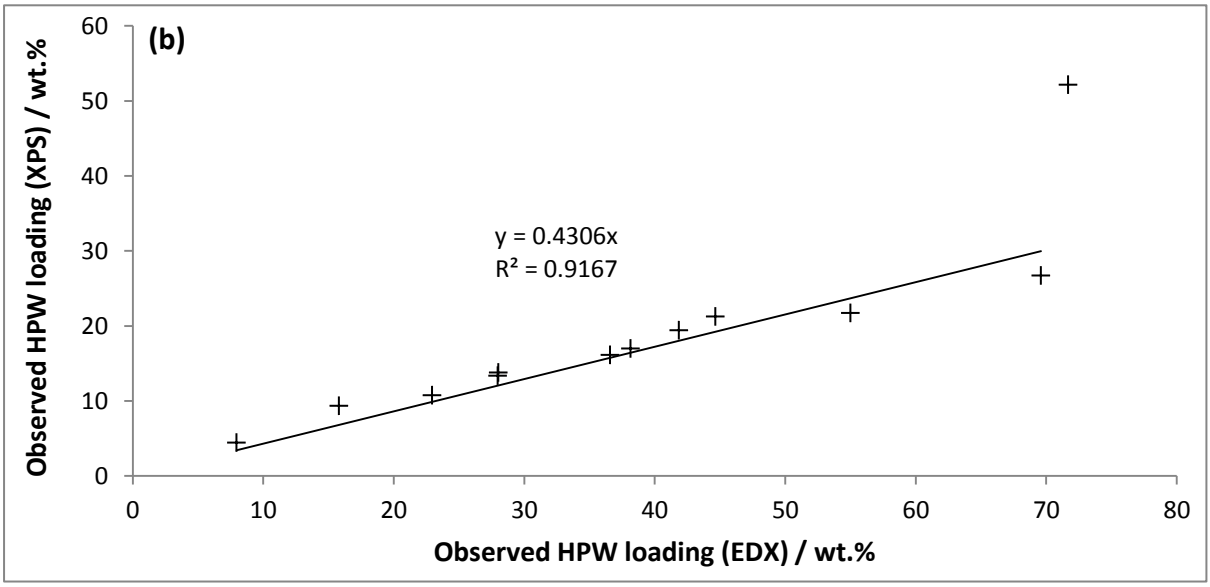

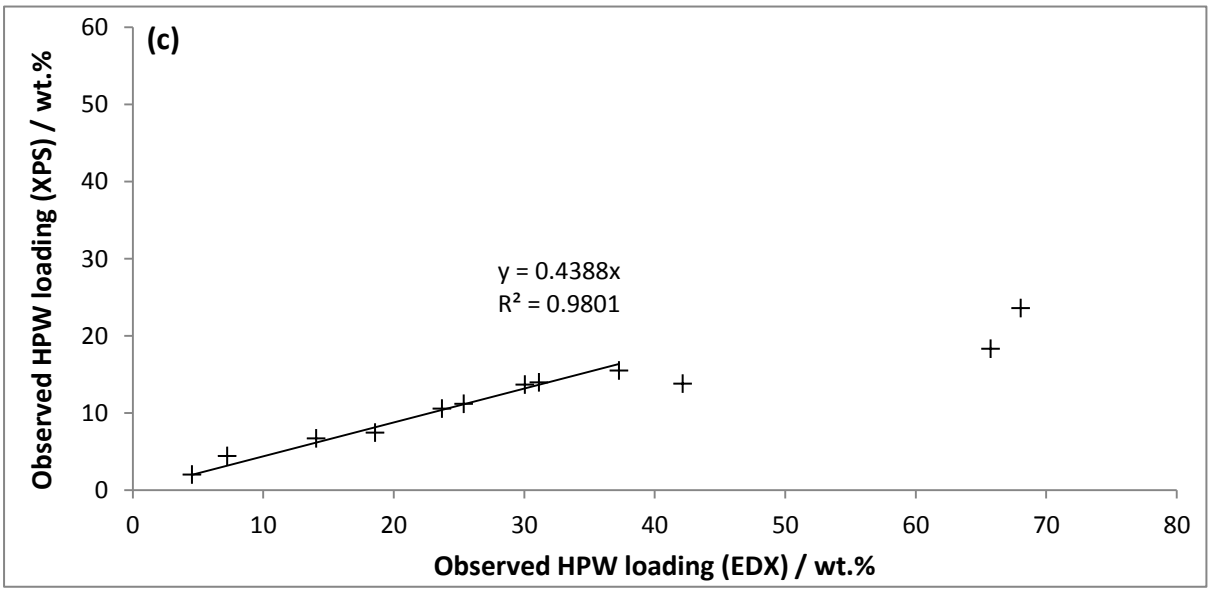

Fig. 30 Loadings of HPW on (a) SBA-15, (b) KIT-6 and (c) fumed silica, measured by EDX and XPS.

practice, the correlation between EDX and XPS results is similar for all supports, suggesting that particle size variations are almost fully compensated for by differences in surface coverage.

The supported CsPW catalysts exhibit larger particles than the HPW catalysts (section 3.4). Moreover, Keggin units are packed more closely (section 3.2) and tungsten atoms are surrounded by heavy caesium ions, instead of the weakly absorbing water molecules in pure HPW. Thus, according to the above arguments, the difference between nominal loadings and estimates from XPS should be greater for a supported CsPW catalyst than a comparable HPW-based material. In reality, XPS delivers loading values for the CsPW catalysts which are almost equal to the EDX measurements (Fig. 31). This could suggest that CsPW more strongly favours deposition on the external surface of the support particles, such that a greater proportion of the catalyst is accessible to XPS analysis.

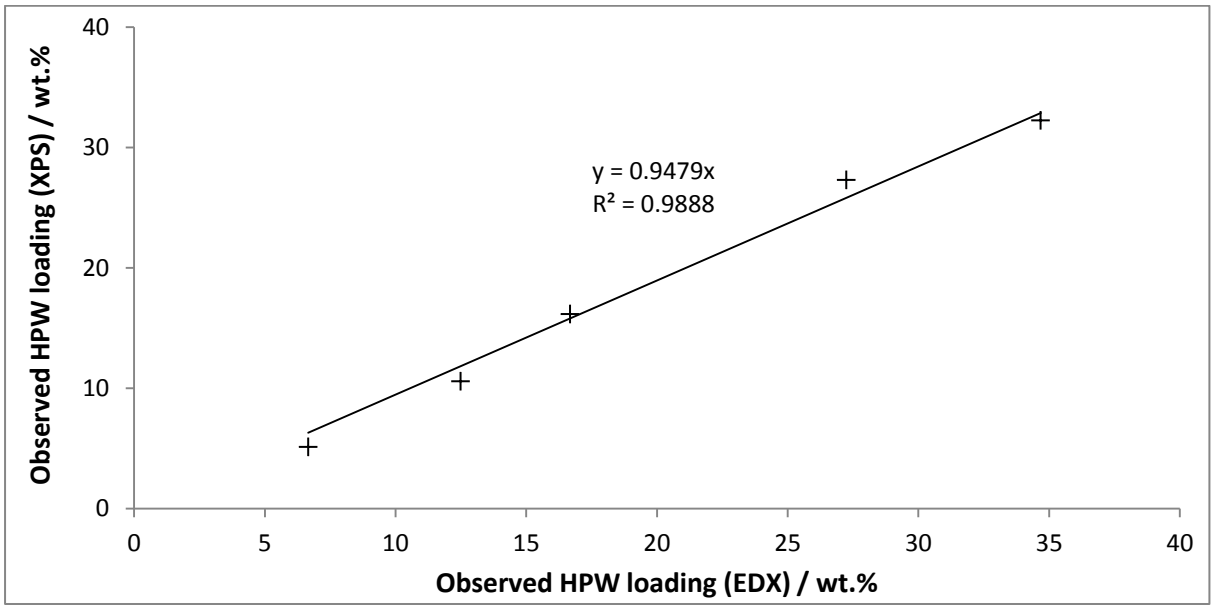

Fig. 31 Loadings of HPW in SBA-15-supported CsPW catalysts, measured by EDX and XPS.

Although it is typically a minor effect, contamination may also influence XPS measurements. As illustrated in Fig. 32(a), most of the catalysts analysed contain 0.5 – 6 wt.% carbon and 10 – 20 wt.% more oxygen than would be predicted from the molar concentrations of silicon and tungsten (assuming these elements are present only as SiO_2 and HPW). The carbon signal is likely due to adventitious carbon adsorbed during the XPS experiment, while the excess oxygen may be attributed to humidity. Some methanol may also be present from the catalyst preparation. HPW loadings without the contributions of these species are shown in Fig. 32(b). Correction evidently makes little difference to the overall trends in the data, but does serve to uniformly increase the loading values, thus improving the match with EDX measurements.

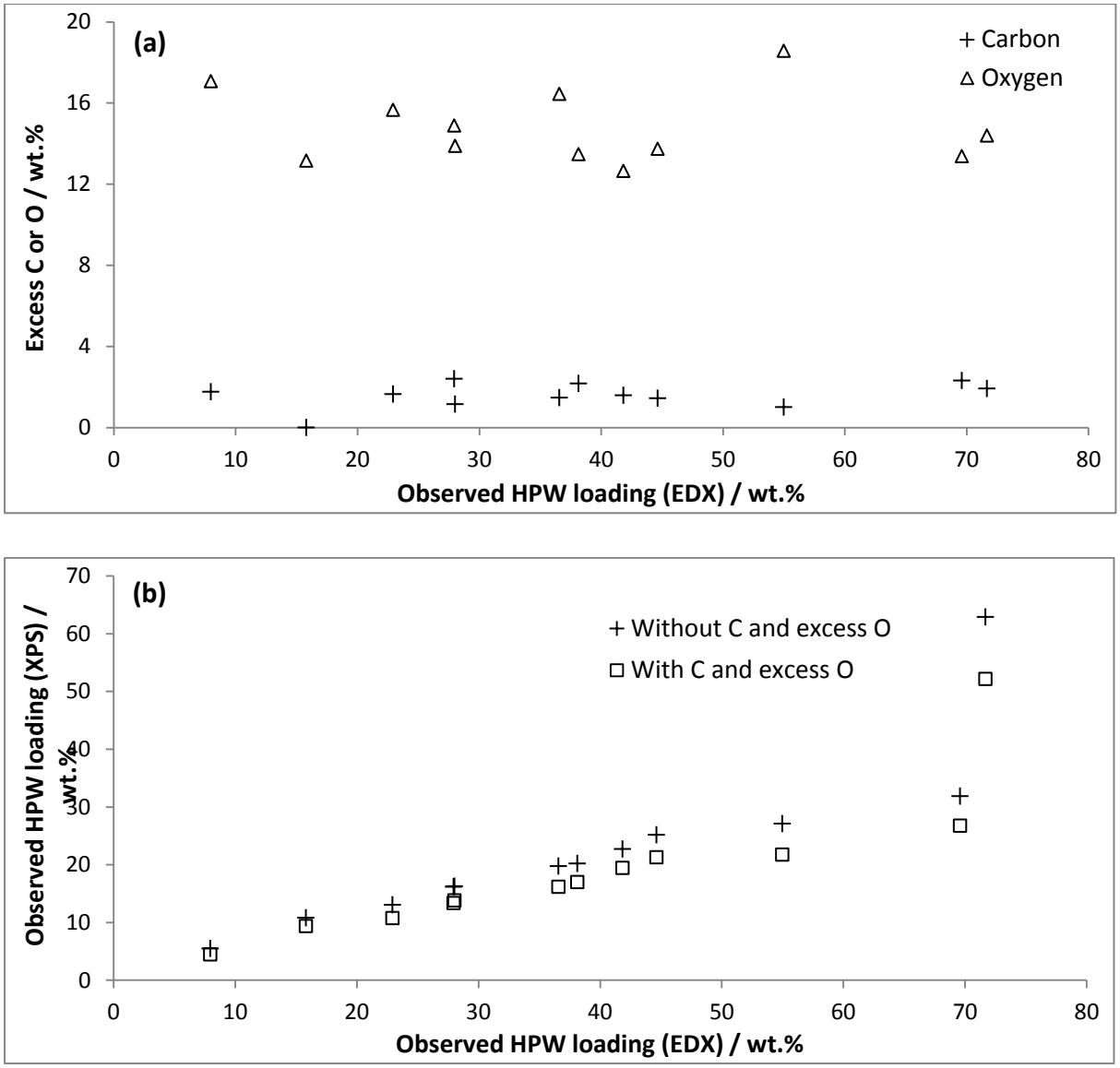

Fig. 32 (a) Loadings of O and C in KIT-6-supported HPW catalysts, and (b) HPW loadings in the absence of these contributions.

3.4 Particle size and pore-blocking effects

The average size of crystallites in a sample, *D*, can be estimated from PXRD data using the Scherrer equation:[96]

$$D = \frac{0.9\lambda}{\sqrt{B^2 - S^2}\cos\theta} \qquad \text{(Eq. 8)}$$

where λ is the wavelength of X-ray radiation used (1.5418 Å for Cu Kα), *S* is an approximation of the instrumental broadening of peaks in the diffraction pattern, θ is the Bragg angle of a peak and *B* is the corresponding full-width at half-maximum (FWHM). The Scherrer equation does not provide any

information about particle shape; is biased towards larger particle sizes, due to the dependency of peak intensities on the number of unit cells parallel to the diffracted beam axis; and cannot be applied accurately to particle sizes much outside the range 5 – 25 nm. In addition, the equation provides no indication of the particle size distribution, and thus does not guarantee that a large number of crystallites exhibit sizes close to the estimated average. Nonetheless, Scherrer analysis is a useful tool for gauging qualitative trends in particle sizes.

For all catalysts where peaks could be resolved (i.e. all materials except 10% HPW on KIT-6), Eq. 8 was applied to a set of the most intense peaks. The five peaks consistently analysed were those with *N* values of 8, 10, 12, 22 and 50. *D* values were calculated for each peak and weighted by peak area before computing their average. The variation in *D* throughout each catalyst series is displayed in Fig. 33.

The HPW catalysts supported on SBA-15 and KIT-6 exhibit similar particle sizes of 6 – 9 nm. Generally, these particle sizes do not vary significantly with loading, though a sharp increase is observed at the highest loading in both series. The dimensions of the CsPW catalysts are comparable (8 – 11 nm) and also show little variation with respect to loading. By contrast, supporting HPW on fumed silica produces relatively large particles (12 – 21 nm) that gradually increase in size as more HPW is incorporated. That particle sizes vary only weakly with HPW content suggests that the major factors affecting crystallite growth are the compositions of the catalyst and support. Differences between catalysts may be attributed to thermodynamic parameters, such as the catalyst-support interaction strength, or kinetic parameters, such as the rate and reversibility of particle growth. It is not possible to investigate these parameters by PXRD, but other techniques (see sections 3.5 and 3.6) may offer additional insight.

Scherrer analysis can only account for crystallites large enough to contribute to the observed PXRD pattern. Moreover, it provides no information about particle shape, so is not directly indicative of the presence or absence of pore blocking. Indeed, although Scherrer particle sizes on SBA-15 and KIT-6 consistently exceed the modal pore diameters of these supports, TEM images of the pores show no evidence of large internal or external HPW deposits. It may be inferred that HPW is primarily deposited in thin, uniform layers on the silica surfaces. The magnitude of the Scherrer measurements likely reflects extended particle growth in one or two dimensions, with relatively minor contributions from large, three-dimensional crystallites. As will be discussed later (section 3.7), this conclusion is consistent with the observed variation in catalytic activity, which can be adequately explained at loadings less than 40 wt.% without taking into account differences in the apparent sizes of HPW particles.

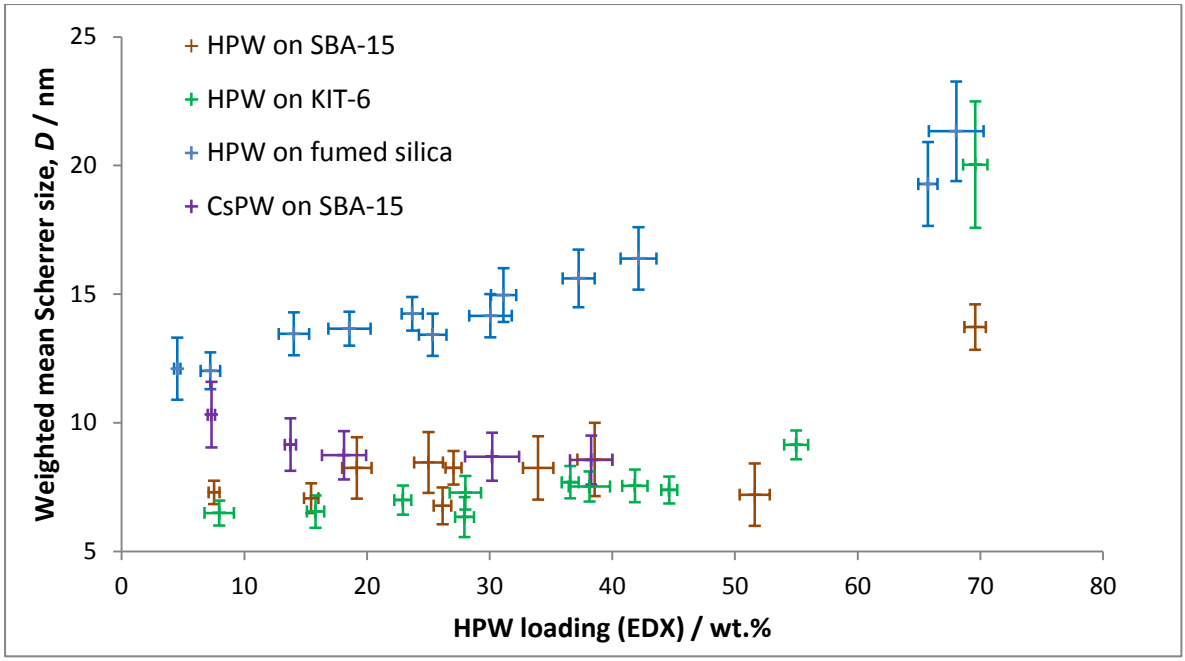

Fig. 33 Average Scherrer particle sizes of HPW on SBA-15, KIT-6 and fumed silica, and CsPW on SBA-15.

As mentioned previously, the intensity of a diffraction signal is related to the number of unit cells in the corresponding crystallites. Thus, the areas of the peaks in a PXRD pattern should provide a measure of the quantity of crystalline material present in the sample. Interestingly, total peak areas in this study scale with EDX loadings in a linear fashion (Fig. 34). These trends suggest that increasing the HPW loading affects the number of HPW crystallites but has little impact on their average size. Accordingly, the data support the conclusions drawn from Scherrer analysis: except at high loadings, the sizes of both internal and external HPW deposits depend only on the nature of the silica support.

Deposition in pores may be probed more directly using porosimetry.[83] In this technique, a sample is degassed by heating under vacuum, then exposed to an analyte gas (typically nitrogen) at low pressure and constant temperature (77 K). The pressure is increased in stages, and after each interval the change in pressure is measured to determine the volume of gas adsorbed on the sample. Upon reaching a value close to atmospheric pressure, the pressure is reduced, again in stages, and the volume of liberated gas measured after each interval. In this way, an isotherm is generated from which the pore properties of the material can be estimated.

To evaluate the surface area of a material, porosimetry data was processed using the Brunauer-Emmett-Teller (BET) approach. This calculation utilises low-pressure adsorption data and is based on an extension of the Langmuir adsorption model, introducing approximations to account for multilayer adsorption of the analyte gas. Another model, the Barret-Joyner-Halenda method, can be used to obtain estimates for pore volume and diameter from either adsorption or desorption data.

In this study, as in many others, the BJH method was applied to the desorption branches of isotherms, as this approach provides the most conservative estimates of pore diameter. Finally, a technique known as t-plot statistical thickness analysis was applied to the adsorption data at intermediate relative pressures (0.2 – 0.5) to estimate the contribution of micropores to the areas and volumes of the catalysts.

The isotherms and BJH pore size distributions of the different silica supports are shown in Fig. 35. SBA-15 and KIT-6 display type IV isotherms, indicative of multilayer deposition with complete pore-filling at high relative pressures. By contrast, the isotherm of fumed silica is of type II: adsorption plateaus at intermediate pressures but proceeds to increase without limit, suggesting that the material contains pores of many different sizes, including large mesopores and macropores. BJH analysis confirms the existence of a variety in fumed silica, while SBA-15 and KIT-6 exhibit narrow distributions of pore sizes, with diameters concentrated around 5.9 and 5.3 nm respectively. The surface areas and pore volumes of the ordered silicas are very similar and, as expected, much larger than the values for fumed silica. However, as a fraction of the total porosity, the ordered silicas exhibit much more microporosity, which may be attributed to disordered fractures between the major, uniform channels.

The HPW catalysts supported on KIT-6 and SBA-15 exhibit similar desorption isotherms. As loading increases, surface area (Fig. 36) and pore volume (Fig. 37) are found to decrease more rapidly than would be expected if HPW and SBA-15 were physically mixed, indicating that HPW is being accommodated in the pores of the support. The rates of decrease generally fall as loading increases, but remain approximately constant at intermediate loadings (30 – 40 wt.%). The micropore area and volume also decrease up to 15 – 20 wt.%, but plateau or rise if loading is increased further (Fig. 38). The results are indicative of sequential filling of pores in order of size: porosity decreases rapidly as micropores are filled, but varies less as, subsequently, the catalyst is deposited in larger pores. The onset of linear variation likely corresponds to the filling of the major, monodisperse channels of the supports, as the porosity of similarly sized channels should (in the absence of pore-blocking effects or the filling of other pores) vary in proportion to the mass of HPW deposited. The micropores not filled are likely those too small to accommodate a Keggin unit (diameter 1.2 nm), while the increase in microporosity at high loadings may be attributed to the creation of small pores as larger pores become constricted. Micropores may also be generated within or between HPW deposits, as the large Keggin units are unlikely to pack perfectly within the narrow pores of the support.

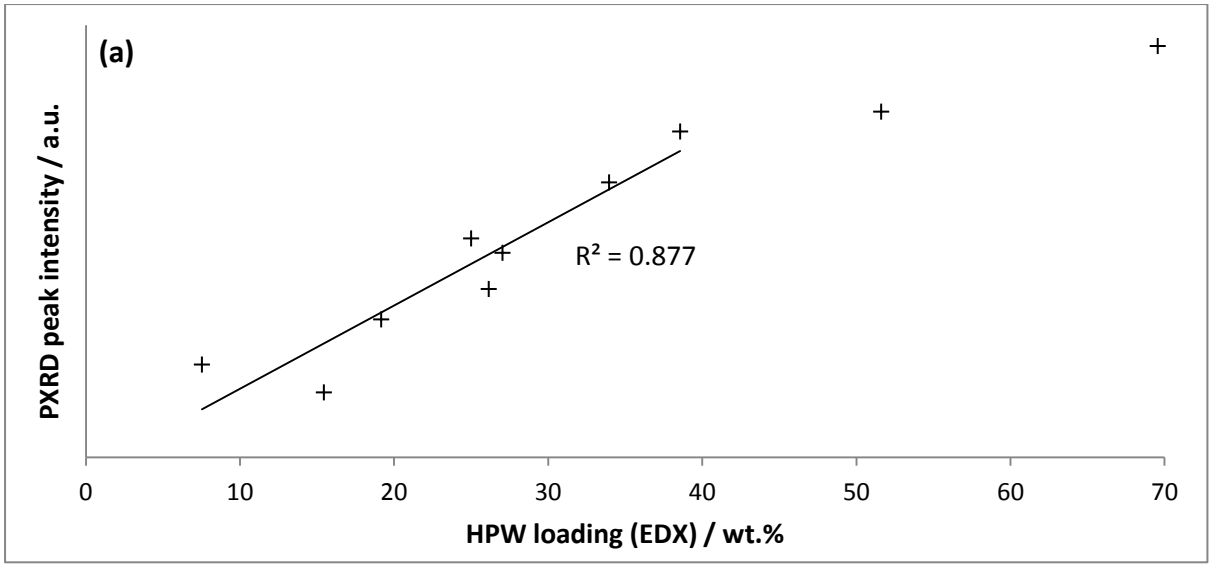

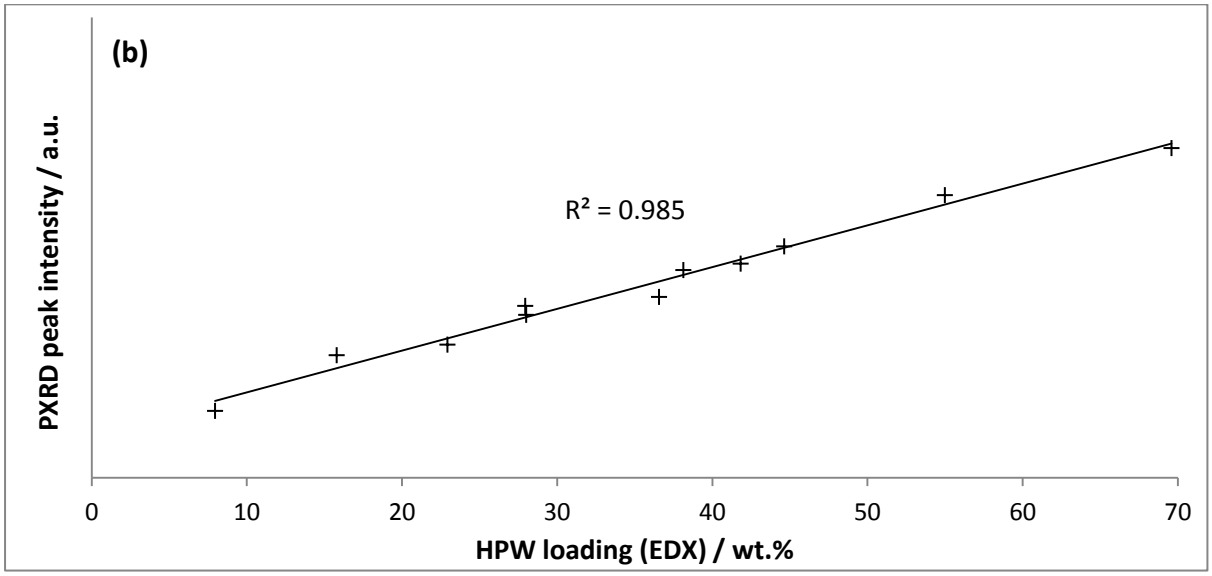

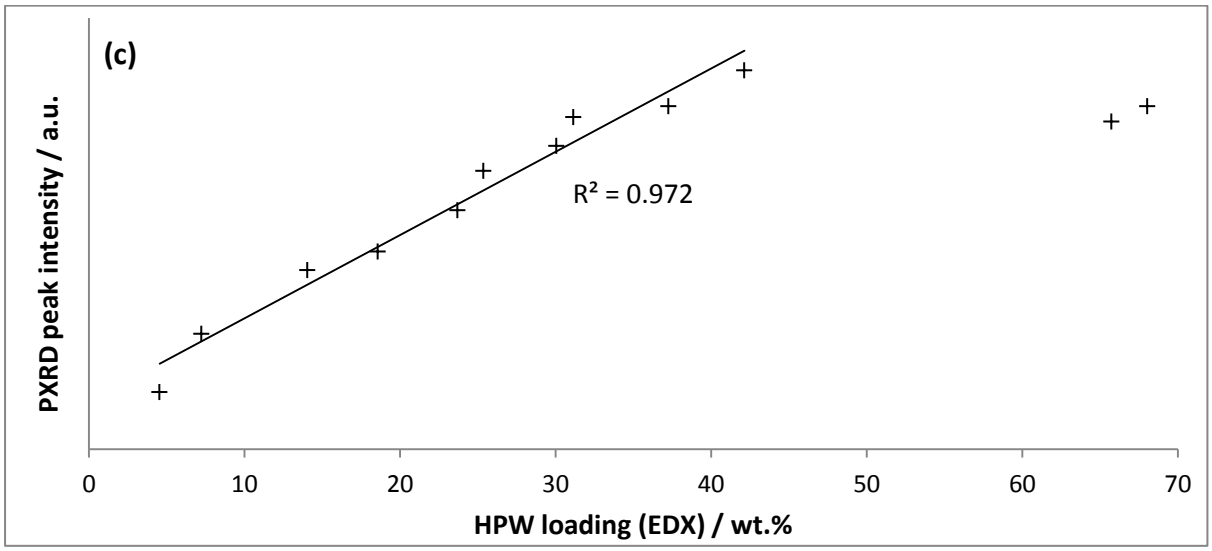

Fig. 34 Variation of PXRD peak intensities with HPW loadings on (a) SBA-15, (b) KIT-6 and (c) fumed silica. Peak areas are not normalised, as the same sample volume was used for each catalyst.

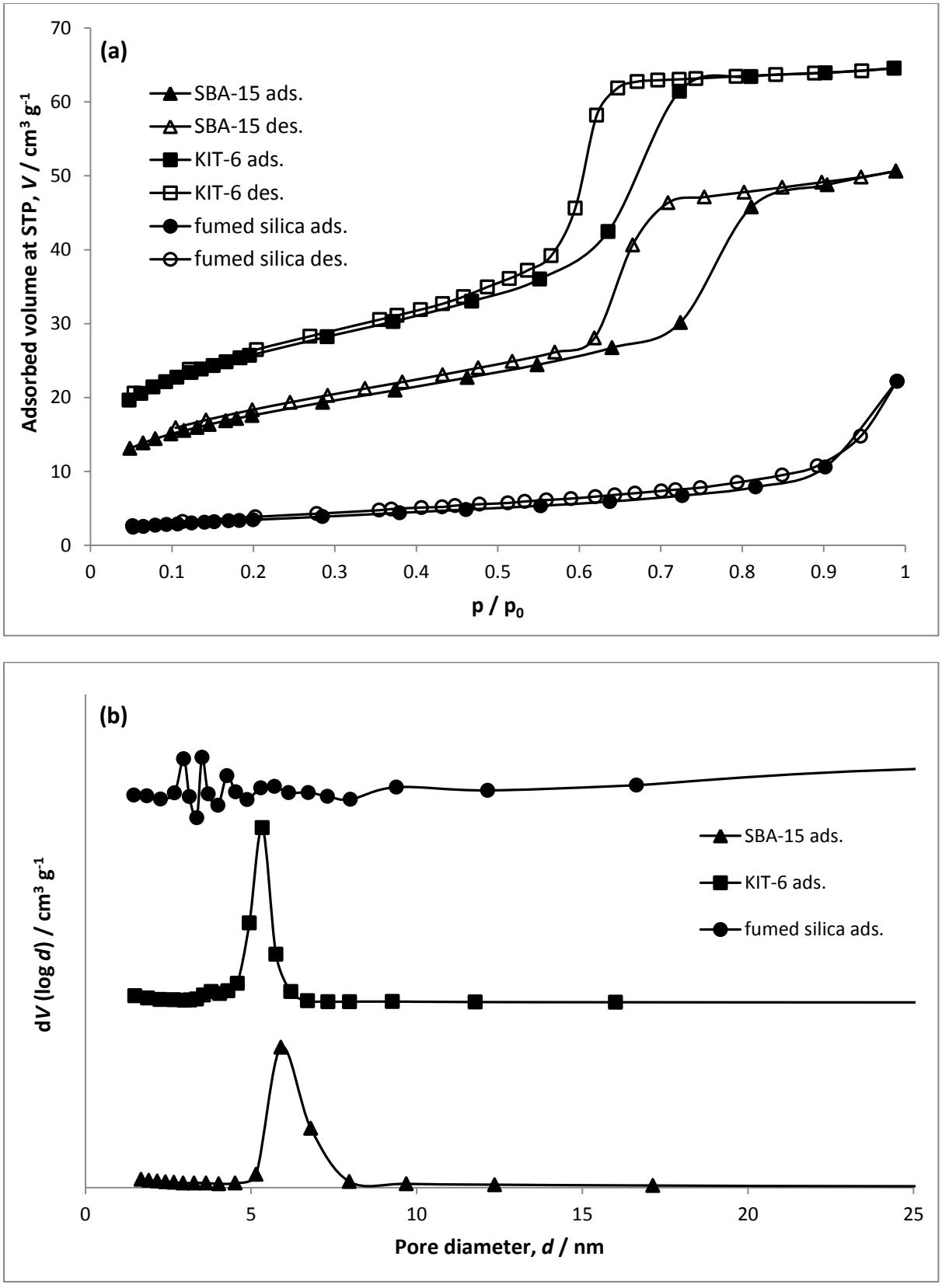

Fig. 35 (a) Nitrogen adsorption and desorption isotherms of the silica supports at 77 K; (b) pore-size distributions of the silica supports calculated using the BJH model.

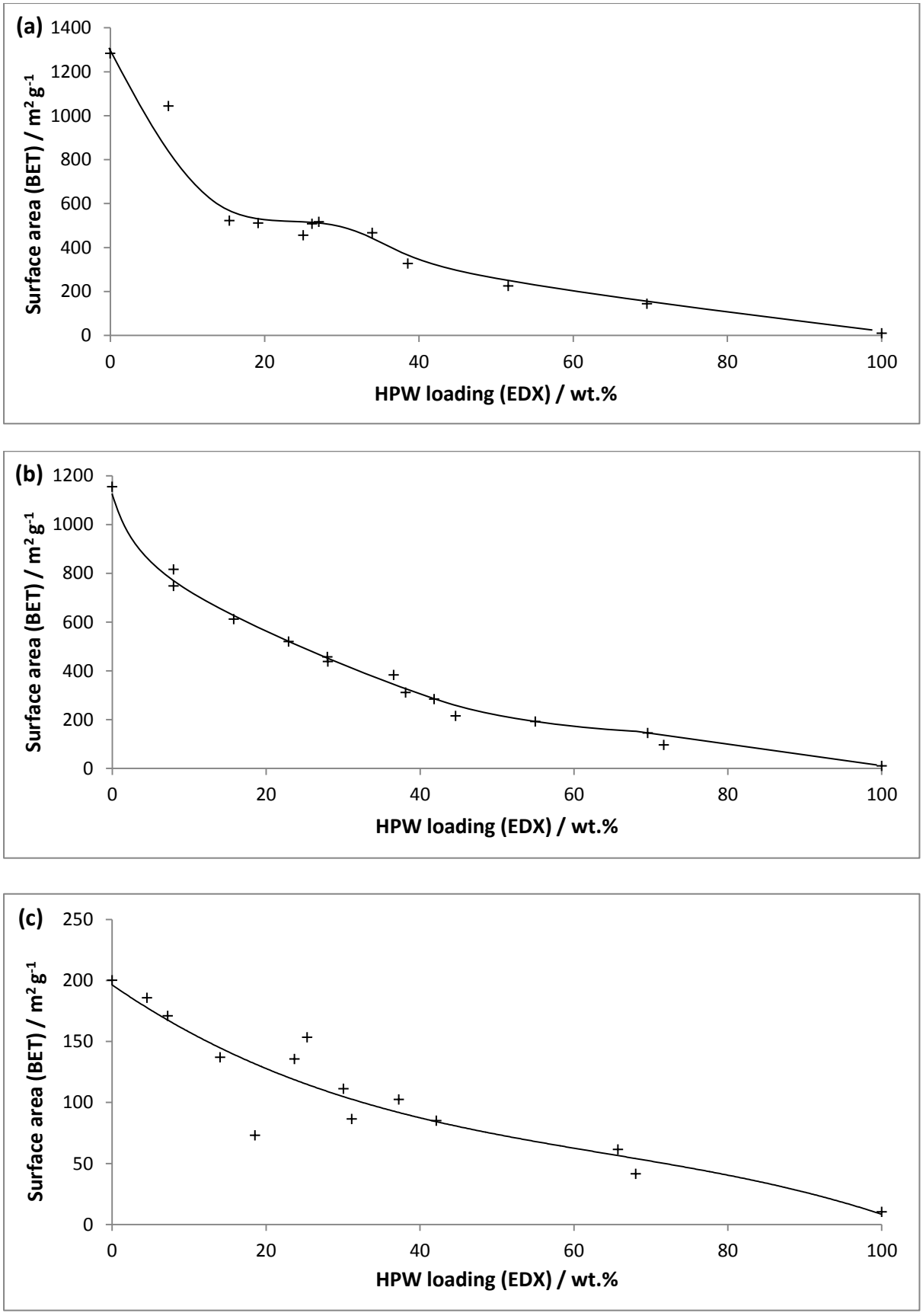

Fig. 36 Variation in surface area (BET) of HPW on (a) SBA-15, (b) KIT-6 and (c) fumed silica. Lines are included to guide the eye only. Note physical mixtures give areas proportional to loading.

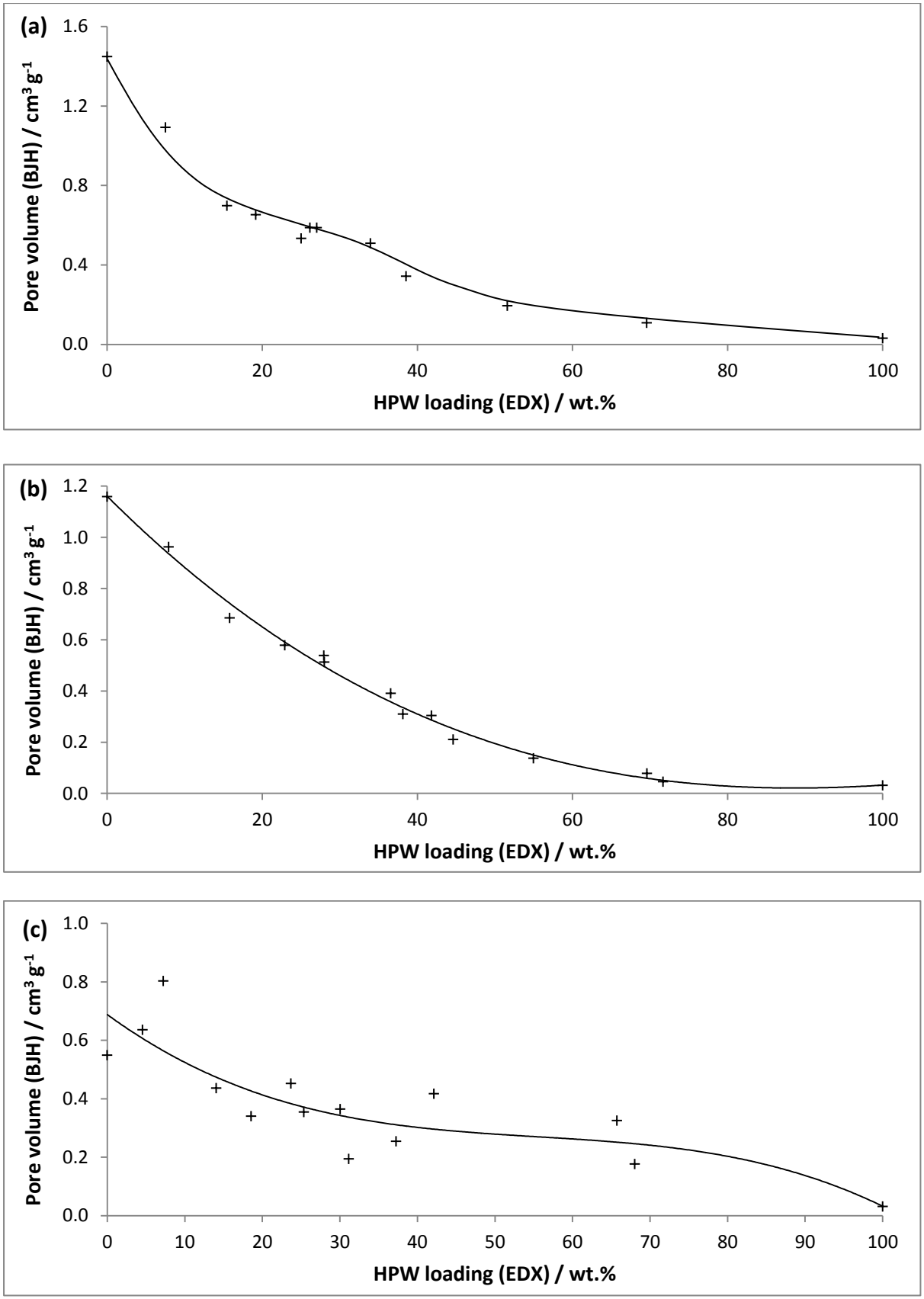

Fig. 37 Variation in pore volume (BJH) of HPW on (a) SBA-15, (b) KIT-6 and (c) fumed silica. Lines are included to guide the eye only. Note physical mixtures give volumes proportional to loading.

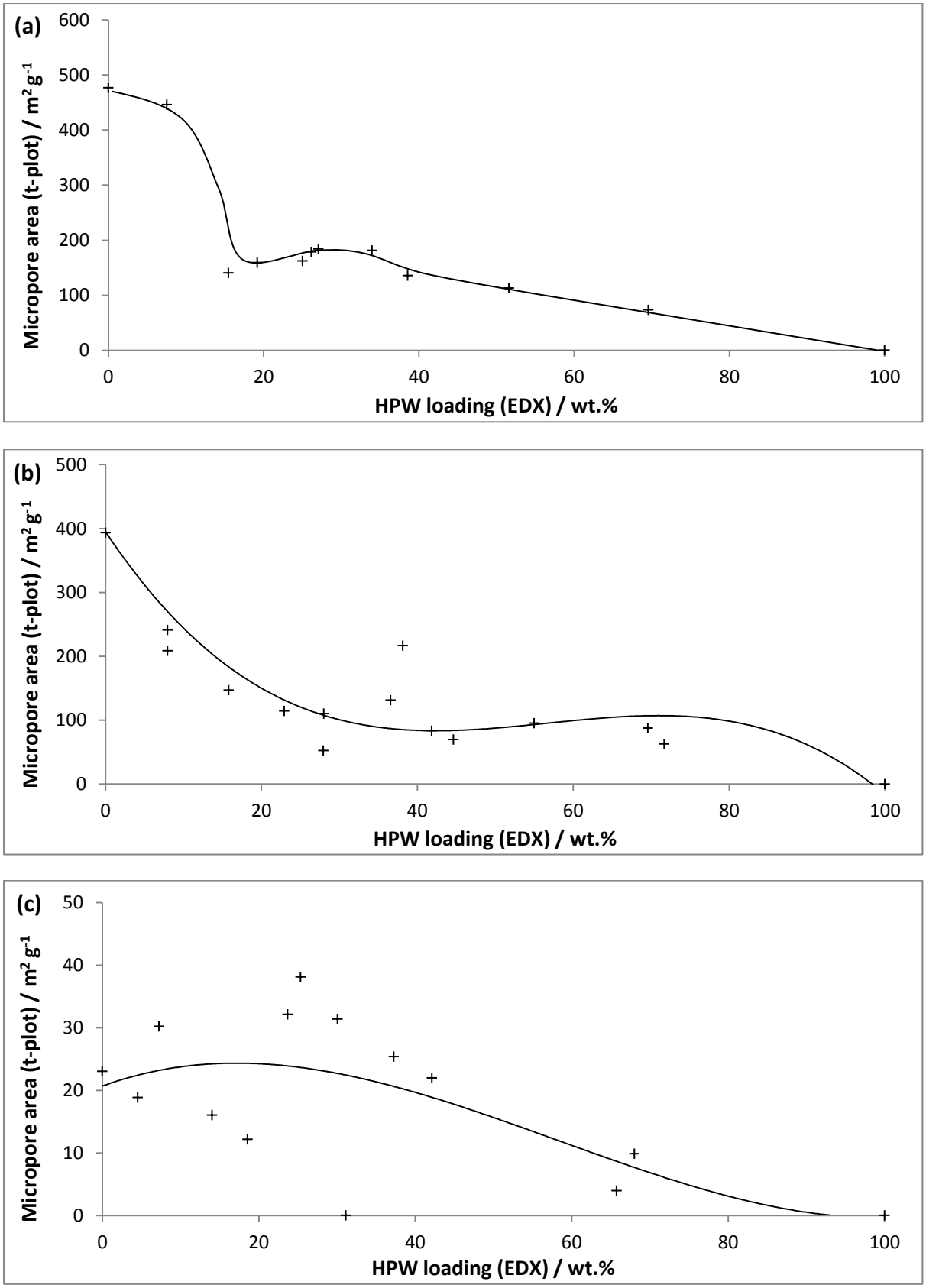

Fig. 38 Variation in micropore area (t-plot) of HPW on (a) SBA-15, (b) KIT-6 and (c) fumed silica. Lines are included to guide the eye only. Due to the nature of the t-plot analyses, micropore volumes exhibit identical trends.

When HPW enters a porous support, it occupies a fraction of the pore volume and thus reduces the volume measured in porosimetry. To determine whether occupation of space by HPW may account for all the volume lost upon impregnation, the total volume of HPW was calculated for each catalyst and subtracted from the pore volume of the pure support. Pore volumes were normalised to the mass of support, and HPW volumes calculated using densities estimated from PXRD data (section 3.2). Fig. 39 displays the catalyst pore volumes that remain unaccounted for in this approach. Clearly, in both KIT-6 and SBA-15, the volume lost during impregnation always greatly exceeds the volume of HPW added, suggesting that the majority of inaccessible pore space is actually free of HPW deposit.

Pore blockage may occur if an accumulation of catalyst completely fills the cross-section of the pore. Multiple blockages can greatly reduce the observed pore volume, as the space between the blockages may be inaccessible to adsorbates even if it is mostly free of deposit. The data in Fig. 39 loosely represent the volumes lost in this manner. Generally, pore blockage increases with loading, but the rate of increase is notably smaller for loadings between 15 and 35 wt.%. Indeed, in the SBA-15 series, pore blockage remains roughly constant within this range. This trend reinforces the theory that HPW is deposited predominantly as a monolayer at intermediate loadings. Since the diameter of a Keggin unit is much less than the average pore diameter, growth of the monolayer without deposition of additional layers should not lead to a significant increase in the number of channels blocked.

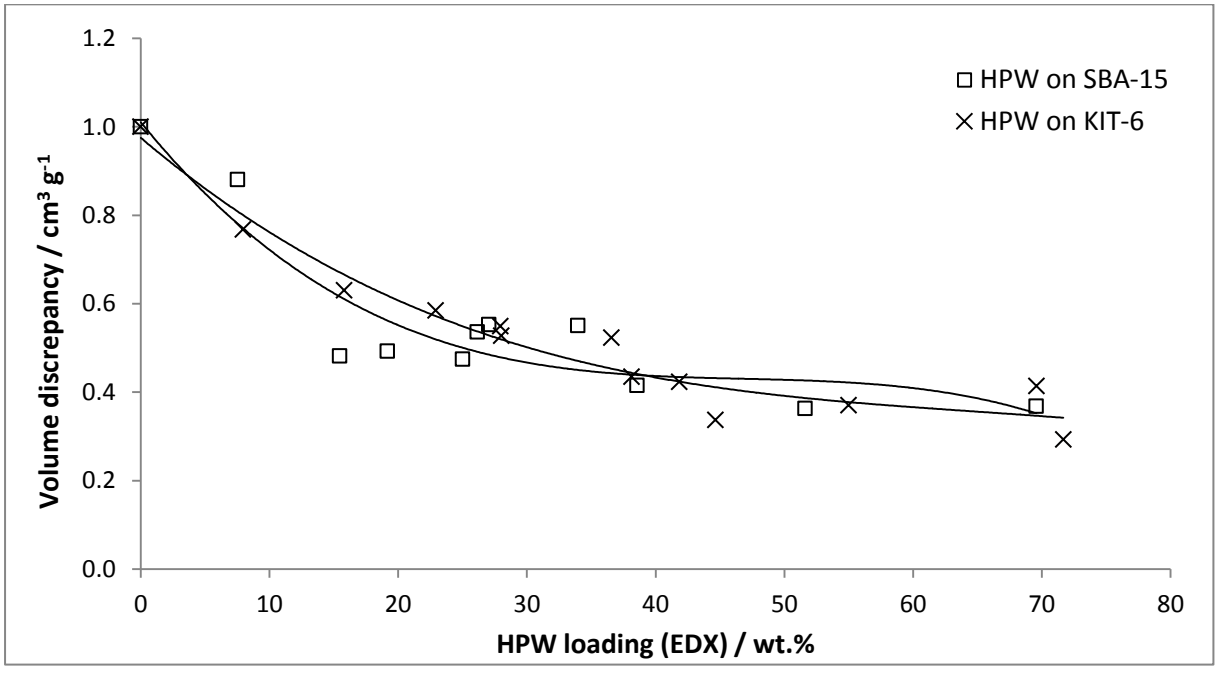

Fig. 39 Losses of pore volume in silica-supported HPW catalysts not accounted for by the volumes of HPW added.

To obtain more accurate estimates of pore blocking, a support may be considered which exhibits an initial volume V_0, and a volume V_{cat} when loaded with HPW. The volume of HPW can be estimated from its mass and density, but this calculation does not account for the proportion of catalyst sequestered by inaccessible pores. It is simplest to assume that HPW is distributed uniformly in the pore, and that blockages are so small as to have no effect on this distribution beyond rendering a region of pore space inaccessible. This model is supported by the data: although pore blocking clearly increases with loading, the modal pore diameter does not vary (Fig. 40), suggesting that local constrictions of the pores (i.e. blockages) are small and infrequent.

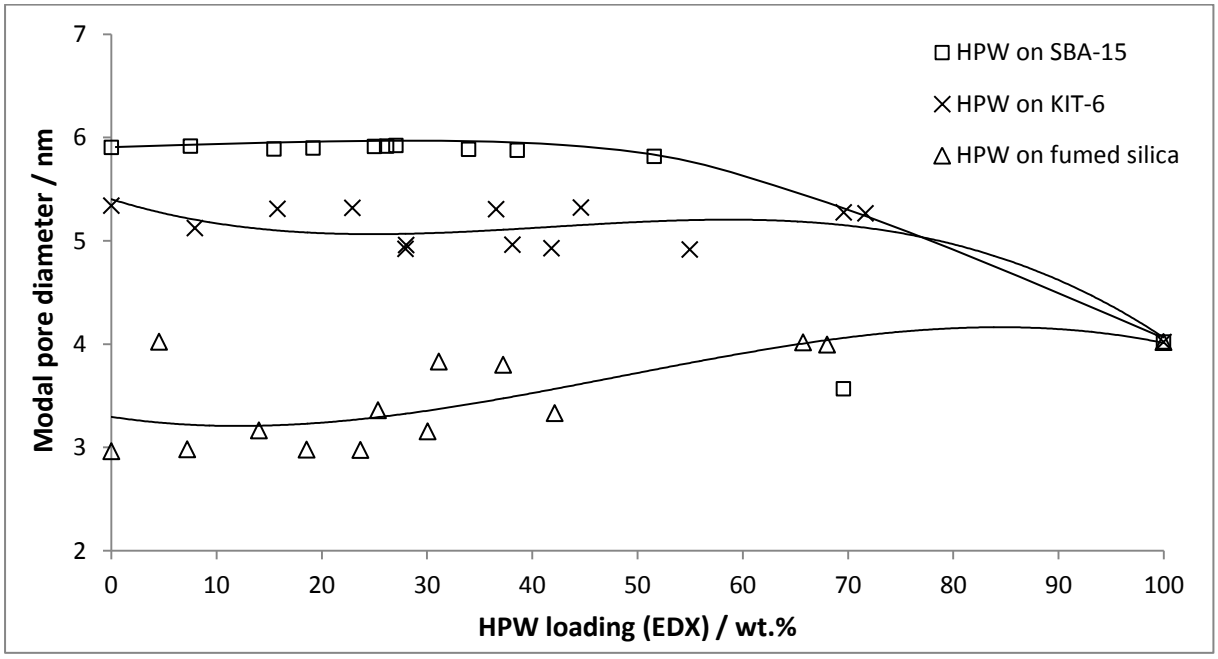

Fig. 40 Variation in modal pore diameter with HPW loading on SBA-15, KIT-6 and fumed silica.

The volume of HPW deposits in a supported catalyst can be simply and accurately calculated, so their contribution to pore volume can be incorporated into a quantitative estimate of pore blocking. If P is the proportion of pores blocked, V_{HPW} the total volume of HPW and V_{acc} the volume in accessible channels only:

$$V_{acc} = (1 - P)V_{HPW} \quad \text{(Eq. 9)}$$

$$P = \frac{V_0 - V_{cat} - V_{acc}}{V_0} = \frac{V_0 - V_{cat} - (1 - P)V_{HPW}}{V_0} \quad \text{(Eq. 10)}$$

$$P = \frac{V_0 - V_{cat} - V_{HPW}}{V_0 - V_{HPW}} \quad \text{(Eq. 11)}$$

In these calculations, all volumes are normalised to the mass of support. The fractional weight loading measured by EDX, *W*, is used for scaling. For example, the catalyst pore volume per unit mass, V'_{cat}, is converted to the volume per mass of catalyst, V_{cat}, by dividing by *(1-W)*:

$$V_{cat} = \frac{V'_{cat}}{1 - W} \quad \text{(Eq. 12)}$$

Similarly, V_{HPW} is estimated from the measured *HPW* density, ρ, and normalised according to Eq. 13:

$$V_{HPW} = \frac{W}{1 - W}\left(\frac{1}{\rho}\right) \quad \text{(Eq. 13)}$$

V_0 is the measured pore volume of the pure support and thus requires no additional scaling.

For catalyst applications, it is more useful to estimate the fraction of pore volume which remains accessible to adsorbates. A typical measure is the normalised pore volume, *NPV*. This is simply the normalised pore volume of the catalyst as a fraction of the support volume, with no correction for the volume of material added to the pores:

$$NPV = \frac{V_{cat}}{V_0} \quad \text{(Eq. 2)}$$

A corrected version of this ratio, NPV_{corr}, may be obtained by converting *P* (Eq. 11) to a comparable estimate of the fraction of pores accessible to adsorbates:

$$NPV_{corr} = 1 - P = \frac{V_{cat}}{V_0 - V_{HPW}} \quad \text{(Eq. 14)}$$

Clearly, correcting *NPV* serves to reduce the estimate of pore blocking. However, the correction is only significant if V_{HPW} and V_0 are comparable in magnitude. It should further be noted that NPV_{corr} may still contain significant error, due to the simplifying assumptions made in the derivation: namely, that HPW is deposited uniformly throughout all pores (regardless of pore size) and that every unit of pore space has the same likelihood of occupation, even if it is far from the surface of a pore wall.

In reality, the activity of a catalyst rises in proportion to the area of the material. It would therefore be more useful to estimate the effect of pore blocking on the catalyst area. Unfortunately, the geometry of the HPW deposits cannot be accurately known, so their area cannot be estimated in the manner of the volume correction above. It is worth noting, however, that if HPW is deposited uniformly in pores of equal size, the fractional loss of pore volume due to blocking should be equal to the fractional loss of surface area. Thus, *P* should serve as a reasonable estimate of pore blocking

effects in materials with highly uniform pores, such as SBA-15 and KIT-6. The similarity between *NPV* and its area-based equivalent, *NSA*, for the SBA-15 and KIT-6 catalysts studied is shown in Fig. 41.

The values of NPV_{corr} calculated for catalysts on SBA-15 and KIT-6 are shown in Fig. 42. The displayed errors are calculated from the errors in the input parameters of Eq. 14, so do not take into account inaccuracies in the model. However, it should be noted that in most cases V_{HPW} is much smaller than V_0, so NPV_{corr} is likely to be accurate even if the assumptions underlying the correction are not completely valid. This is illustrated by the close correspondence between NPV_{corr} and *NPV* over the range of loadings tested. The NPV_{corr} plots are likewise similar to the data given in Fig. 39: pore blocking increases with loading, but varies relatively weakly between loadings of 15 and 35 wt.%.

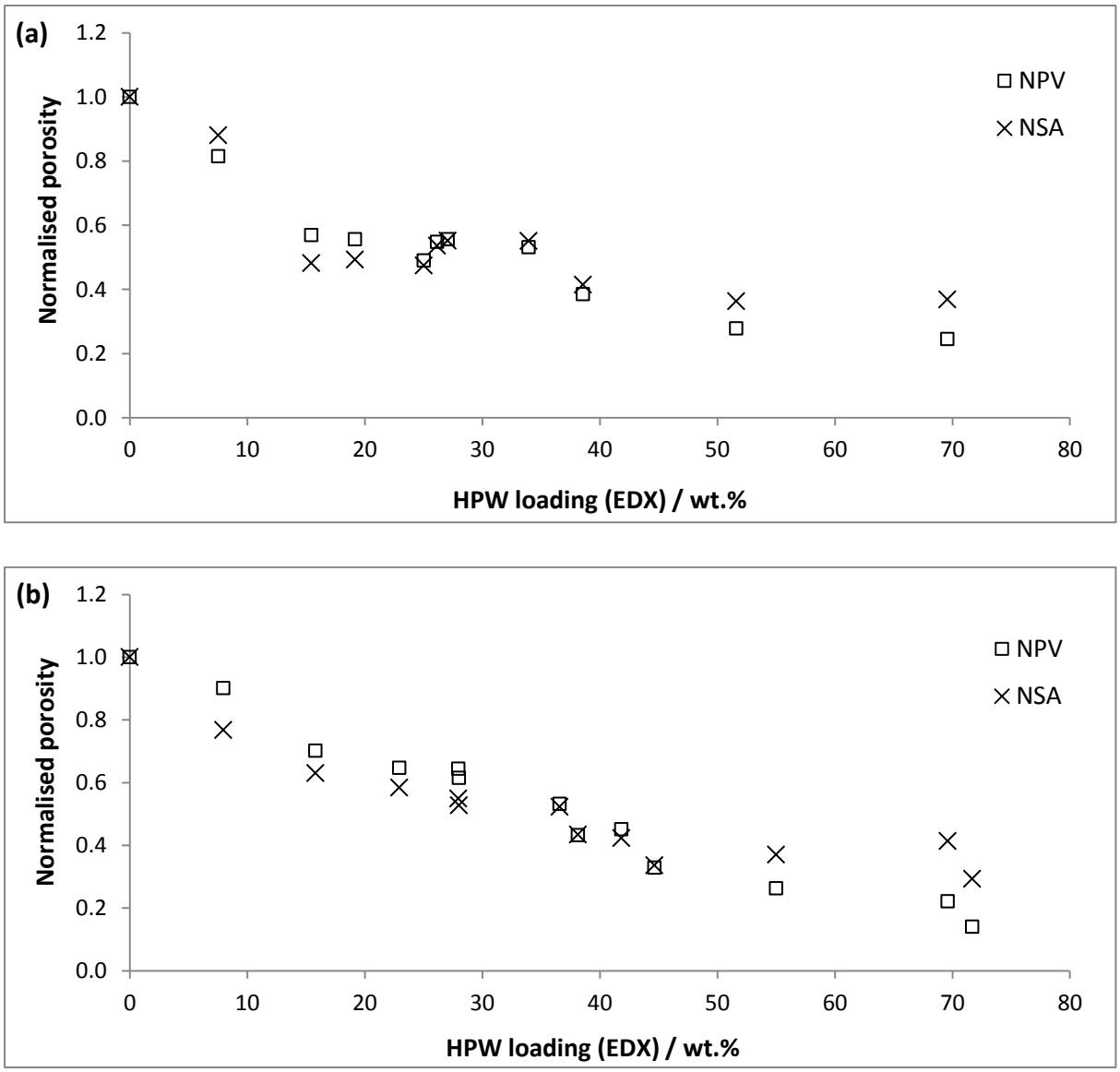

Fig. 41 *NSA* and *NPV* values of HPW catalysts on (a) SBA-15 and (b) KIT-6. Errors are similar to those illustrated in Fig. 42 overleaf, but are omitted here for clarity.

Notably, pores smaller than 1.2 nm in diameter are unable to accommodate Keggin units. Thus, to improve the NPV_{corr} estimate, it may seem appropriate to exclude micropore contributions from the calculation. Similarly, the assumption that HPW is distributed uniformly within a catalyst only holds if the quantity of HPW in a pore roughly scales with the pore volume. This is true of small pores, but in larger pores the HPW content is more likely to scale with the pore area, which is probably negligible for pores larger than the major mesoporous channels. It may therefore be sensible to also exclude a subset of large pores from the NPV_{corr} calculation. In practice, pore-blocking estimates for highly uniform supports are not significantly affected by such corrections (Fig. 43). For this reason, uncorrected pore volumes were utilised for all calculations in this study.

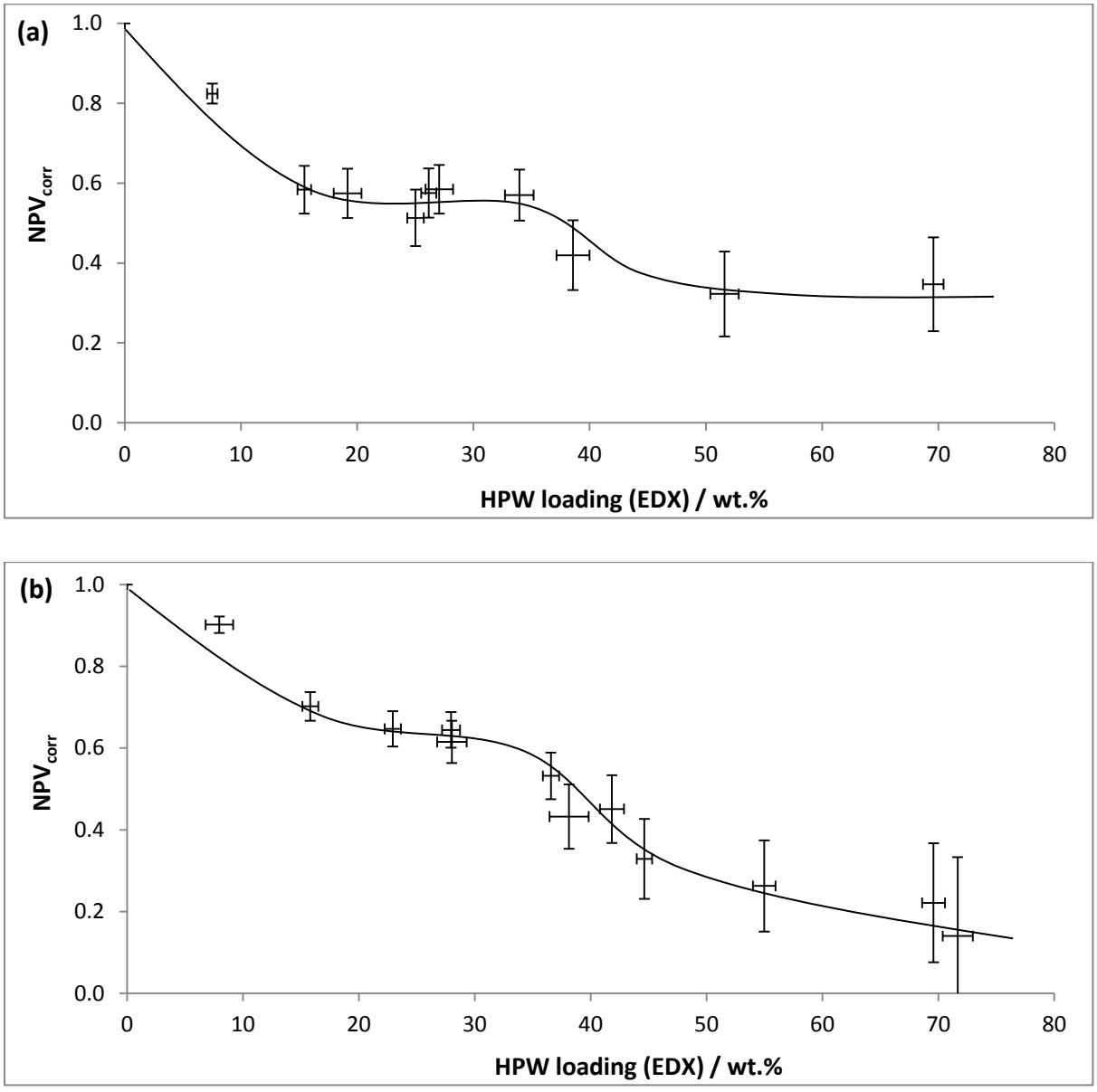

Fig. 42 NPV_{corr} values of HPW catalysts on (a) SBA-15 and (b) KIT-6. Lines are included to guide the eye only. Errors *in* NPV_{corr} values are estimated assuming conservative pore-volume errors of ±10%.

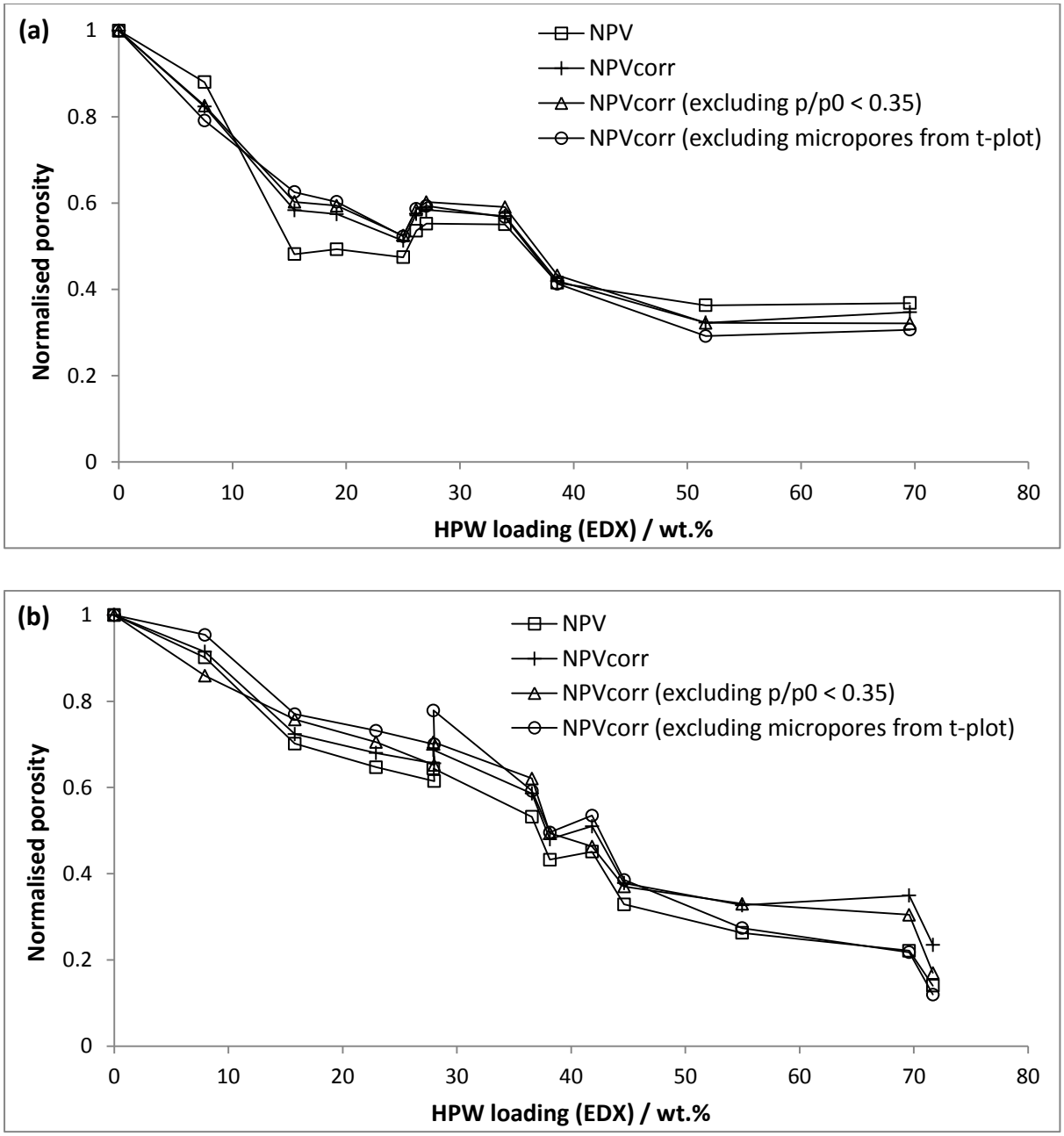

Fig. 43 *NPV* values of HPW catalysts on (a) SBA-15 and (b) KIT-6, illustrating the effects of corrections. Errors are similar to those illustrated in Fig. 43, but are omitted here for clarity.

Given that HPW deposition has little effect on the volume-based estimate of pore-blocking, it is reasonable to assume that most of the difference between *NPV* and *NSA* values is real. As such, these values may be used to estimate the average radius of pores affected by blocking. For cylindrical pores, the average hydraulic radius, R_h, is related to the pore area, *S*, and volume, *V*, via the equation:

$$R_h = \frac{2V}{S} \qquad \text{(Eq. 15)}$$

For the sum of pores rendered completely inaccessible by pore blocking, the pore volume may be expressed:

$$V = (1 - NPV_{corr})V_0 = PV_0 \quad \text{(Eq. 16)}$$

Similarly, the best approximation for *S* is given by:

$$S = (1 - NSA)S_0 \quad \text{(Eq. 17)}$$

Thus the hydraulic radius of these pores can be estimated:

$$R_h = \frac{2(1 - NPV_{corr})V_0}{(1 - NSA)S_0} \quad \text{(Eq. 18)}$$

The variation in R_h with loading for the SBA-15 and KIT-6 catalysts is shown in Fig. 44. In both SBA-15 and KIT-6, R_h is consistently close to the modal pore radius of the support (approximately 3.0 nm in SBA-15 and 2.6 nm in KIT-6) minus the radius of a Keggin unit (0.6 nm), possibly indicating an average deposit thickness of half a unit. Between 15 and 55 wt.%, no significant decrease in R_h is observed with increasing HPW content. This could suggest that after a base monolayer has formed in pores, adding more HPW serves only to increase the proportion of inaccessible pores, rather than incrementally constricting those that remain accessible. This model reflects the similarity between the modal pore diameters of the supports and the diameter of a Keggin unit: if another unit is deposited onto a layer with thickness approximately $r - R_h$ (where *r* is the modal pore radius of the support), the pore becomes blocked and can no longer influence pore-size measurements. Alternatively, R_h may be preserved due to deposition on the external surface of the support. Where pore blocking is estimated to remain constant with respect to loading (Fig. 42), such deposition must be particularly favoured, perhaps as a consequence of restricted diffusion of bulky Keggin units through mesopores that are already narrowed or segmented by catalyst deposits.

While the surface areas and pore volumes of the SBA-15 and KIT-6 supports are similar, their NPV_{corr} plots exhibit significant differences. The KIT-6 catalysts display slightly less pore blocking at low loadings, and the decrease in NPV_{corr} with increasing loading is more consistent: a shallow gradient is observed between 15 and 35 wt.%, whereas the plot for the SBA-15 series displays a pronounced plateau in this region. Such disparities may be attributed to the greater connectivity of the KIT-6 support. In SBA-15, a small number of blockages can prevent access to the majority of a pore's volume, so even partial filling of a set of pores may deliver near-maximal pore blocking. For example, a loading of 15 wt.% HPW represents only a partial monolayer in the major mesopores of the support, but the *NPV* value is almost identical to the value at 35 wt.%. By contrast, many

blockages are needed to create inaccessible voids in KIT-6, as each pore may be reached via multiple routes. Thus, pore blockage increases gradually with the number of blockages, and matches the value in SBA-15 only when the pore connectivities have been reduced to similar levels. At high loadings, the two supports exhibit almost equal *NPV* values, as their ordered mesopores now differ little in their connectivities, and any new pore blockages are predominantly caused by external HPW deposits.

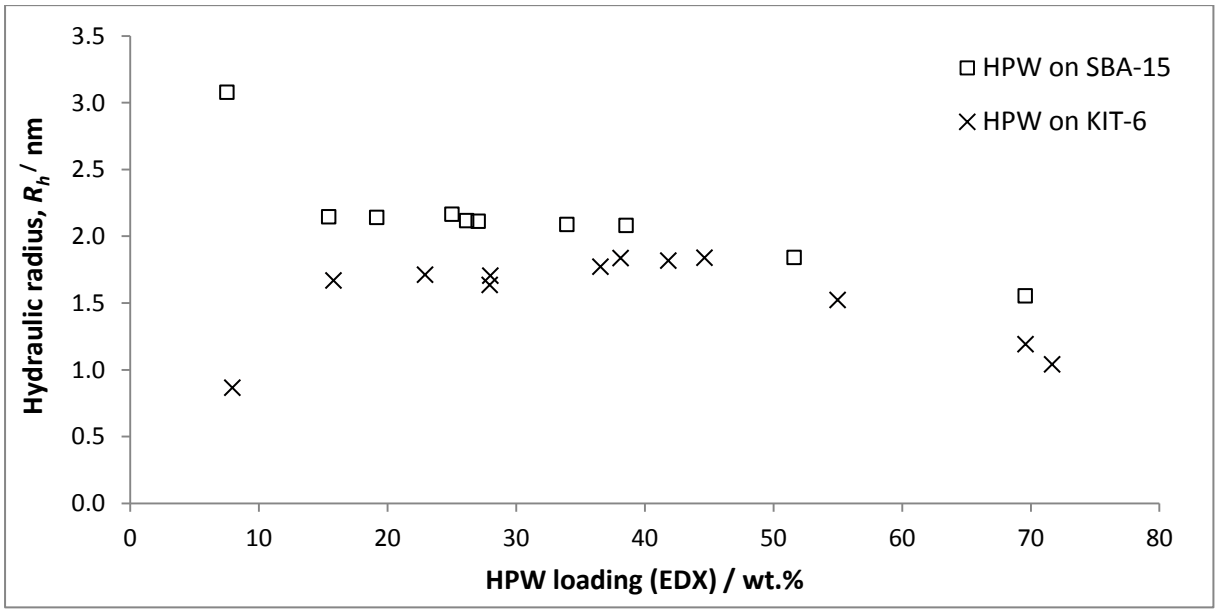

Fig. 44 R_h values of HPW catalysts on SBA-15 and KIT-6.

Impregnation of fumed silica with HPW may also result in pore blocking. Unfortunately, applying Eq. 14 to such systems is problematic, as changes in pore volume are largely due to modifications in particle size and shape, rather than simple filling of internal channels. The effect of HPW addition is therefore complicated: it is possible to envisage mesopore sizes varying with aggregation of coated silica particles, and micropores being generated within the HPW deposits, to replace those filled by Keggin units. Indeed, the pore volumes of the fumed silica catalysts in this study appear to vary randomly with loading, in some cases even exceeding the volume of the pure support (Fig. 37(c)). The trend in micropore volume (from t-plot analysis) is similarly uncorrelated (Fig. 38(c)). Given that the surface areas of the fumed silica catalysts are consistently close to the values that would be obtained if HPW and the support were physically mixed (Fig. 36(c)), pore blocking in these catalysts was assumed to be negligible compared with other factors affecting catalytic activity, such as particle size. It is worth noting that even if pore-blocking estimates could be obtained for these materials, they would be highly inaccurate and of limited use, since the quantitative methods outlined above are only reliably applicable to uniform pore networks.

3.5 X-ray photoelectron spectroscopy (XPS) analysis

The distribution of catalytic species can be investigated by XPS.[107] As shown in Fig. 45, the W signals of the supported catalysts can be decomposed into two sets of doublets, each corresponding to a different chemical environment.[38] The lower-energy doublet, which exhibits the lowest intensities, may be attributed to W which is directly interacting with the support surface, termed "interfacial W". The remaining doublet, representing the majority of W atoms, is attributed to W not subject to an interaction with the support, termed "bulk W". Notably, interaction of HPW with the support does not produce visible changes in the characteristic signals of other elements: the positions of the Si 2p and O 1s signals do not vary significantly with loading. The positions of signals are also insensitive to the use of different silica supports, though the relative intensities of the component doublets are markedly affected.

The energy of interfacial W is approximately 1.4 eV less than the energy of bulk HPW. This relatively large shift is commonly cited as evidence of a strong ionic interaction between the interfacial Keggin anion and the support, arising from protonation of surface silanol groups. Such an interaction is likely localised to the triad of W atoms nearest to the surface, so a monolayer of Keggin units (with 12 W atoms per unit) would be expected to give a bulk W signal with three times the intensity of its interfacial W signal. However, interfacial W is likely more strongly affected by absorption effects than bulk W, particularly if multilayer deposits of HPW are present. Consequently, the observed (bulk W / interfacial W) intensity ratio should be significantly greater than 3.

Fig. 46(a) displays the variation of interfacial W loading in the SBA-15 catalysts. Excepting two anomalies, absolute interfacial loading increases as HPW content rises from 7 to 34 wt.%, but plateaus as more catalyst is added. This trend supports the theory that monolayer deposition of HPW reaches completion near 35 wt.%: beyond this loading, HPW forms additional layers on existing deposits and is therefore unlikely to interact directly with the support. Furthermore, when expressed as a fraction of the total HPW loading (Fig. 47(a)), the interfacial loading exhibits a trend similar to that of the porosity data presented in section 3.4 (Fig. 36, 37, 41 and 42). As total HPW loading increases, the proportion of W in the interfacial environment decreases, but a plateau is observed between 27 and 39 wt.% (EDX loadings), suggesting that monolayer formation is the only significant form of HPW deposition in this region.

The catalysts supported on KIT-6 exhibit similar XPS spectra to the SBA-15 series (Fig. 46(b) and 47(b)). Absolute interfacial loadings increase with HPW content but appear to plateau and even

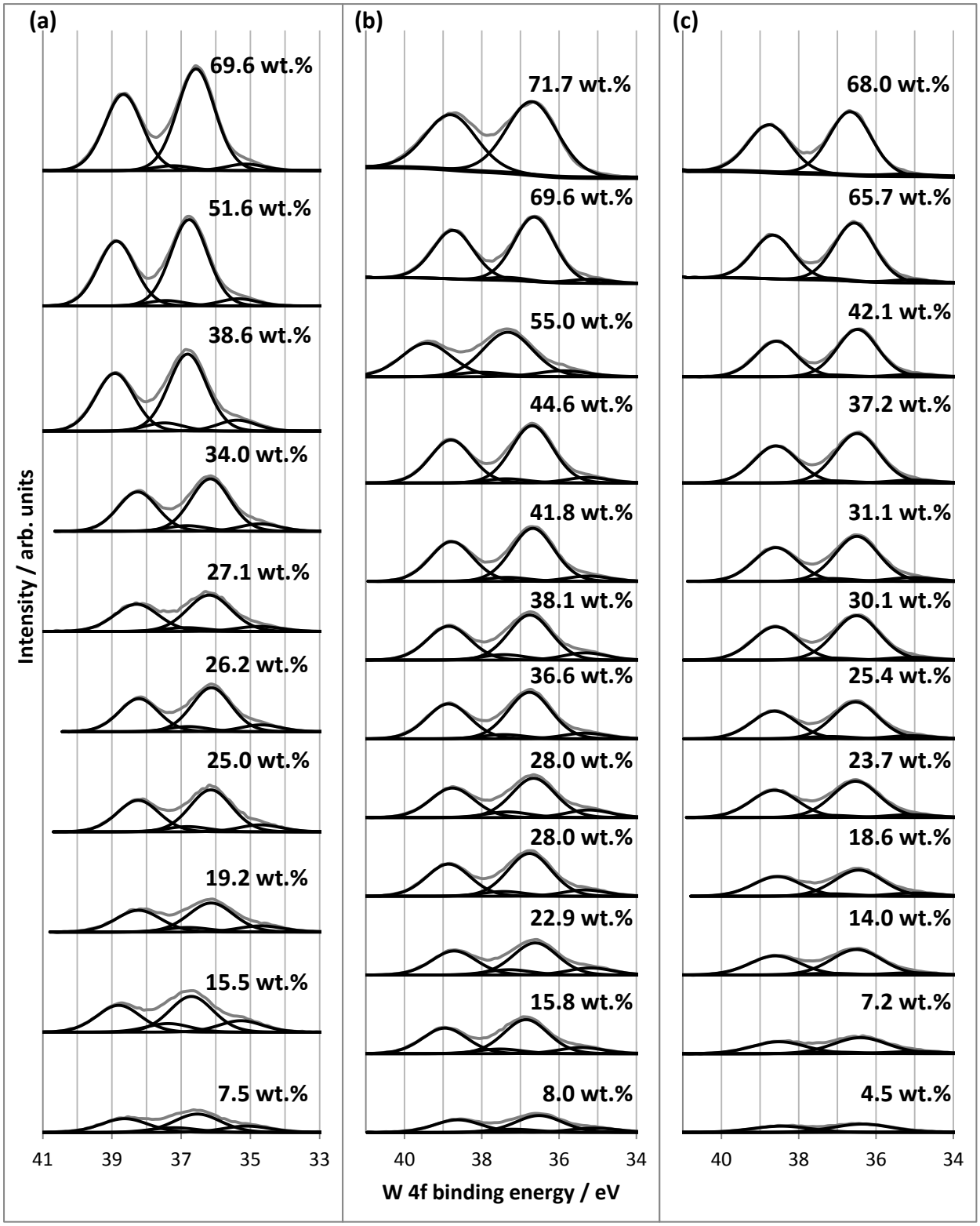

Fig. 45 W 4f signals from HPW on (a) SBA-15, (b) KIT-6 and (c) fumed silica. All signals (plotted in grey) are calibrated against the major C 1s signal of adventitious carbon (285 eV) and fitted to Gaussian-Lorentzian (G-L) doublets of fixed shape and separation (plotted in black). Full-width half-maxima (FWHM) are constrained to be constant for each catalyst. Labelled loadings are average measurements from EDX.

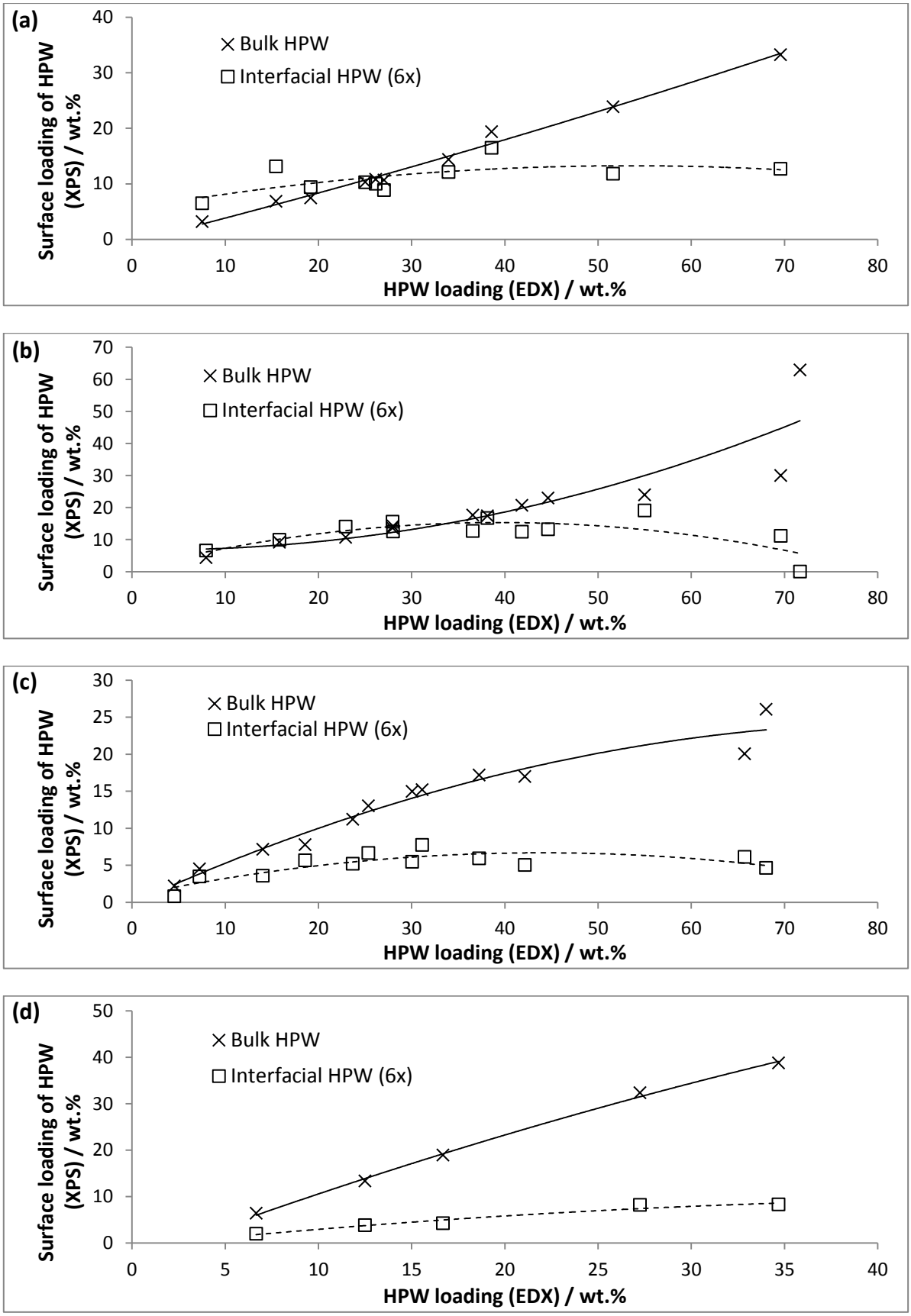

Fig. 46 Bulk and interfacial W loadings of HPW on (a) SBA-15, (b) KIT-6 and (c) fumed silica, and (d) CsPW on SBA-15. Interfacial loadings are scaled by a factor of six for clarity.

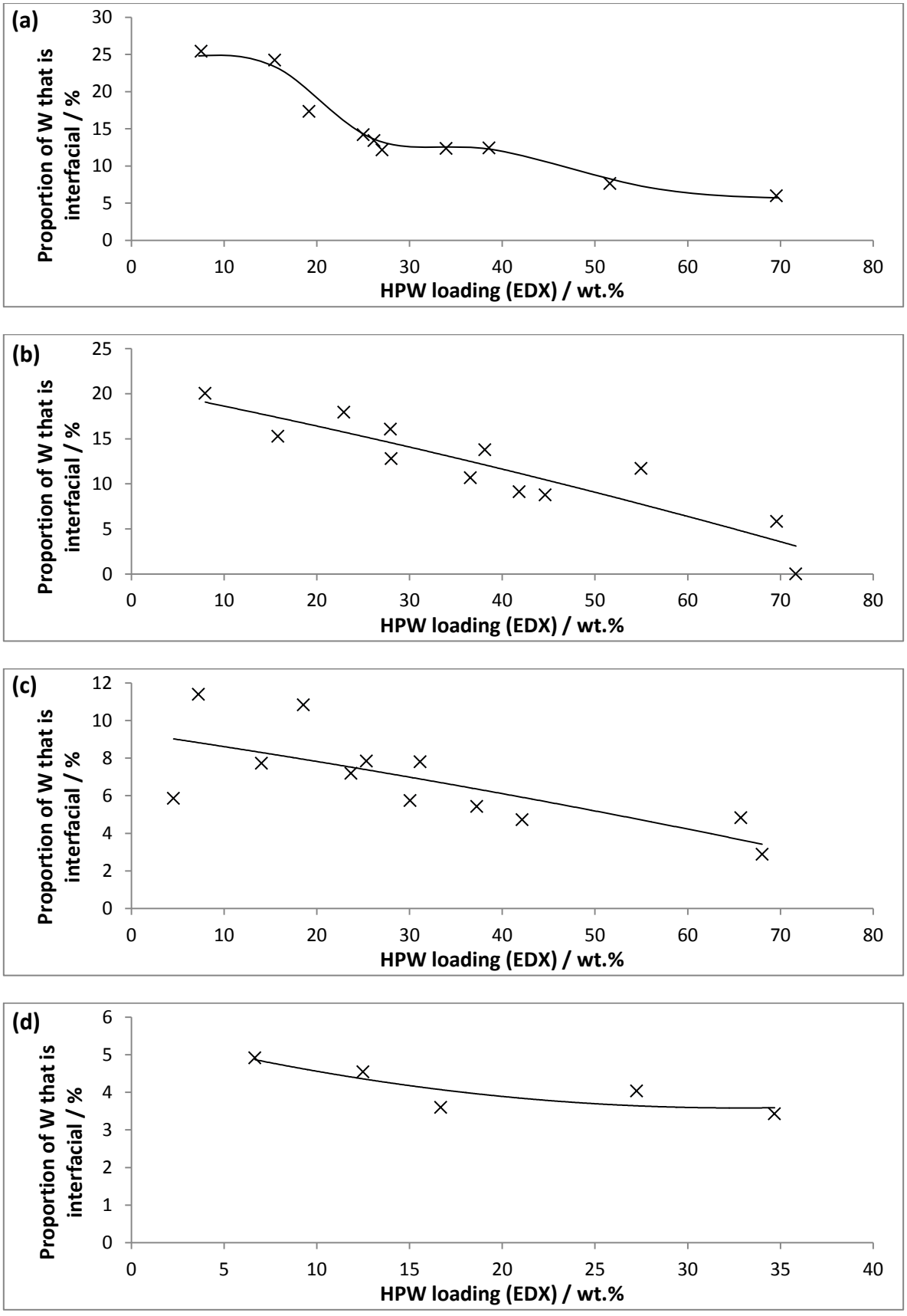

Fig. 47 Proportion of interfacial W in HPW on (a) SBA-15, (b) KIT-6 and (c) fumed silica, and (d) CsPW on SBA-15. Lines are included to guide the eye only.

decrease beyond 40 wt.%. As a fraction of total loading, interfacial HPW loading falls with rising HPW content; however, unlike in the SBA-15 series, the pattern of decrease is continuous, with no pronounced plateaus. This discrepancy is interesting, as it suggests that monolayer growth on KIT-6 is accompanied by some multilayer deposition at all loadings. Such continuous build-up of bulk HPW might partly contribute to the gradual increase in pore blocking displayed in Fig. 42.

Fig. 46 illustrates that, despite small differences in surface area and pore volume, SBA-15 and KIT-6 deliver interfacial HPW loadings within very similar ranges; indeed, the maximum measured interfacial loadings on the supports are identical to two significant figures (2.3 wt.%). The lack of variation between the supports suggests that interfacial deposition is governed primarily by the composition and area of the support surface. By contrast, factors such as pore shape and connectivity exert very little influence on the structure of the HPW deposits.

In the fumed silica catalysts, as in other series, the absolute interfacial loading of HPW reaches a constant value beyond a threshold bulk loading. However, compared with the ordered supports, relatively little HPW is needed to deliver the maximum interfacial loading: the plateau occurs at a bulk loading of just 18 wt.% (Fig. 46(c)). The interfacial loadings are also consistently lower than the corresponding loadings on other supports, and represent a comparatively small proportion of the total HPW content (Fig. 47(c)). These differences are likely due to the lower surface area of the fumed silica support: less HPW is required to match the fractional coverage of other supports, so more of the catalyst must be accommodated in non-interfacial layers on existing deposits.

Intriguingly, interfacial loadings are lower in the supported CsPW catalysts than in all of the HPW catalysts, despite the use of a high-area mesoporous support (Fig. 46(d) and 47(d)). This observation reflects differences in Scherrer particle size: the CsPW particles (8 – 11 nm) are smaller than the HPW particles on fumed silica (12 – 21 nm) but significantly larger than the HPW particles on SBA-15 and KIT-6 (6 – 9 nm). Although low in magnitude, the absolute interfacial loadings nonetheless increase with HPW content and only appear to plateau at the relatively high loading of 27 wt.%. It is evident, therefore, that while CsPW favours bulk precipitation more strongly than HPW, these deposits are still effectively dispersed across the silica surface. The difference in deposition could suggest that nucleation of CsPW occurs less readily (resulting in fewer particles), or that growth and Ostwald ripening processes are more rapid. Another possibility is that CsPW, being less soluble than HPW, is less easily redistributed to maximise interactions with the support. In effect, the kinetic stability of the multilayer deposits may be preventing the formation of a thermodynamically stable monolayer on the silica surface.

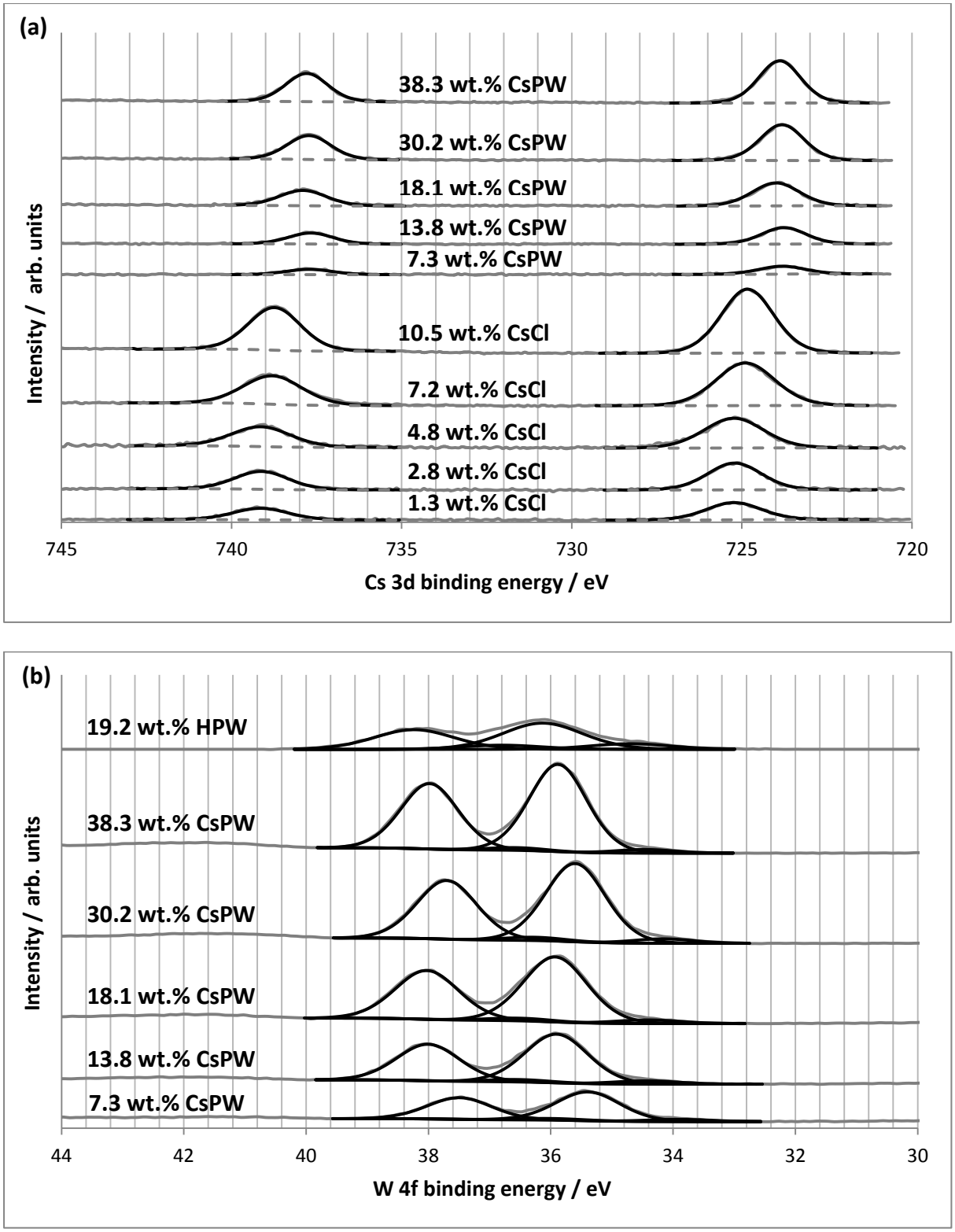

Fig. 48 (a) Cs 3d signals from CsCl and CsPW on SBA-15; (b) W 4f signals from CsPW on SBA-15, compared with a representative HPW catalyst on the same support. All signals (plotted in grey) are calibrated against the major C 1s signal of adventitious carbon (285 eV) and fitted to G-L doublets of fixed shape and separation (plotted in black). FWHM values are made constant for each catalyst. Loadings of supported CsCl are nominal, while those of CsPW and HPW catalysts are the EDX values.

XPS may be used to identify the number of environments that a given element experiences within a material. In the CsPW catalysts, Cs 3d photoelectrons would be expected to produce two separate signals if both CsCl and the HPW salt were present. In practice, supported CsPW produces a signal 1 eV lower than supported CsCl, but only the former was observed in the catalysts produced for this study (Fig. 48(a)). Thus, it may be deduced that excess CsCl is efficiently removed during catalyst formation. The CsPW signal can be fitted as a single doublet of Gaussian-Lorentzian curves, indicating that Cs^+ ions, unlike the W atoms of the Keggin units, do not significantly interact with the support. Interestingly, incorporation of Cs^+ ions has little effect on the positions of the W 4f signals (Fig. 48(b)). This might suggest that Keggin anions interact only weakly with the Cs^+ ions, but it is also possible that ion exchange leads to the formation of a Cs-rich phase with an overlying layer of pure HPW: in this model, signals from the HPW layer would dominate the W 4f spectrum, owing to its proximity to the surface and relatively low concentration of highly absorbing, electron-dense atoms.

It is worth highlighting that any conclusions drawn from XPS data are tentative, since the effects of absorption and sample heterogeneity on signal positions and intensities are not accurately known. Furthermore, although the precision of individual measurements may be estimated by varying the curve fitting parameters between reasonable limits, determining the net variance in elemental composition would require a number of samples of each catalyst to be analysed.

3.6 Surface chemistry of catalysts and supports

High dispersions of HPW on silica are possible due to strong interactions between the catalyst and support. To maximise the catalyst-support interface, HPW adsorbs to silica as a monolayer, with significant multilayer deposits emerging only at very high loadings. Dispersion of HPW on silica is evident in TEM images of the catalyst; for example, although HPW accounts for 34 wt.% of the material shown in Fig. 49, the pore structure is still clearly visible and indistinguishable from the pure support.

As described in section 1.2, binding of HPW to silica can be attributed to an electrostatic attraction between Keggin anions and surface silanol groups, which may be protonated by the acid catalyst. The density of silanol groups on a silica surface can be investigated by thermogravimetric analysis (TGA).[108] A pre-weighed sample is heated to 120^{o}C under an inert atmosphere to remove absorbed water. Subsequently, the temperature is raised to 1000^{o}C and any further mass loss recorded (Fig. 50). Mass lost during the second heating stage may be attributed to water generated by condensation of adjacent silanol groups. By converting the mass decrease to molar quantities, multiplying by two (to account for the stoichiometry of silanol condensation) and dividing by the

area of the support (measured by porosimetry), the surface concentration of silanol groups can be estimated.

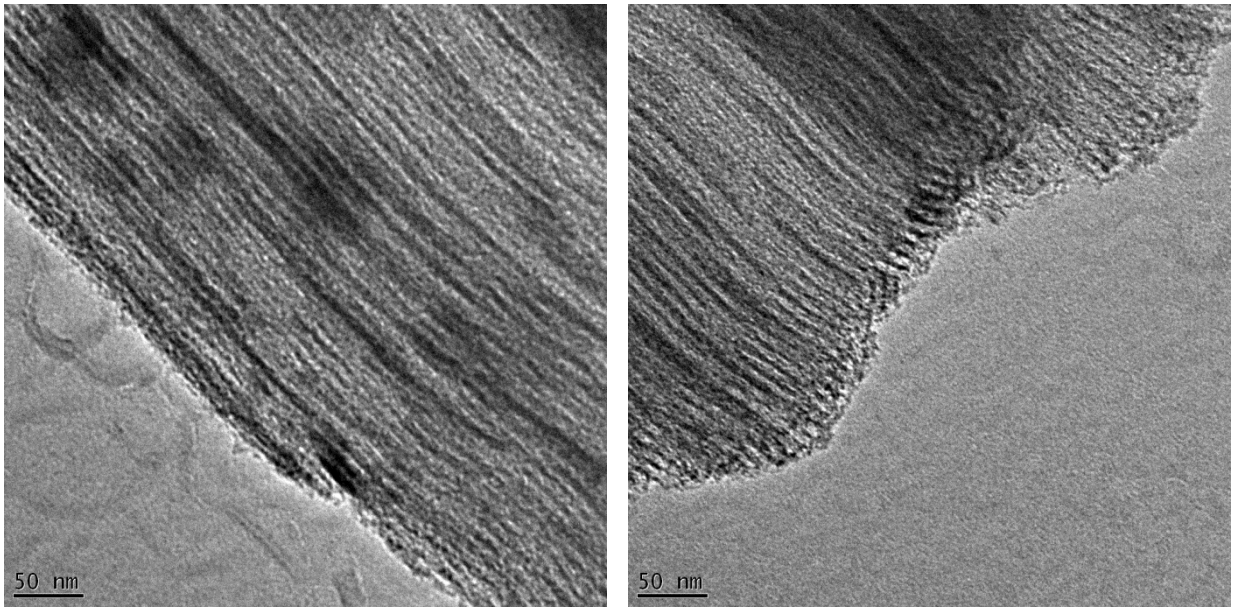

Fig. 49 Transmission electron microscope (TEM) images of 34 wt.% (estimated from EDX) HPW on SBA-15. The uniform channels of the support are clearly visible.

In this study, the surface silanol densities of SBA-15 and KIT-6 were measured as 3.3 and 4.3 nm^{-2} (7.1 and 8.2 mmol water per gram of catalyst) respectively. Other batches of SBA-15 prepared within the research group exhibited comparable densities of 3.8 and 5.3 nm^{-2} (6.4 and 7.9 mmol water per gram of catalyst). Errors in these values are likely substantial, owing to the small masses used in TGA, the errors associated with measured (BET) surface areas, and arbitrary delineation between adsorbed and silanol-derived water; given conservative estimates of 10% error in each measured variable, errors ranging from ± 0.5 nm^{-2} to ± 1.0 nm^{-2} would be expected. Nonetheless, that the values measured are similar (within error) to each other and to comparable data in the literature[108, 109] supports the hypothesis that the surface chemistries of the mesoporous supports are unaffected by differences in pore structure. Indeed, it has been proposed that the silanol densities of such supports are primarily determined by the calcination procedures used in their preparation: higher temperatures favour increased dehydration, so reduce the number of silanol groups on the surface.[108] The presence of silanol groups may be important for catalytic activity, as they provide a binding site for HPW and also enhance the hydrophilicity of the surface. In the esterification reactions employed in biodiesel synthesis, a support with fewer silanol groups might be favoured, to reduce the local concentration of water and prevent hydrolysis of the ester product.

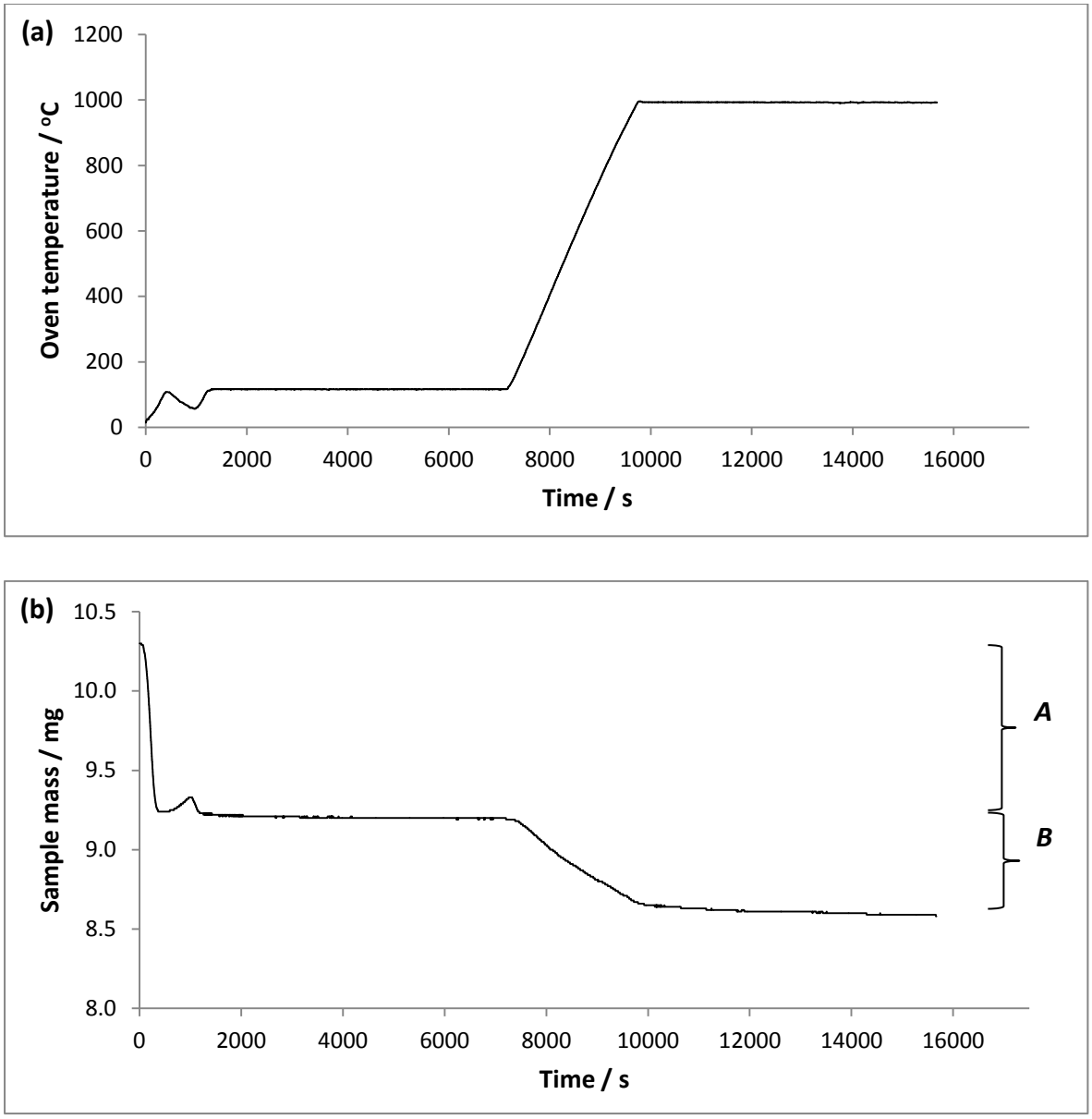

Fig. 50 (a) Temperature ramp and (b) thermogram of SBA-15 during a TGA experiment. In the thermogram, interval *A* represents adsorbed water removed during the initial drying step, while interval *B* is assumed to correspond to water produced through silanol condensation.

TGA analysis of the fumed silica support was attempted, but the low density and surface area of the material prevented accurate measurement of mass losses. As an alternative method of comparison, the silica supports were studied by inverse gas chromatography (IGC).[110-113] This little-known technique resembles a standard gas chromatography experiment, in that a vapour is passed through a solid column and the retention time measured. However, the static phase in IGC is a silanised glass cylinder containing the solid sample to be analysed (typically a powder, but potentially other materials such as fibres and large particles) and the mobile phase is a pure gas such as a volatile alcohol or alkane (Fig. 51).

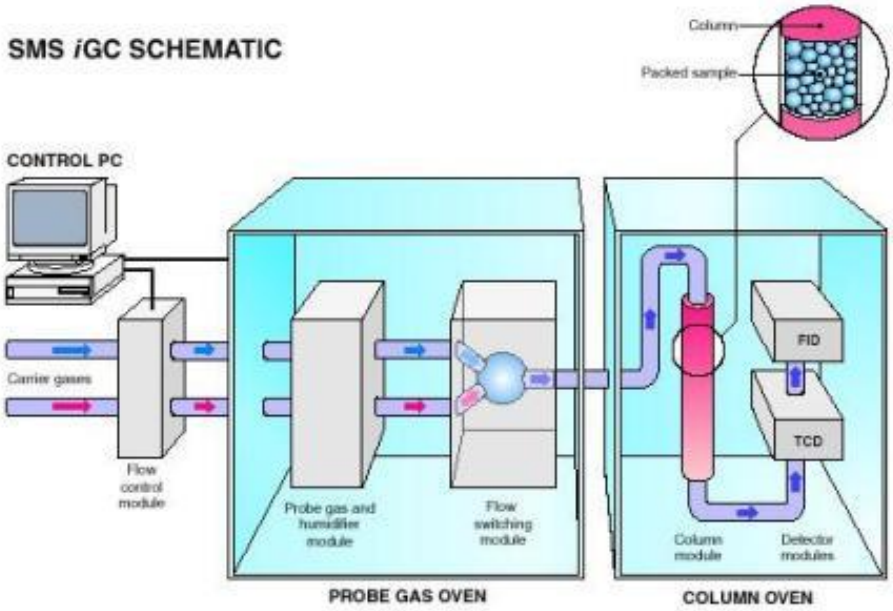

Fig. 51 Schematic representation of the inverse gas chromatograph (IGC) used in this study.[111] A probe compound is dispersed at low concentration in a carrier gas (helium) and passed through a silanised glass column packed with the material of interest. Emergence of the probe from the column is detected by a flame ionisation detector (FID) or thermal conductivity detector (TCD). The desorption profile and retention time of the probe can then be used to quantify the binding properties of the sample surface.

In a standard IGC experiment, the sample is packed into the glass column between plugs of glass wool and inserted into an oven between the liquids to be vaporised (in a separate oven) and the detectors (typically flame ionisation and/or thermal conductivity detectors). The glass column and wool are pre-silanised to minimise interaction with the mobile phase, such that any changes in retention time can be attributed to the material of interest. The column is heated to remove adsorbed species from the sample, then successively treated with different vapours dispersed in a controlled flow of inert gas (typically helium). The retention time of each vapour, termed the probe, is measured from the detector response and corrected by subtracting the retention time of a non-interacting species (methane).

The usefulness of IGC stems from the fact that the retention time, t_R, can be converted to a Gibbs free energy, ΔG, via the equation:[110]

$$\Delta G = RT \ln\left(\frac{jFTt_R}{273.15m}\right) \qquad \text{(Eq. 19)}$$

where R is the molar gas constant, T is the temperature, F is the flow rate, m is the sample mass and j is the James-Martin compressibility correction factor, related to the outlet pressure P_0 and inlet pressure P_i:

$$j = \frac{3}{2}\left[\frac{\left(\frac{P_i}{P_0}\right)^2 - 1}{\left(\frac{P_i}{P_0}\right)^3 - 1}\right] \quad \text{(Eq. 20)}$$

Further, the Gibbs free energy is related to the energy of adhesion, W_A, via Avogadro's constant, N_A, and the molecular cross-section of the probe, a:

$$\Delta G = N_A a W_A \quad \text{(Eq. 21)}$$

Finally, for a probe interacting only via dispersive forces, W_A can be expressed in terms of the known surface tension of the probe, γ_L^D, and the unknown surface tension of the specimen, γ_S^D:

$$W_A = 2\sqrt{\gamma_L^D \gamma_S^D} \quad \text{(Eq. 22)}$$

Overall:

$$\Delta G = 2N_A a\sqrt{\gamma_L^D \gamma_S^D} \quad \text{(Eq. 23)}$$

Crucially, if ΔG is measured for n-alkanes of different lengths and plotted against $2N_A a\sqrt{\gamma_L^D}$, a straight line is obtained (Fig. 52). The gradient of this line is equal to the square root of γ_S^D; thus, from this relatively simple experiment, the dispersive surface tension of the support (independent of probe) can be estimated. Furthermore, given the nature of the calculation, it is not necessary to accurately measure any of the constant terms in the argument of the logarithm of Eq. 19, such as *j*, *m* and *F*: these terms represent a constant additive term in ΔG, so do not affect the gradient of the experimental plot.

The surface tension term γ_S^D represents the dispersive component of the support interaction. To probe non-dispersive, or specific, interactions, the sample must be treated with polar probes. As above, the ΔG value of a polar probe may be calculated from its retention time and plotted against the parameter $2N_A a\sqrt{\gamma_L^D}$, representing the known characteristics of the molecule. However, since ΔG now contains a specific contribution, ΔG_{SP}, it should be vertically displaced from the straight line described by the n-alkane data (Fig. 52). The vertical displacement from the straight line is equal to ΔG_{SP}, while the corresponding y-coordinate on the straight line is equal to the dispersive component of the probe-surface interaction, ΔG_D (Eq. 23).

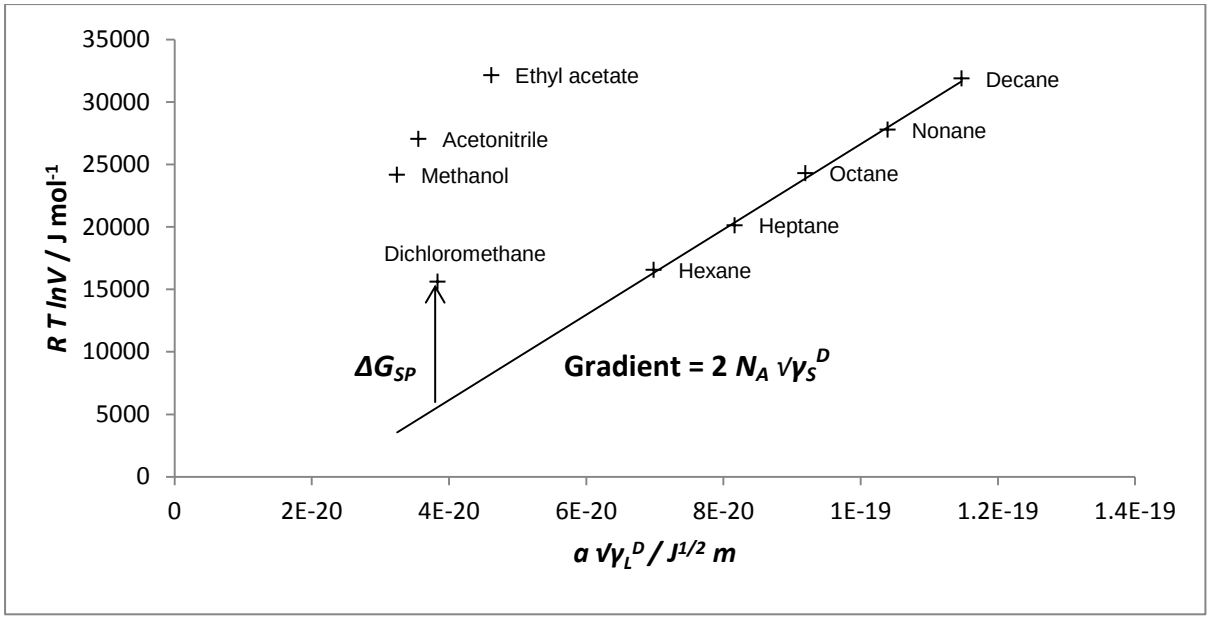

Fig. 52 Surface energy plot for SBA-15 silica, from inverse gas chromatography (IGC) measurements. The plot can be used to calculate the dispersive surface energy of the support, γ_S^D, and the energies of interaction with specific probes. The free-energy contribution of non-dispersive interactions, ΔG_{SP}, is calculated for each probe as the difference between its total interaction energy and the dispersive contribution, ΔG_D, estimated from its molecular area, a; the ΔG_{SP} value for dichloromethane is marked above as an example.

The specific energy ΔG_{SP} may be decomposed into probe and surface contributions as in Eq. 23. Thus, the specific surface tension of the surface, γ_S^{SP}, can be estimated provided the specific surface tension of the probe, γ_L^{SP}, is known. According to Van Oss, γ_S^{SP} can be further split into electron-donor and electron-acceptor contributions, γ_S^- and γ_S^+, by comparison with equivalent values for the probe:

$$\Delta G_{SP} = 2N_A a\sqrt{\gamma_L^{SP}\gamma_S^{SP}} = 2N_A a\left(\sqrt{\gamma_L^+\gamma_S^-} + \sqrt{\gamma_S^+\gamma_L^-}\right) \qquad \text{(Eq. 24)}$$

It is common to apply the Van Oss equation in order to subsequently calculate the Chen-Qi (CQ) ratio, γ_S^D/γ_S^-, a measure of hydrophobicity.[114] The CQ ratio is a useful descriptor of a material, as it changes only if dispersive and specific surface energies are scaled by different factors: a uniform increase in binding strength has no effect. Unfortunately, Eq. 24 can only be applied if γ_L^- and γ_L^+ (and, indeed, γ_L^{SP}) are accurately known. This is true for only a small number of probes. Indeed, it is typical for two probes to be used, with each assumed to be either a perfect electron donor ($\gamma_L^+ = 0$) or a perfect electron acceptor ($\gamma_L^- = 0$).

In this study, the CQ approach was found to be unsuitable. The electron donor probe, ethyl acetate, produced broad signals with long retention times. To address this problem, the sample mass was reduced and the experimental temperature maximised. However, under these conditions, the retention time of the acceptor probe, dichloromethane, was unsatisfactorily short. The errors in both measurements were deemed unacceptable, as repeat CQ experiments failed to deliver convergent results.

As an alternative to the CQ ratio, a probe-specific measure of hydrophobicity was obtained by dividing ΔG_D by ΔG_{SP}. This quantity was calculated for three different probes: ethyl acetate, acetonitrile and methanol. It was expected that comparing $(\Delta G_D / \Delta G_{SP})$ values for these probes would allow chemical differences between the silica supports to be qualitatively identified. For example, variation in the ratio describing the ethyl acetate interaction might suggest a difference in electron-accepting ability, since ethyl acetate is primarily an electron donor.

The measured surface energies of the SBA-15, KIT-6 and fumed silica supports in this study are given in Table 2. The values of γ_S^D and ΔG_{SP} for the ordered mesoporous silicas, SBA-15 and KIT-6, are very similar. This suggests that the supports differ only in their porous characteristics, in agreement with the evidence from TGA. In contrast, fumed silica displays much lower values of γ_S^D and ΔG_{SP}. This relatively weak binding may indicate that the area of contact with probe molecules is smaller, perhaps due to a comparative lack of micropores or surface corrugation. Differences in binding strength could account for differences in HPW particle size on the tested silica supports: on fumed silica, HPW tends to form larger particles than on SBA-15 and KIT-6, as the enthalpic gain from catalyst-support interactions is smaller.

		SBA-15	KIT-6	Fumed silica
Dispersive surface energy, γ_S^D / mJ m^{-2}		71	75	32
Methanol	**ΔG_{SP} / kJ mol^{-1}**	19	21	12
	$\Delta G_D / \Delta G_{SP}$	0.54	0.52	0.58
Acetonitrile	**ΔG_{SP} / kJ mol^{-1}**	21	23	13
	$\Delta G_D / \Delta G_{SP}$	0.54	0.52	0.61
Ethyl acetate	**ΔG_{SP} / kJ mol^{-1}**	22	25	13
	$\Delta G_D / \Delta G_{SP}$	0.67	0.62	0.77

Table 2 Surface energies and hydrophobicity parameters of the silica supports in this study.

While the hydrophobicity factors, $(\Delta G_D / \Delta G_{SP})$, are highest for fumed silica and lowest for KIT-6, the differences between the supports are small and of similar magnitude. It is not possible to state, from IGC data alone, whether the differences are indicative of significant variation in silanol density. However, since the TGA data suggest that the SBA-15 and KIT-6 surfaces are chemically similar, it may be deduced that the trends illustrated in Table 2 reflect only minor compositional variation between supports.

The surface chemistry of the supported HPW catalysts was investigated by Raman spectroscopy. The spectra display three major signals at 130 – 180, 180 – 280 and 950 – 1050 cm^{-1} (Fig. 53). The two lowest-frequency signals may be attributed primarily to resonances of single W-O bonds, while the highest-frequency signal is due to W=O vibrations.[115, 116] Other tungsten oxide species such as WO_3 (a possible product of HPW decomposition) are not evident, and the major signals do not shift significantly upon changing the support or even adding caesium to the catalyst.[116] Signal intensities, however, increase consistently with loading, and also appear to vary between supports (Fig. 54). For example, the signal intensity at 950 – 1050 cm^{-1}, I_{950}, exhibits similar values for the catalysts on SBA-15 and KIT-6, but is 2 – 5 times lower on fumed silica at any given loading. These differences in signal intensity could be due to variation in the surface area irradiated: the ordered silicas contain larger densities of small pores, so their particles may appear rougher, presenting larger areas to the incident laser beam.

Ratios of the signal intensities also vary with loading (Fig. 55). On all supports, the ratio I_{950}/I_{130} exhibits the most pronounced increase, though the ratios I_{950}/I_{180} and I_{180}/I_{130} also display strong positive correlations. Such trends are predominantly caused by differences in scaling of the intensities themselves: while I_{130} and I_{180} increase roughly linearly with HPW content, the rise in I_{950} conforms to a higher order polynomial. The apparent disproportionate rise in W=O signals may reflect differences in the orientations of the W=O and W-O bonds in HPW deposits. It is worth noting, however, that the fumed silica catalysts exhibit less well-defined intensity trends than the other catalysts, and also that the intensity ratios on all supports appear to level off or even decrease at high loadings. A possible interpretation is that correlated variations in intensity are observed only if particle size and shape remains fairly constant. As the silica reaches full coverage, it presents a less favourable substrate for deposition, so large, irregular crystallites of HPW may form instead of a homogeneous layer on the support. Interestingly, the signal intensities and intensity ratios of CsPW on SBA-15 are also significantly different to the values for HPW on the same support (Fig. 56), but this could reflect the effect of caesium on bond vibrations in addition to particle size differences.

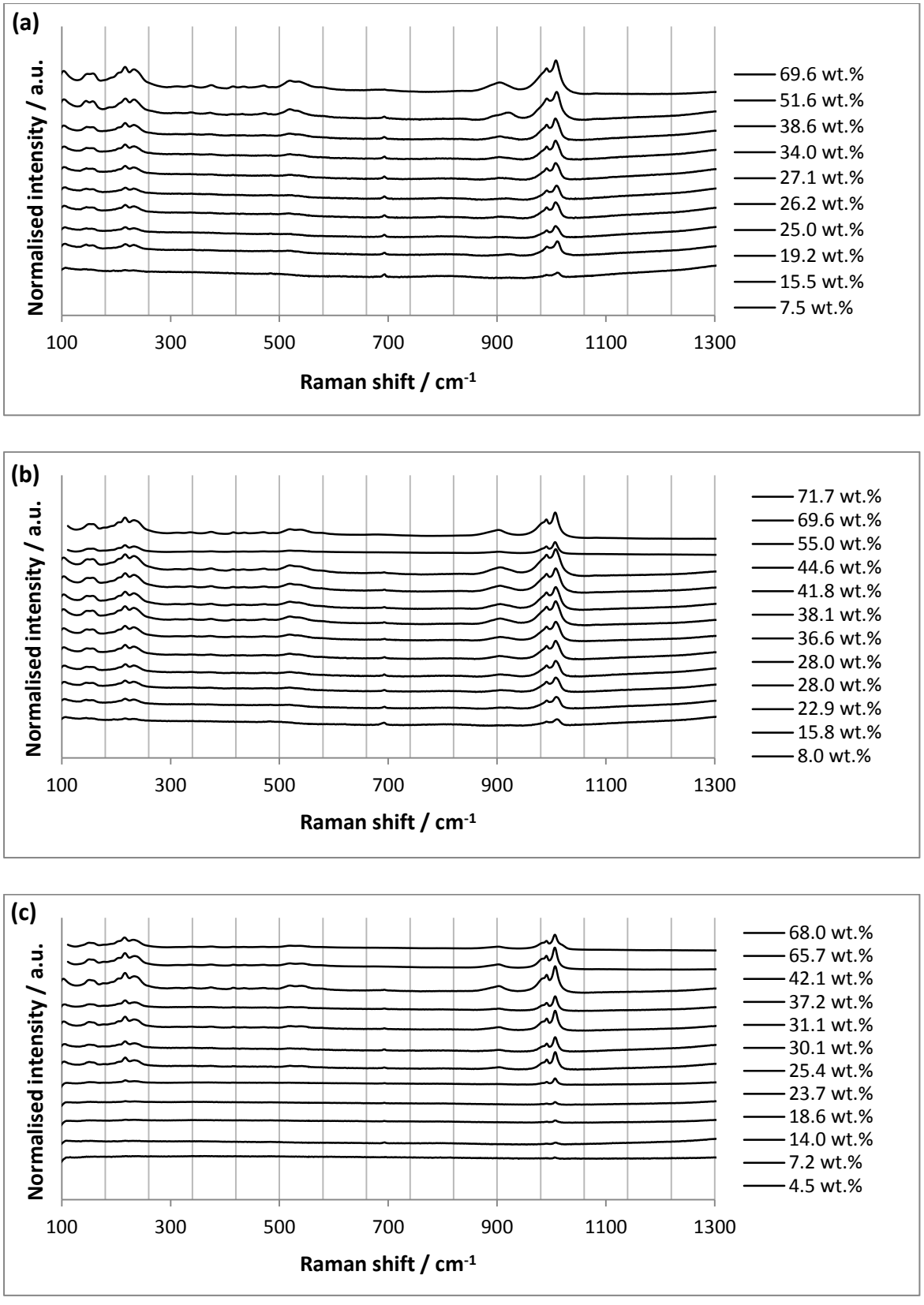

Fig. 53 Raman spectra for HPW on (a) SBA-15, (b) KIT-6 and (c) fumed silica, at a variety of loadings. Intensities were normalised against the intensity at 1300 cm^{-1}, and are plotted on offset log scales for clarity.

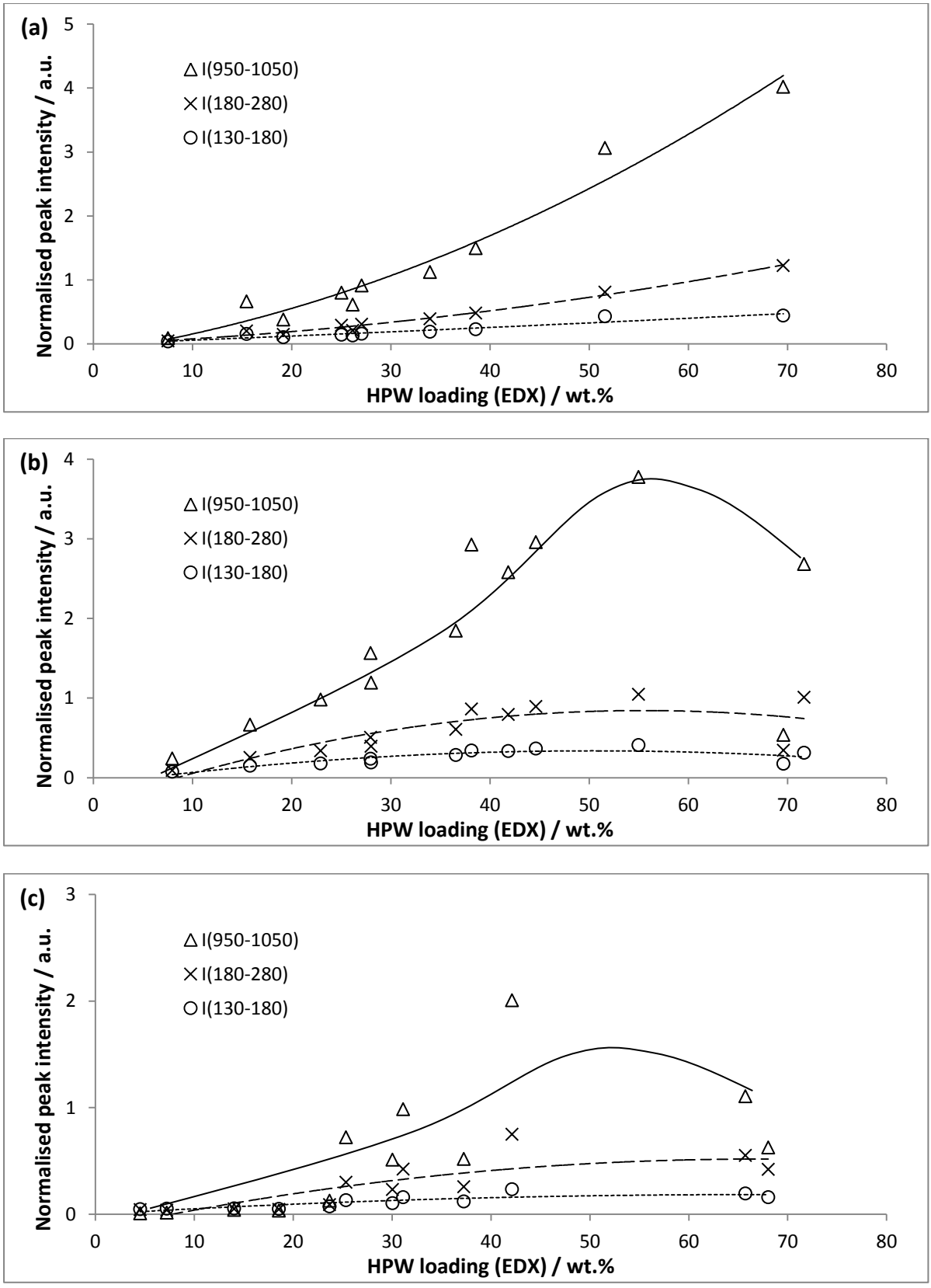

Fig. 54 Intensities of major Raman signals at 130 – 180, 180 – 280 and 950 – 1050 cm^{-1}, corresponding to HPW on (a) SBA-15, (b) KIT-6 and (c) fumed silica. Each peak area was normalised against a linear background over the range of wavenumbers spanned by the peak.

According to literature reports, increasing the loading of HPW on a support may also affect its acidity. For example, Zhang *et al*. found that the number of Brønsted acid sites in a silica-supported Keggin acid (as measured in base-desorption experiments) peaks at a loading of 40 wt.%.[40] However, strong acid sites are not present below 10 wt.% and reach maximum density at a higher loading than weaker acid sites. Thus, the ratio of strong to weak acid sites also increases with loading. A possible interpretation of this data is that weak acid sites correspond to Keggin units in contact with the support, whereas strong acid sites are attributable to the overlying layers. In this model, acid strength increases only once multilayer catalyst deposits begin to form. The number of exposed acid sites, however, is maximised when a full monolayer is generated: increasing the loading further only serves to increase pore blockage and the size of catalyst particles, so reducing the area of acidic material accessible to reactants.

To test the density of acid sites of the HPW catalysts on SBA-15, samples were treated with excess pyridine. Each sample was extensively dried, then analysed by diffuse reflectance infrared spectroscopy (DRIFTS) to determine the relative concentration of base remaining on the surface. Quantification by DRIFTS is difficult, as spectra are strongly influenced by the size, shape and concentration of scattering particles. However, provided the sample particles are small and highly dilute, it may be assumed that the concentration of an absorbing species, *c*, scales with its absorbance, *A*, in accordance with the Beer-Lambert Law:

$$A = \varepsilon l c \qquad \text{(Eq. 25)}$$

The variables *l* and ε denote, respectively, the path length of the cell and absorption coefficient of the sample at the relevant wavelength. To maximise the applicability of the Beer-Lambert Law to this study, catalysts were finely ground and diluted in a weakly absorbing matrix (potassium bromide) prior to pyridine treatment. Absorbance was measured for each prominent signal by integrating the spectral trace above a linear baseline and normalising against the weight loading of catalyst in the sample.

With or without pyridine, DRIFTS spectra for HPW on SBA-15 exhibit a number of prominent resonances between 400 and 1300 cm^{-1}, which are largely attributable to W-O bonds in HPW[20, 117] (Fig. 57(a)). As expected, absorbance in this region increases almost linearly with HPW loading (measured by EDX) except at low loadings (< 20 wt.%), where the signals due to HPW may be comparable in intensity to silica resonances (Fig. 59(a)). Above 1300 cm^{-1}, most major resonances can be assigned to silica or bound water. Specifically, silica produces strong signals at 1790 – 2100 cm^{-1} and 3740 – 3750 cm^{-1}, while water produces a broad signal around 3000 cm^{-1} and sharper resonance at 1560 – 1770 cm^{-1} (Fig. 57(a) and 58(a)). Absorbance due to silica falls linearly with

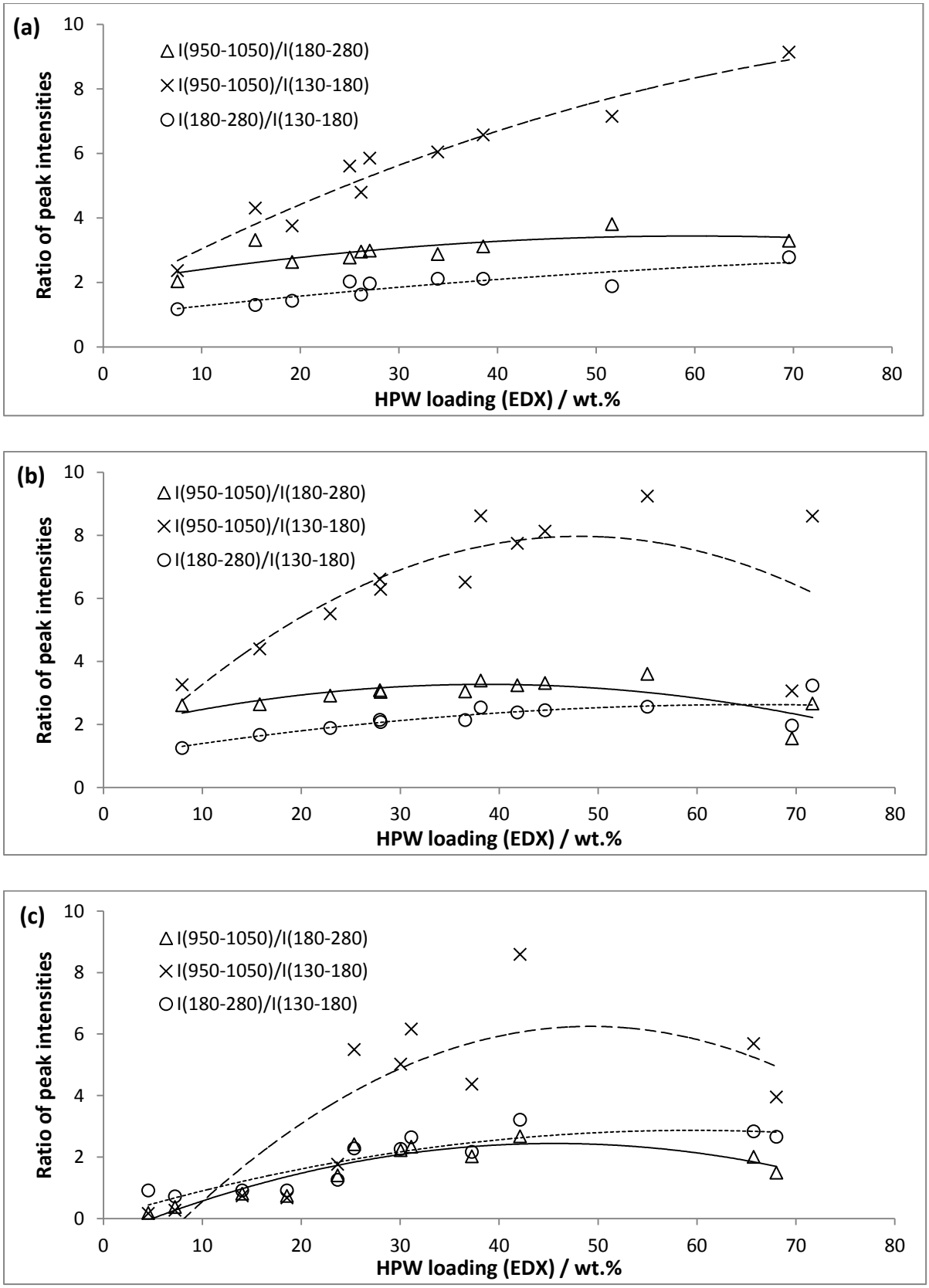

Fig. 55 Ratios of intensities of major Raman signals at 130 – 180, 180 – 280 and 950 – 1050 cm^{-1}, corresponding to HPW on (a) SBA-15, (b) KIT-6 and (c) fumed silica.

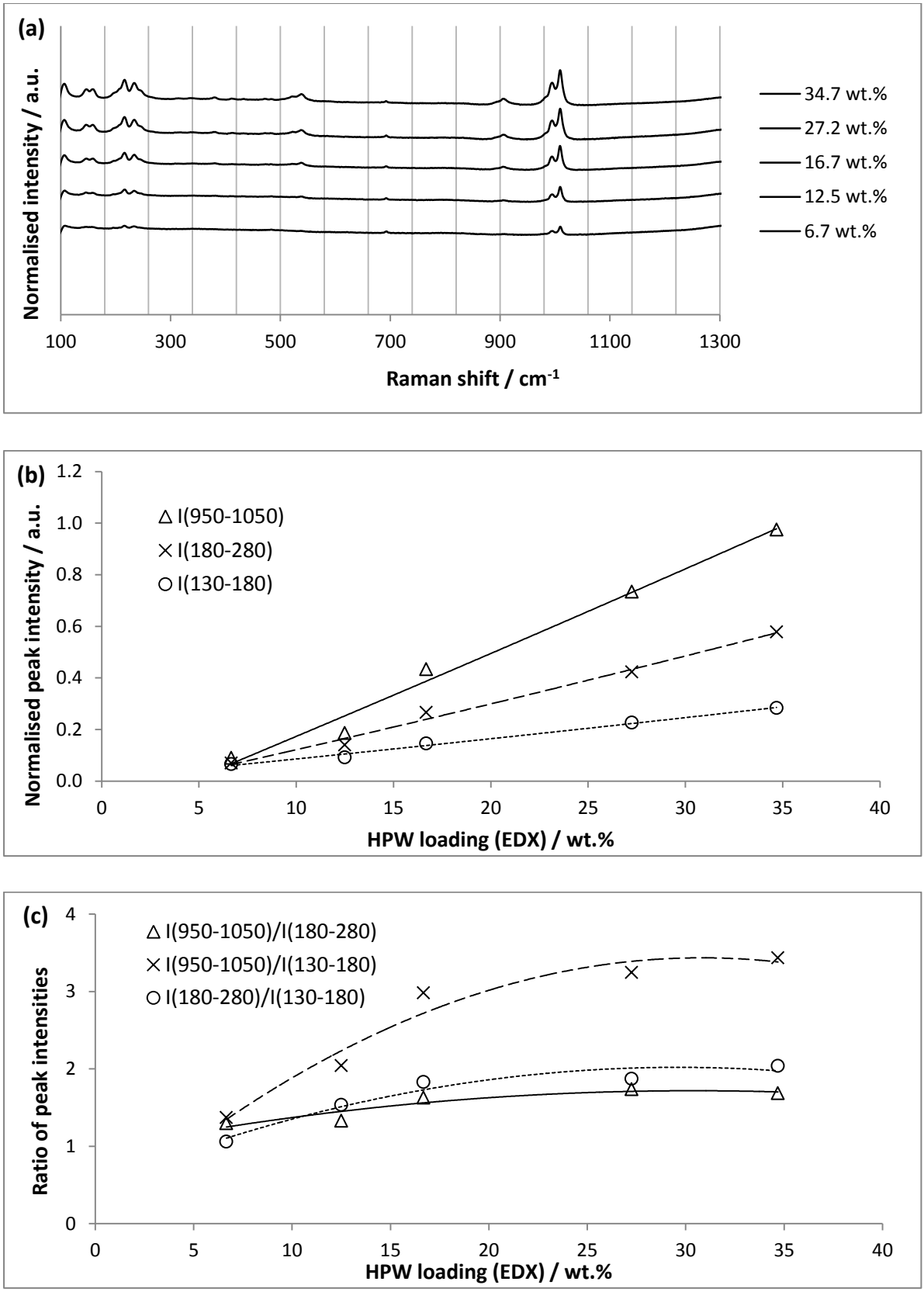

Fig. 56 (a) Raman spectra of CsPW on SBA-15, and (b) Intensities and (c) intensity ratios of major Raman signals at 130 – 180, 180 – 280 and 950 – 1050 cm^{-1}. Each peak area was normalised against a linear background over the range of wavenumbers spanned by the peak.

HPW loading, but the water signals exhibit no such correlation, perhaps reflecting the variability of oxygen loading evident in XPS spectra of these materials.

After addition of pyridine to the samples, new signals are observed in the "fingerprint" region at the expected positions[118] (Fig. 57(b)). Characteristic C-H stretching vibrations are also evident at 2940 – 3000 cm^{-1} (Fig. 58(b)), but the total absorbance of these signals is roughly constant with respect to HPW loading (Fig. 59(b)). It may be inferred that the pyridine content of the samples does not vary with catalyst loading. This lack of variation may be due to the fact that both the catalyst and the potassium bromide matrix were treated with an excess of the base: even after drying, far more pyridine remains adsorbed to the potassium bromide than the diluted catalyst, so the effect of changing HPW content cannot be detected.

Given that the potassium bromide matrix retains a "reservoir" of pyridine, it may be assumed that accessible acid sites in the samples – to which pyridine should bind strongly – are completely saturated. Reaction of pyridine with an acid forms a pyridinium ion, generating new resonances at 1480, 1530, 1600 and 1630 cm^{-1} if the acid sites are of Brønsted type, and at 1440 and 1595 cm^{-1} if they are pure Lewis acceptors.[118] In the spectra analysed in this study, signals in the range 1560 – 1770 cm^{-1} cannot be resolved from the O-H bending resonance of water. However, signals at 1480 – 1500 and 1510 – 1560 cm^{-1} and the absence of any other significant absorption in the range 1400 – 1560 cm^{-1} (Fig. 57(b)) strongly suggest that only Brønsted sites are available for pyridine binding.

For the two detectable Brønsted acid signals, absorbance increases linearly with loading (Fig. 59(b)). It may thus be deduced that pyridine reacts with all of the acid sites capable of contributing to DRIFTS spectra, and that external coverage of the support is proportional to loading. Unfortunately, the internal pore surfaces are not addressed by infrared spectroscopy, and pyridine, being a small and polar molecule, may react with more acid sites than would be accessible to non-polar or bulky reagents. Consequently, it is not possible to draw any conclusions from these data regarding the concentrations of reactive acid sites at different HPW loadings. Indeed, of all the techniques described above, only porosimetry can provide a quantitative assessment of catalyst accessibility to assist in the interpretation of activity measurements.

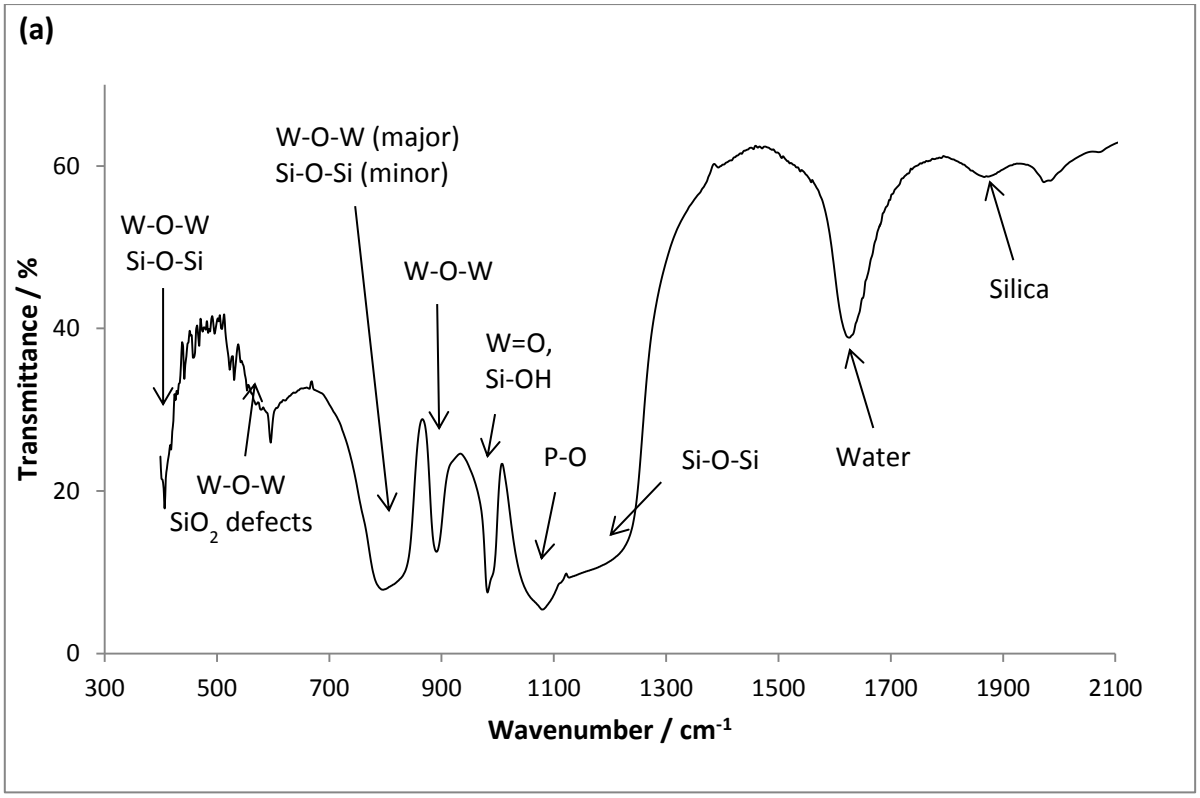

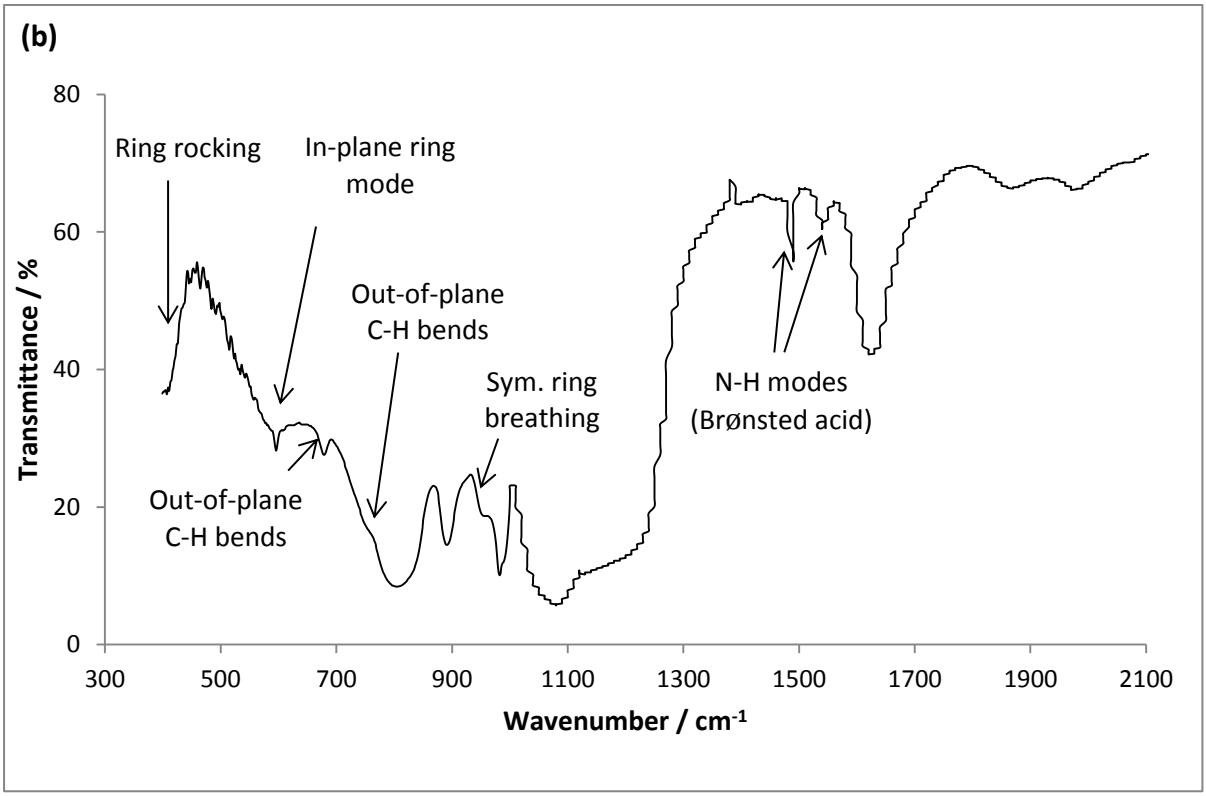

Fig. 57 DRIFTS spectra in the low-wavenumber region of 70 wt.% HPW on SBA-15 (a) without and (b) with added pyridine. Samples were diluted to 5 wt.% in KBr before analysis. Likely assignments for peaks due to silica and HPW are marked in (a), while peaks due to pyridine are assigned in (b).

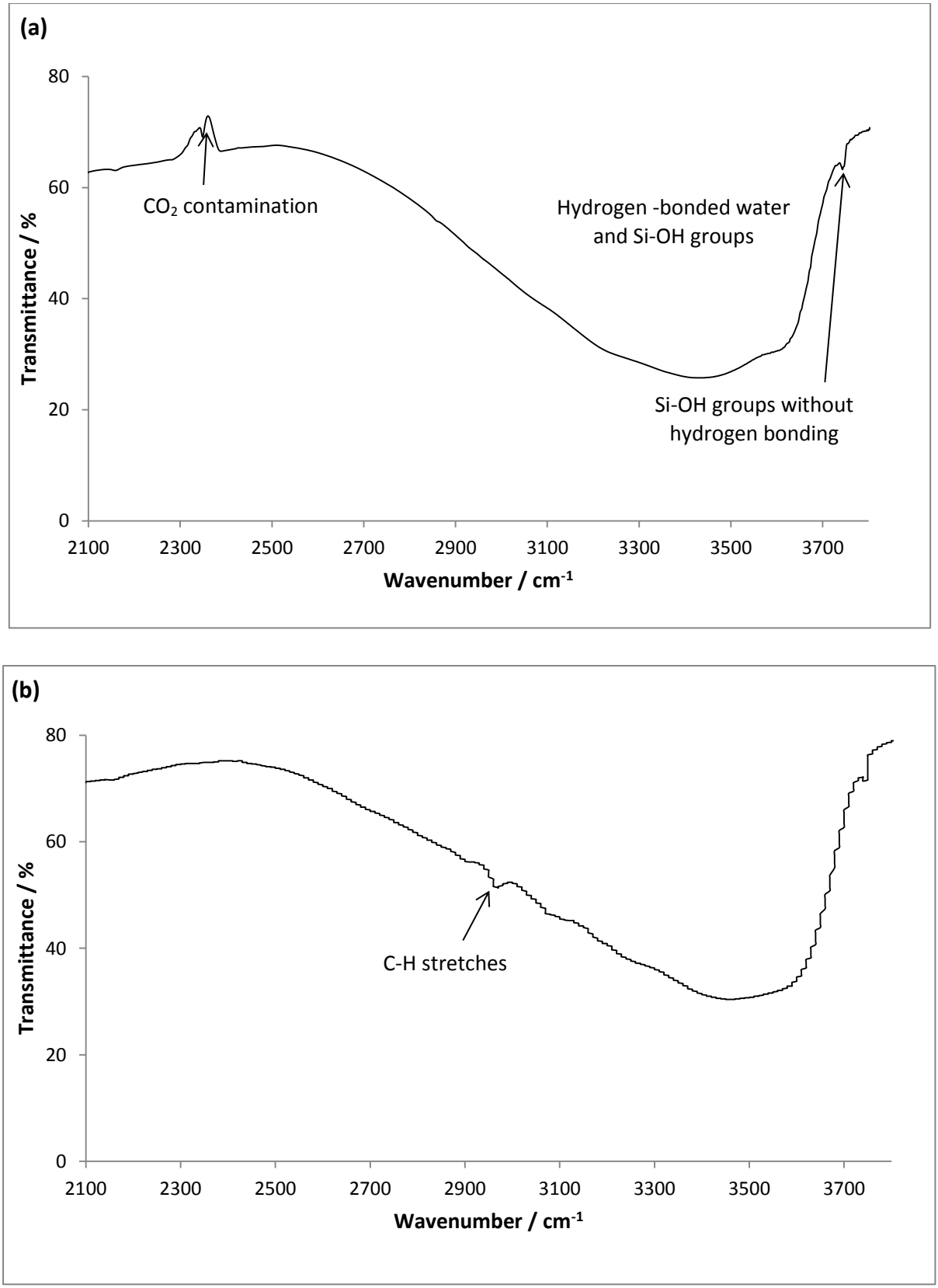

Fig. 58 DRIFTS spectra in the high-wavenumber region of 70 wt.% HPW on SBA-15 (a) without and (b) with added pyridine. Samples were diluted to 5 wt.% in KBr before analysis. Likely assignments for peaks due to silica and HPW are marked in (a), while peaks due to pyridine are assigned in (b).

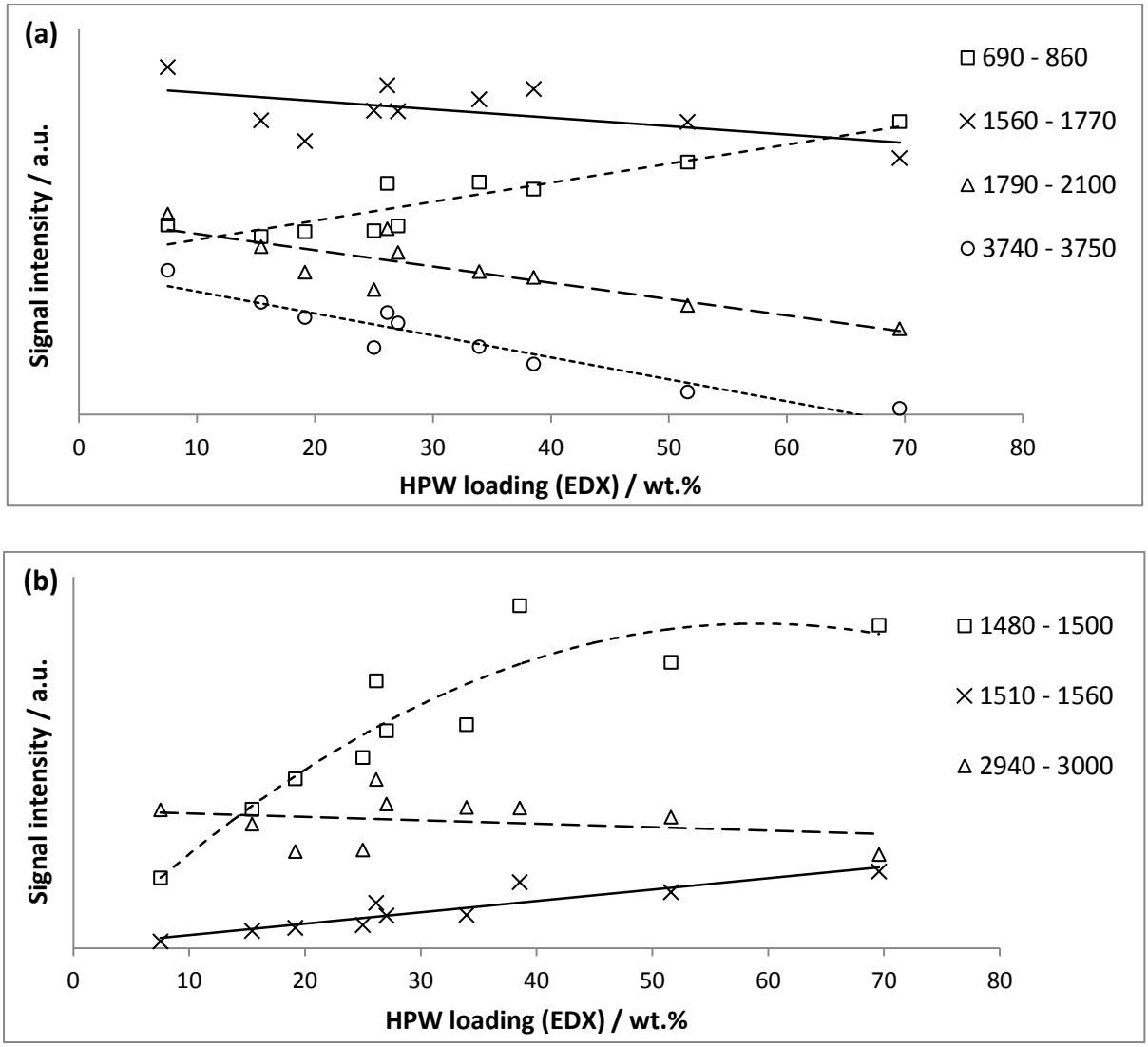

Fig. 59 Intensities of DRIFTS signals from HPW supported on SBA-15, after treatment with pyridine. Signal intensities attributed to HPW and/or silica are displayed in (a), while those attributed to pyridine are displayed in (b). The approximate range of wavenumbers for each signal is listed in the legend. Each peak area was normalised against a linear background over the range of wavenumbers spanned by the peak.

3.7 Interpretation of reaction profiles

For most catalysts studied, reaction profiles for the alpha-pinene isomerisation are approximately linear for at least the first hour (Fig. 60). Such a trend is characteristic of zero-order kinetics, implying the catalyst is saturated and operating at maximum turnover. The rate is equal to the gradient of the profile in this region and may be converted to a turnover frequency (*TOF*) by dividing by the number of moles of HPW in the catalyst sample. *TOF* values and the raw rate constants, k_{raw}, for the HPW catalysts in this study are shown in Fig. 61.

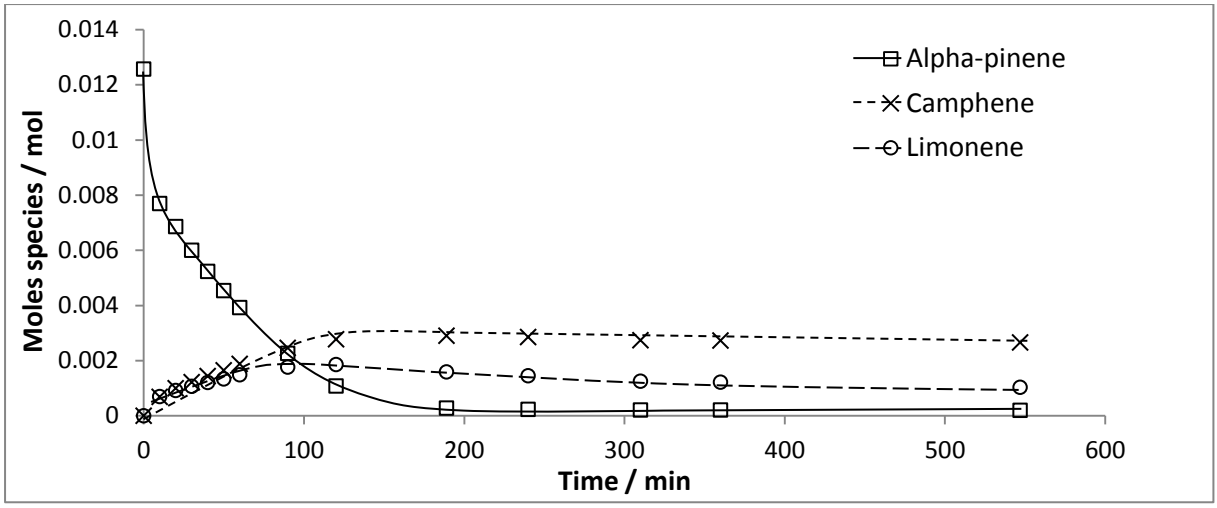

Fig. 60 Reactant and product quantities during alpha-pinene isomerisation at 35°C, catalysed by 19 wt.% HPW on SBA-15.

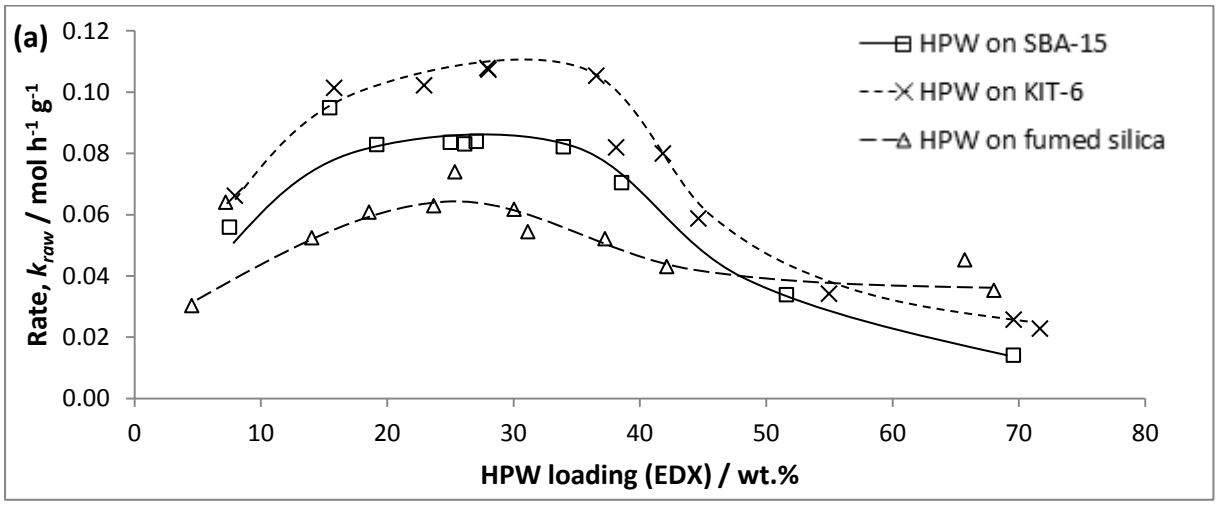

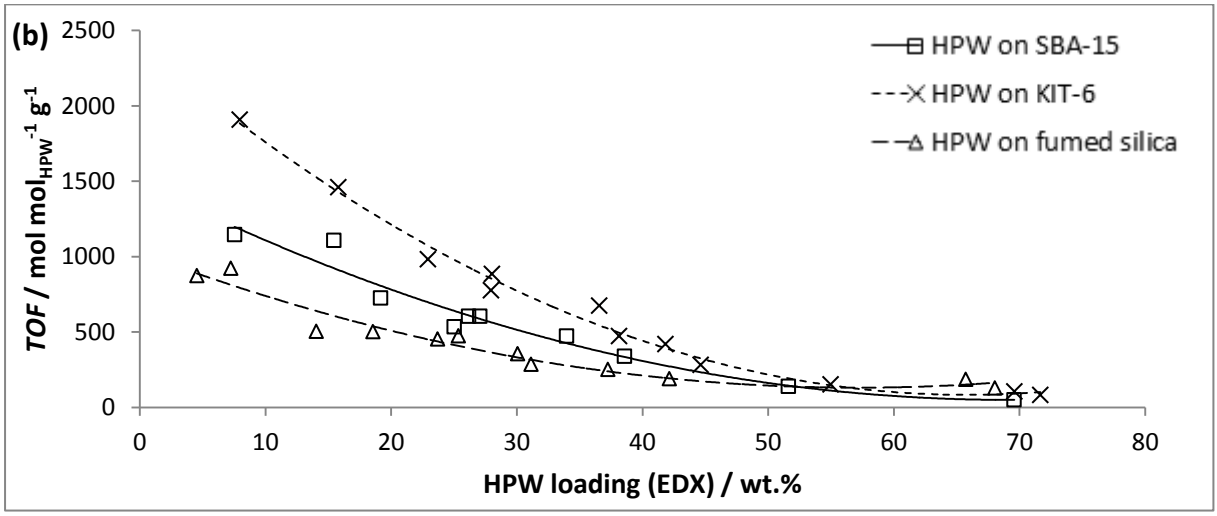

Fig. 61 (a) Rates (k_{raw}) and (b) turnover frequencies (*TOF*) of alpha-pinene isomerisation reactions catalysed by HPW on silica supports.

The isomerisation reactions proceeded with a marked reddening of the initially colourless reaction mixture, in addition to the formation of a small quantity of oily residue. These changes are likely attributable to the formation of oligomers, which may constitute as much as 40% of total alpha-pinene conversion (see later, Fig. 67). It is reasonable to suppose that such by-products might influence the rate of reaction by blocking pores within the supported catalyst, adsorbing to products and reactants in solution, or otherwise affecting the transport of molecules to and from the sites of reaction. Indeed, since the reaction is conducted in neat reagent, even the conversion of alpha-pinene to isomeric terpenes could significantly influence the diffusion rates of reagents. That reaction profiles remain linear in the first hour of reaction, however, suggests that effects of this nature can be neglected as minor or systematic errors in the measurements of k_{raw}. To test this theory, reactions were performed using the same batch of catalyst (27 wt.% HPW on SBA-15) at different stirring rates (Fig. 62). The results indicate that accelerating the mixing of reagents has little effect on k_{raw}: saturation of the catalyst means that the rate of reaction is determined by the turnover frequency at the catalytic sites rather than mass transport considerations.

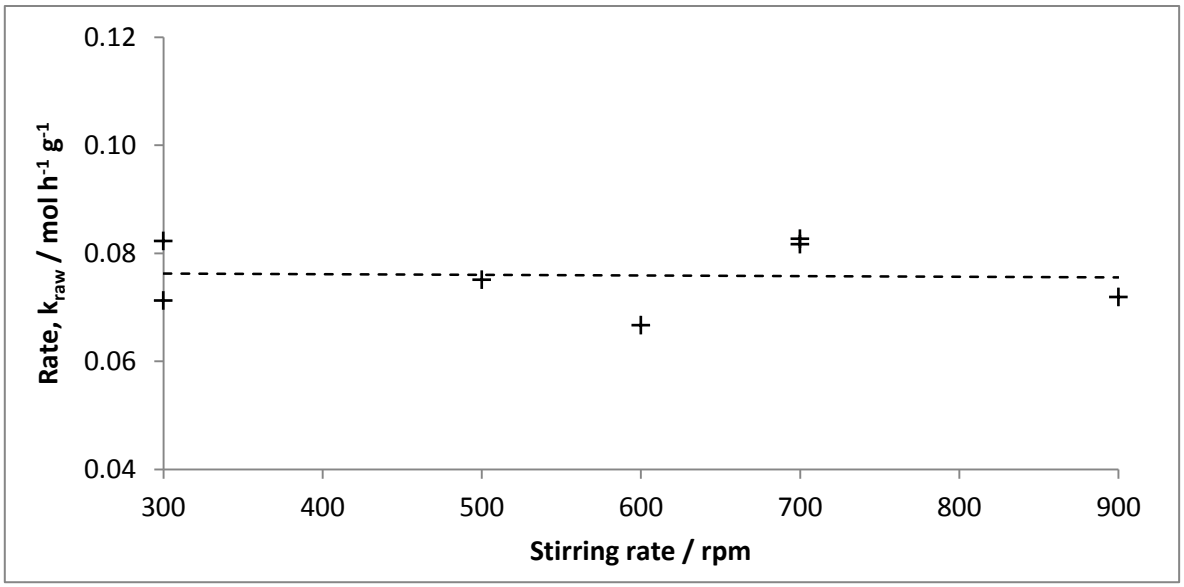

Fig. 62 (a) Rates (k_{raw}) of alpha-pinene isomerisation reactions catalysed by 27 wt.% HPW on SBA-15 at different stirring rates. The near-zero gradient of the line of best fit suggests that there is little deviation from the mean k_{raw} value (0.076 ± 0.003 mol h^{-1} g^{-1}).

There is little difference between HPW catalysts supported on SBA-15 and those supported on KIT-6, especially at loadings greater than 30 wt.%. However, these catalysts exhibit substantially greater activities than catalysts supported on fumed silica. A plausible hypothesis is that fumed silica, possessing a lower area than the other supports, presents proportionally fewer catalytic sites at its

surface when saturated with HPW. To evaluate this theory, rate constants, may be normalised to support mass, in the manner of the *NPV* and *NSA* calculations:

$$k_{mass} = \frac{k_{raw}}{1 - W} \quad \text{(Eq. 26)}$$

In Eq. 26, W is the fractional HPW loading (by mass) from EDX and k_{mass} the normalised rate constant. Using the surface area of the support, S_0, from nitrogen porosimetry, k_{mass} may be converted to k_{area}, the rate constant per area of support:

$$k_{area} = \frac{k_{mass}}{S_0} \quad \text{(Eq. 27)}$$

These normalisation procedures are important, as they allow the effect of additional HPW to be analysed without having to account for the changing ratio of catalyst to support. For example, if every mole of HPW added the same number of catalytic sites to a unit area of support, k_{mass} and k_{area} would increase linearly. By comparison, k_{raw} would scale as the function $W(1-W)$, making it more difficult to detect any meaningful variation in the correlation between HPW content and catalytic activity. It may be argued that a *TOF* calculation (k_{raw}/W) would highlight such variation, since catalyst deposits with equal activity per site should exhibit identical *TOF* values. However, *TOF* values may appear to vary continuously with loading if there is a significant error in W, or if catalyst deposits become equivalent only above a threshold loading. In this study, catalyst deposits in micropores are expected to be almost inactive, since they are highly inaccessible to reagents. Thus, if HPW in mesopores exhibits a constant molar activity, the calculated *TOF* may scale as $(W - a(1-W))/W$, where a is a constant (specifically, the mass of HPW required to fill the micropores in one mass unit of support).

The values of k_{area} and k_{mass} for HPW on SBA-15, KIT-6 and fumed silica are plotted in Fig. 63. The trends in k_{mass} are objectively similar to those in k_{raw}. However, when rate constants are normalised to support area, catalysts on fumed silica appear more active than those on other supports. In all series, the raw and normalised rate constants increase less rapidly as HPW content rises, and reach a peak at an intermediate loading. It may be inferred that there is an effect, not accounted for in the normalisation procedure, which reduces the rate constant as loading increases. A second effect similarly reduces the rate constant as the degree of mesoporosity increases, such that catalysts on fumed silica may prove more effective, per unit area, than either SBA-15 or KIT-6.

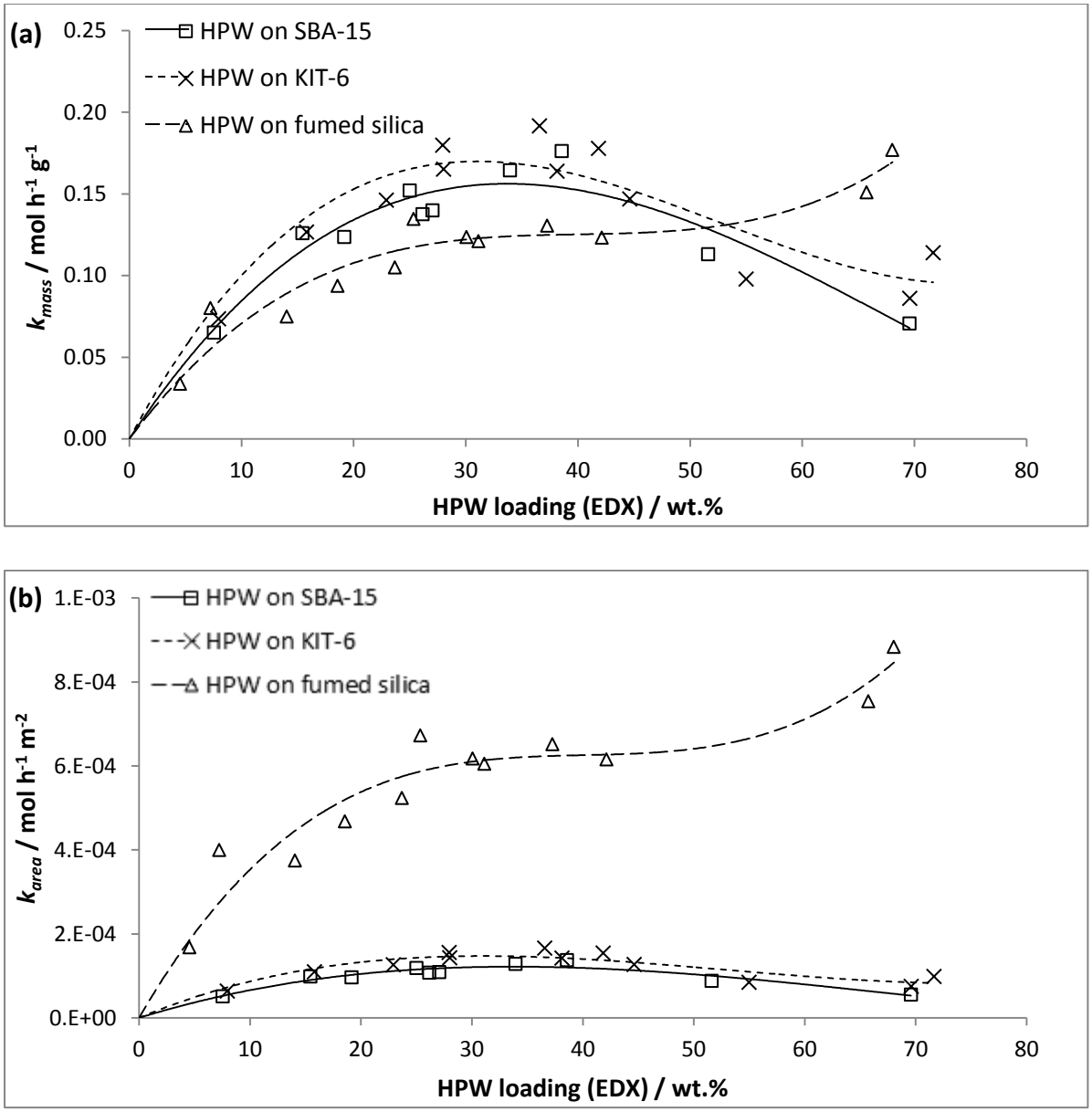

Fig. 63 Rates of alpha-pinene isomerisation reactions catalysed by HPW on silica supports, normalised to (a) support mass and (b) area.

Pore blocking is one possible source of reaction rate variation. Catalytic sites that are not accessible to reactants cannot contribute to the rate, so a *TOF* calculation is likely to underestimate the molar activity of the accessible catalyst. Moreover, since pore blocking increases with loading, *TOF* values are liable to decrease across a series. Evidently, pore blocking provides a qualitative explanation of at least some of the trends in Fig. 63. To quantitatively assess the theory, k_{mass} values may be divided by NPV_{corr}, to provide an estimate of the rate constant per unit of accessible support mass, k_{mass}^{acc}:

$$k_{mass}^{acc} = \frac{k_{mass}}{NPV_{corr}} \quad \text{(Eq. 28)}$$

The caveats discussed in section 3.4 still apply: dividing k_{mass} by NPV_{corr} is valid only under the assumption that pores are uniform in size and shape, such that the fraction of accessible area is roughly equivalent to NPV_{corr}. Nonetheless, k_{mass}^{acc}values for the SBA-15 and KIT-6 catalysts appear to increase linearly with HPW content up to 40 wt.% (Fig. 64). Thus, pore blocking can be deemed the major cause of variation in catalytic activity within these series, at low and intermediate loadings. The corresponding rate constants for the fumed silica catalysts, k_{mass}, already increase linearly below a threshold value, so the approximation NPV_{corr} = 1 may be justified for these materials.

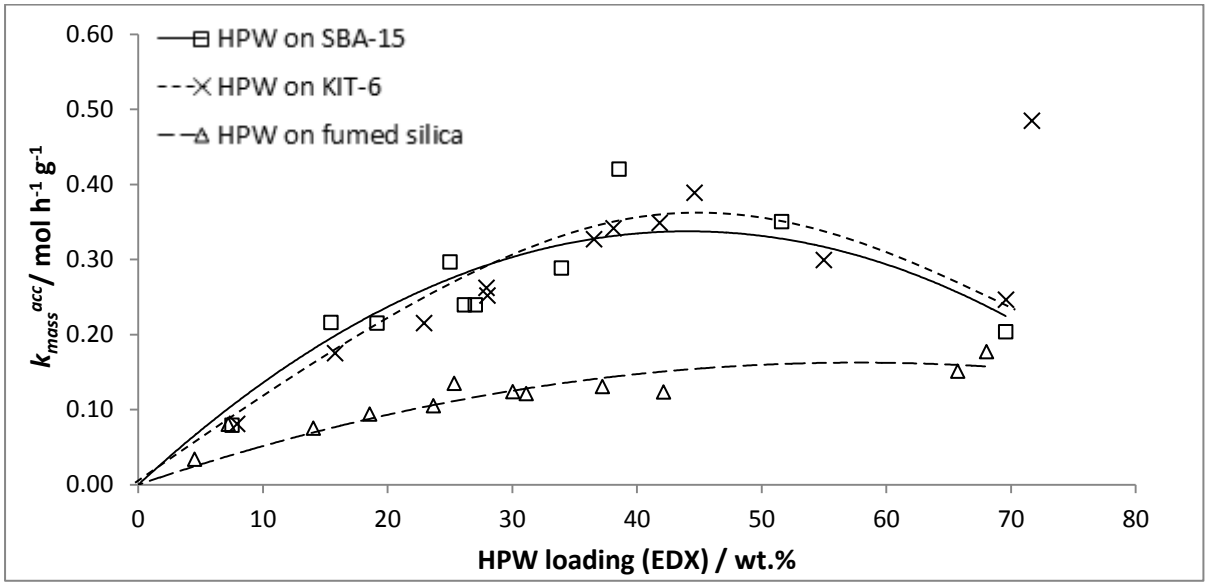

Fig. 64 Rates of alpha-pinene isomerisation reactions catalysed by HPW on silica supports, normalised to support mass and corrected for pore blocking.

Notably, normalising k_{mass} against estimates of pore blocking serves only to enhance the apparent variation between the different supports. Intuitively, this difference may be attributable to variation in surface area. To investigate this possibility, k_{area} values may be adjusted for pore blocking as above:

$$k_{area}^{acc} = \frac{k_{area}}{NPV_{corr}} \quad \text{(Eq. 29)}$$

Remarkably, when k_{area}^{acc} values are plotted against the loading of HPW per area of support (W/S_0), the data for the three supports are almost exactly convergent at loadings below 40 wt.% (Fig. 65). Furthermore, the plots are roughly linear and intercept the origin, suggesting a constant TOF value of 0.6 mol g_{HPW}^{-1} h^{-1} or 1700 mol mol_{HPW} h^{-1} (where the quantity of HPW is that present in accessible

pores only). It may be concluded that, for the supports tested, variation in activity is due primarily to differences in surface area and pore blocking, and can thus be predicted from porosimetry measurements alone. That the sizes of catalytic particles can be neglected, despite apparently varying between supports, provides further evidence that HPW is deposited as a monolayer: increasing Scherrer size reflects growth in the plane of the support surface, so is not indicative of decreasing catalyst accessibility. Differences in the chemistry of the support surface (hydrophobicity etc.) can also be deemed unimportant, since they remain unaccounted for in the k_{area}^{acc} calculation.

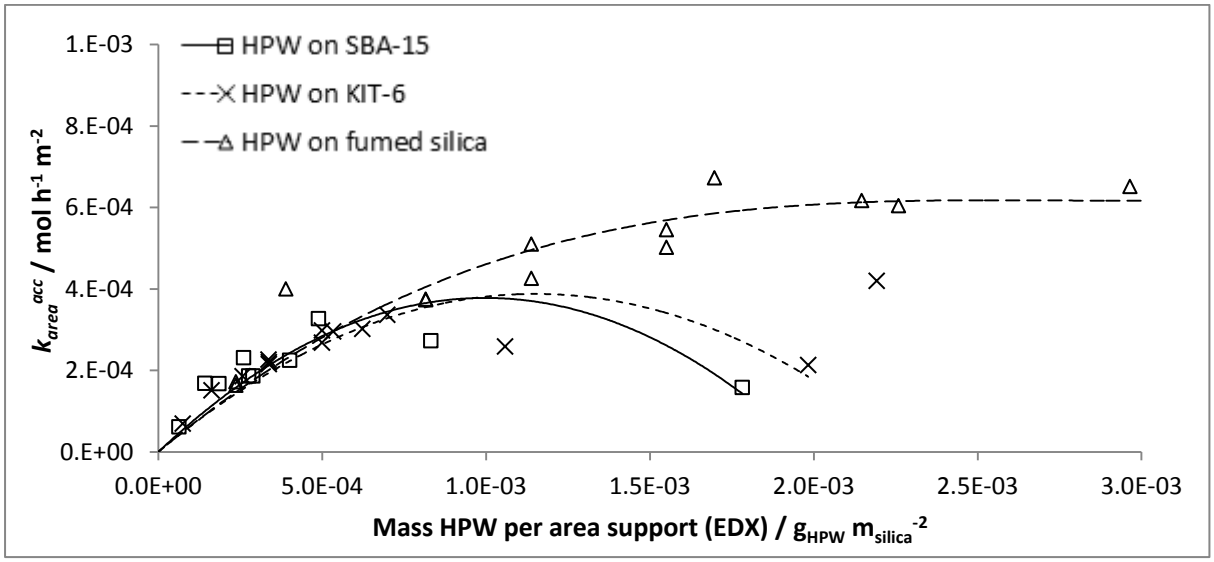

Fig. 65 Rates of alpha-pinene isomerisation reactions catalysed by HPW on silica supports, normalised to support area and corrected for pore blocking.

At high loadings, the profiles for the different catalyst series diverge. For the catalysts on SBA-15 and KIT-6, increases in loading beyond 40 wt.% cause k_{area}^{acc} to decrease sharply. The rate constant for the fumed silica catalysts, meanwhile, tends towards a constant maximum value of 6.5 x 10^{-4} mol h^{-1} m^{-2}. It is likely that reaction rate is limited at high loading due to the difficulty of dispersing additional catalyst on an already saturated support. The size of catalyst particles is forced to increase (as indicated by PXRD measurements), so a smaller proportion of the added catalyst is made accessible to reagents. Adding catalyst may also fuse together support particles and contribute substantially to pore blocking. Different supports may exhibit varying susceptibilities to these effects: for example, SBA-15 and KIT-6 are more liable to exhibit extensive pore blocking, and particle sizes are likely to show greater increases on fumed silica. However, it should be noted that some of the divergence in Fig. 66 could be attributable to errors in k_{area}^{acc}, as neither nor NPV_{corr} nor k_{raw} can be accurately determined if the loading of HPW is high. Errors in *W*, if comparable in size to the normalisation factor (*1-W*), may also be significant.

In addition to providing a measure of the general activity of catalysts, data from alpha-pinene reactions may offer an indication of the strength of acid sites. Since the polycyclic products camphene and beta-pinene are less stable in acid than monocyclic products, a catalyst which is more selective towards the polycyclic species likely contains acid sites which are weaker on average.[38] Fig. 66 displays the selectivities of catalysts on SBA-15 after four and 23 hours of reaction. Though these selectivities do not correlate strongly with loading, it is clear that the two highest HPW loadings deliver substantially more limonene than the other catalysts (at the expense of camphene), tentatively indicating the presence of stronger acid sites. It is further worth noting that for every catalyst, the sum of the selectivities lies in the range 60 – 80% after four hours and 20 – 70% after 23 hours (Fig. 67). Some of the conversion unaccounted for (2 - 7% of total conversion, Fig. 68) may be attributed to unidentified isomerisation products, of which 11 were detected in GC chromatograms. However, most of the discrepancy is likely due to the formation of oligomers, which led to a marked reddening of the reaction mixture during the course of the kinetic trials. Although some high-molecular-weight products were observed in GC traces as broad signals with long retention times, a substantial fraction were removed as a visible residue upon filtration of the reaction mixture aliquots, so the total yield of polymerisation reactions could not be directly measured.

Analysing selectivities after a fixed time may not provide a fair comparison of catalysts, as the results could simply reflect how the make-up of the product mixture varies with changing conversion. It is generally observed, for example, that limonene and camphene react to form other terpene products and oligomeric species upon extended exposure to acid (Fig. 66). Thus, if the concentrations of these minor products are measured after 23 h, the catalysts with the greatest values of k_{raw} (i.e. those with intermediate HPW loadings, Fig. 61 and Fig. 68) are found to deliver the highest yields, even though the corresponding turnover frequencies may be relatively low. An alternative approach is to compare selectivities at a fixed degree of conversion. This method, though less common than the fixed-time approach described above, provides a more reliable indication of acid strength since the results are unaffected by variation in the total reaction rate. In this study, the concentrations of the major products, camphene and limonene, are found to increase in a linear fashion during the first hour of reaction, mirroring the linear consumption of alpha-pinene. Thus, it is possible to calculate the selectivity for each species by simply dividing the rate of its production by the rate of consumption of the reactant. Rates are measured from the gradient of a regression line through multiple data points (typically four to six measurements), so are likely far more accurate than the single-point selectivity estimates usually presented.

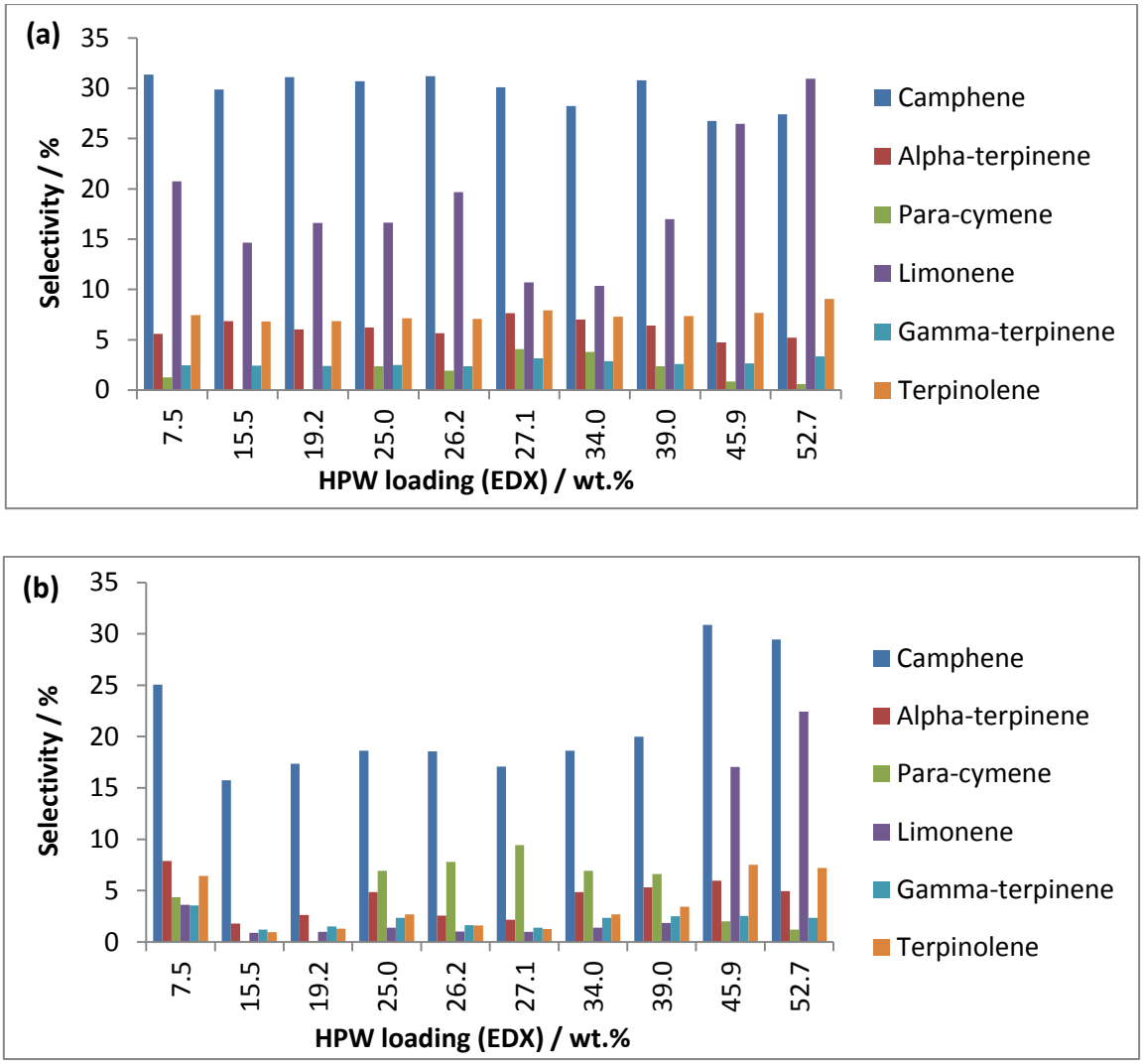

Fig. 66 Selectivities of HPW catalysts on SBA-15 after (a) four and (b) 23 hours of reaction.

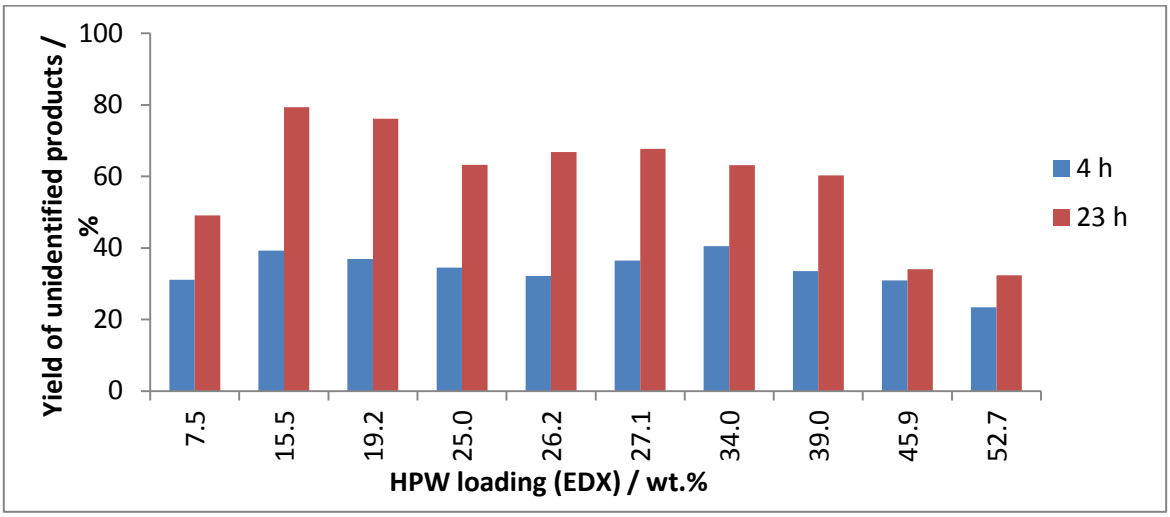

Fig. 67 Percentage of total alpha-pinene conversion by HPW catalysts on SBA-15 that cannot be attributed to products of known identity (see Fig. 66), after four and 23 hours of reaction.

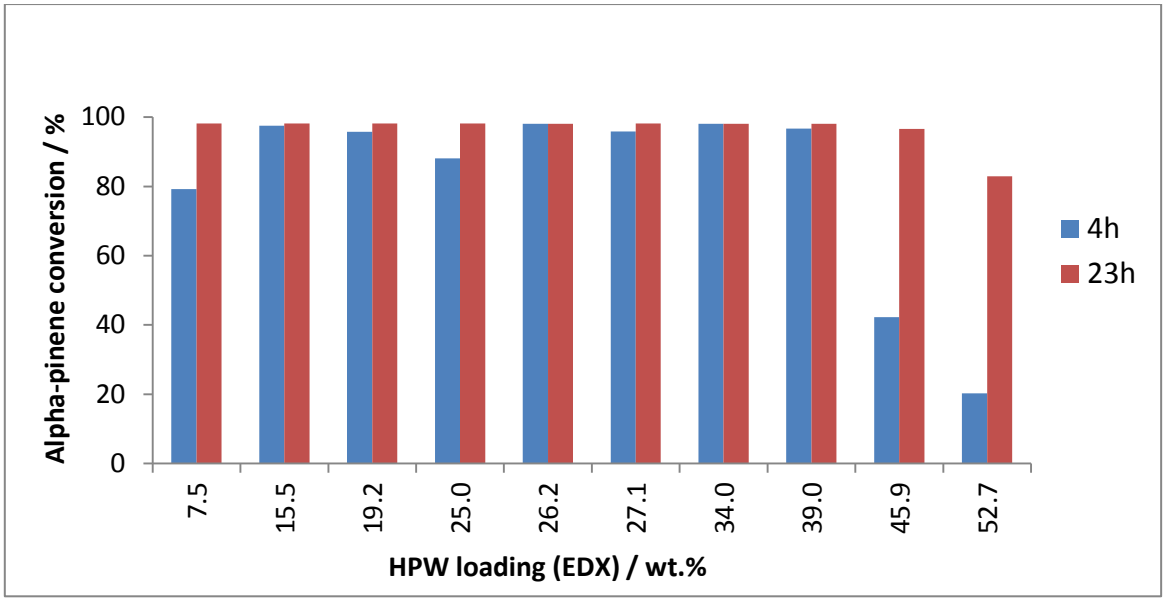

Fig. 68 Total alpha-pinene conversion by HPW catalysts on SBA-15 after four and 23 hours of reaction.

As shown in Fig. 69, most catalysts generate more camphene than limonene in the initial stages of reaction. Limonene selectivities are typically in the range 20 – 25 %, whereas camphene selectivities lie between 25 and 35 %. On all supports, camphene selectivity is highest at a HPW loading of 20 – 40 wt.% and decreases sharply if the loading increases beyond this point. In contrast, limonene selectivity is low at intermediate loadings and reaches a maximum value at the highest HPW loadings studied. It is interesting that camphene production is disfavoured, and limonene production enhanced, at loadings where (according to XPS and porosimetry measurements) monolayer HPW deposition is complete. This result could indicate that the acid strength of HPW is reduced by direct contact with the support, and significantly increases upon formation of multilayer, non-interfacial deposits.

While evidently influenced by HPW loading, selectivity appears to be only moderately dependent on the choice of support. There is some evidence to suggest that selectivity is less variable on fumed silica than on the other supports: measurements are clustered within a smaller range, and changes with loading (particularly at high loadings) are far less pronounced. It may also be noted that, while limonene selectivities vary only weakly between the supports, KIT-6 and SBA-15 exhibit higher maximum selectivities for camphene. These slight differences could indicate that the acid strengths of the fumed silica catalysts are higher, at least at intermediate loadings, due to the larger average particle sizes and greater prevalence of non-interfacial HPW. Such a conclusion is supported by XPS measurements, which indicate that the concentration of interfacial HPW – representing weak acid sites – is consistently low and unvarying across the fumed silica series. In contrast, interfacial

loadings on SBA-15 and KIT-6 are very high when HPW content is low, becoming comparable to the fumed silica value only at bulk loadings exceeding 40 wt.%.

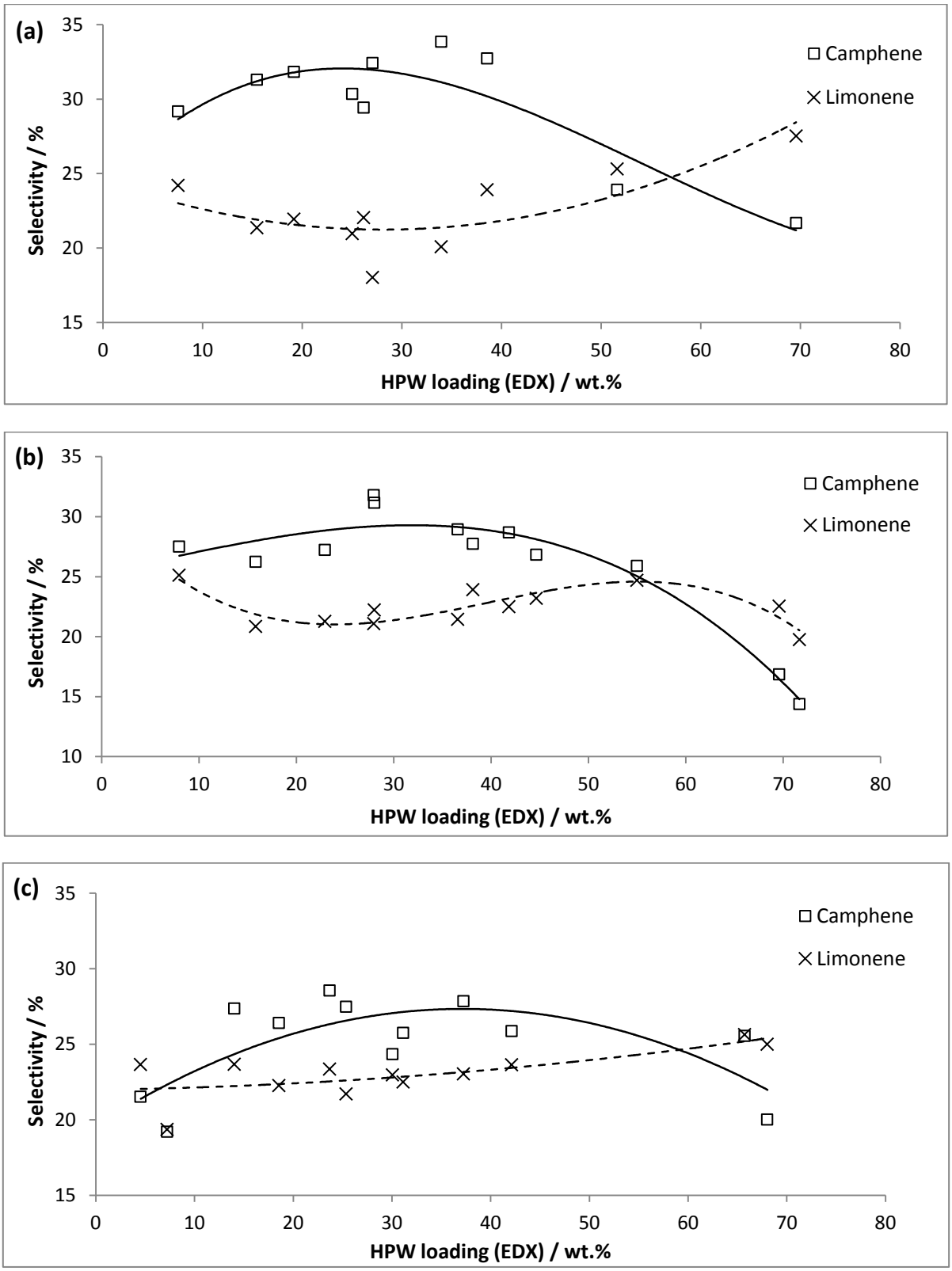

Fig. 69 Selectivities of HPW on (a) SBA-15, (b) KIT-6 and (c) fumed silica.

It should be noted that many of the analyses in this section are based on unreplicated series of measurements, the errors of which are not accurately known. Unfortunately, since repeating the characterisation of each catalyst was not possible within the time constraints of the project, the reliability of the conclusions drawn from such data cannot be fully quantified. Nevertheless, from a limited number of repeat experiments (Table 3 and Fig. 62), the errors in the measurements of k_{raw} may be estimated as 5 – 10% (based on deviations from the mean), with some anomalous deviations in the range 10 – 20%. If the errors in the HPW loadings and NPV_{corr} values are assumed to be as presented in Fig. 27 and Fig. 42 respectively, the errors in k_{area}^{acc} should largely lie in the range 15 – 25 %. Selectivities, meanwhile, are found to exhibit errors mostly below 10% (Table 3). As aforementioned, the uncertainties associated with catalysts with large HPW loadings are likely to be highest, due to their low rates of conversion (per mass of catalyst) and small surface areas.

HPW loading (EDX) / wt.%	**Error in k_{raw} / %**	**Error in camphene selectivity / %**	**Error in limonene selectivity / %**	**Error in k_{area}^{acc} / %**
HPW on SBA-15				
19.2	7.2	3.2	2.0	16.4
25.0	18.7	4.4	0.0	25.3
26.2	2.7	8.8	7.0	14.9
27.1	8.3	6.4	3.4	16.7
38.6	2.9	13.0	9.6	23.4
51.6	15.4	6.0	3.6	37.8
69.6	11.8	7.6	14.4	37.3
HPW on KIT-6				
28.0	1.0	2.1	3.0	12.8
36.6	5.3	4.7	6.6	15.5
HPW on fumed silica				
4.5	2.7	3.5	3.6	10.4
14.0	0.2	1.0	3.0	10.1
18.6	9.0	5.4	4.6	13.6
23.7	4.1	0.6	2.5	10.9

Table 3 Errors in the rate constants and selectivities a subset of silica-supported HPW catalysts, based on duplicate measurements. Errors in the k_{area}^{acc} values are estimated from the measured uncertainties in k_{raw} and HPW loading values, and the estimated errors in NPV_{corr}.

3.8 Catalysts for biodiesel synthesis

In preparation for esterification studies, leaching experiments were conducted on supported HPW and CsPW catalysts. After stirring the materials in methanol for four hours at 60°C, the solutions were filtered and analysed by UV-vis spectroscopy. The solution from the HPW catalyst produced an intense signal due to dissolved HPW, whereas the solution from the CsPW catalyst produced almost no signal (Fig. 70). EDX measurements on a subset of the recovered materials similarly indicate that while the loadings of the HPW catalysts decrease by over 95% after the methanol treatment, the loadings of the CsPW catalysts fall by less than 15% (Table 4). These results are preliminary evidence that supported CsPW catalysts may be suitable for use in biodiesel synthesis, and that caesium-doping (or a comparable treatment) is necessary to avoid leaching effects. Interestingly, this conclusion directly contradicts a number of reports in the literature claiming that silica-supported HPW can be used as a recyclable catalyst for esterification reactions.[37, 66-68]

Alpha-pinene isomerisation tests indicate that the CsPW catalysts retain some of the catalytic activity of HPW, even though the majority of acidic sites are lost during salt formation (Fig. 71). Interestingly, whereas *TOF* values for the HPW catalysts appear to decrease linearly as loading increases, the CsPW catalysts exhibit a linear increase. Values of k_{mass} display a similar trend. It is possible that pore blocking affects all of the catalysts in this series similarly, so adding more catalyst increases the number of accessible catalytic sites. The increase in *TOF* with loading may suggest that the activity per catalytic site scales with loading, but it could also be an artefact resulting from an error in *W*, as described previously.

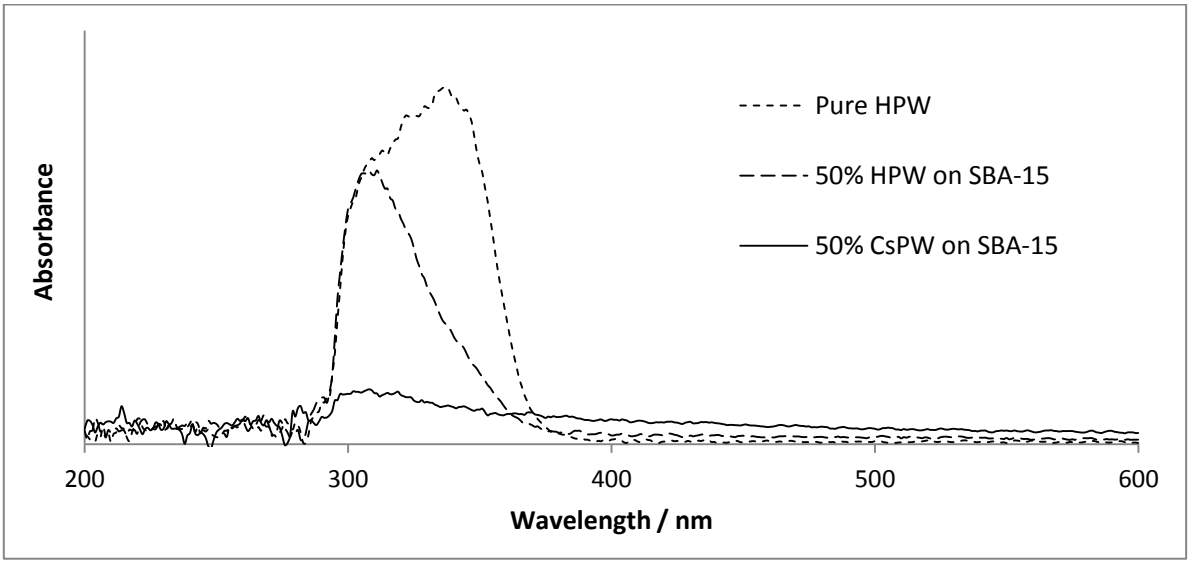

Fig. 70 UV-vis spectra of solutions produced by stirring HPW and CsPW catalysts in methanol at 60°C for four hours.

	HPW loading before wash/ wt.%	HPW Loading after wash / wt.%	Percentage HPW leached / %
HPW on SBA-15	33.95	0.84	98
	15.45	0.45	97
	7.54	0.32	96
CsPW on SBA-15	34.68	29.81	14
	34.68	32.62	6
	34.68	30.11	13
	12.49	11.70	6

Table 4 EDX measurements of HPW and CsPW catalysts before and after stirring in methanol at 60°C for four hours, illustrating the variation in leaching between the two series.

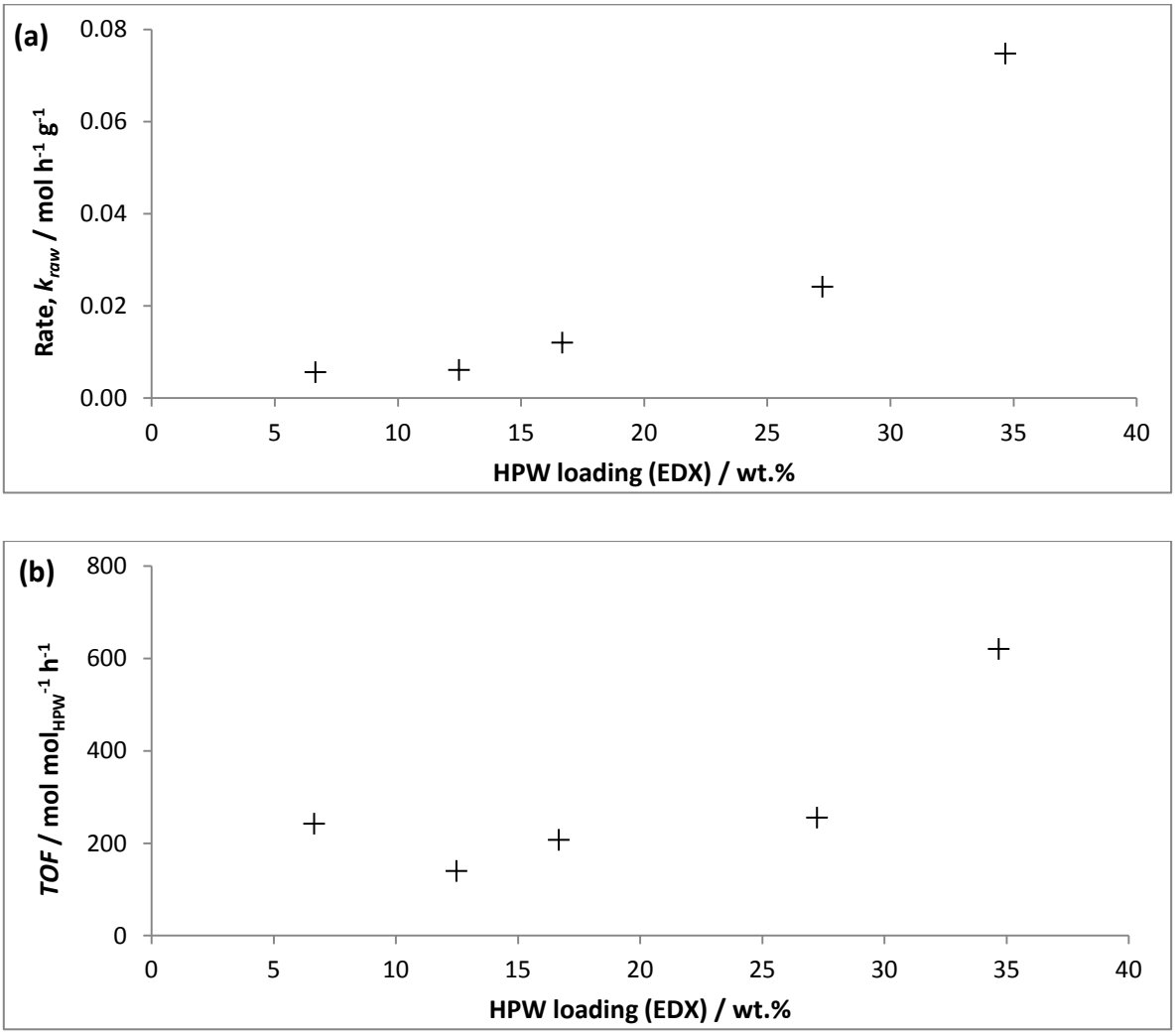

Fig. 71 (a) Rates (k_{raw}) and (b) turnover frequencies (*TOF*) of alpha-pinene isomerisation reactions catalysed by CsPW on SBA-15.

Intriguingly, the selectivity profiles of the CsPW catalysts differ significantly from those described above (Fig. 72). Yields of both limonene and camphene increase with loading and appear to approach a maximum near 30 wt.%. However, the selectivities are consistently lower than the comparable values for the supported HPW catalysts: limonene yields range from 6 to 18%, and camphene yields from 6 to 25%. It is possible that the materials are more strongly acidic than the HPW catalysts, so more readily convert alpha-pinene to monocyclic end-products such as para-cymene. Alternatively, the catalysts may facilitate other reaction routes such as polymerisation. Unfortunately, quantifying the concentrations of minor products proved difficult for this catalyst series, owing to their relatively low rates of conversion. To fully explain the observed selectivities, therefore, additional reaction testing would be required.

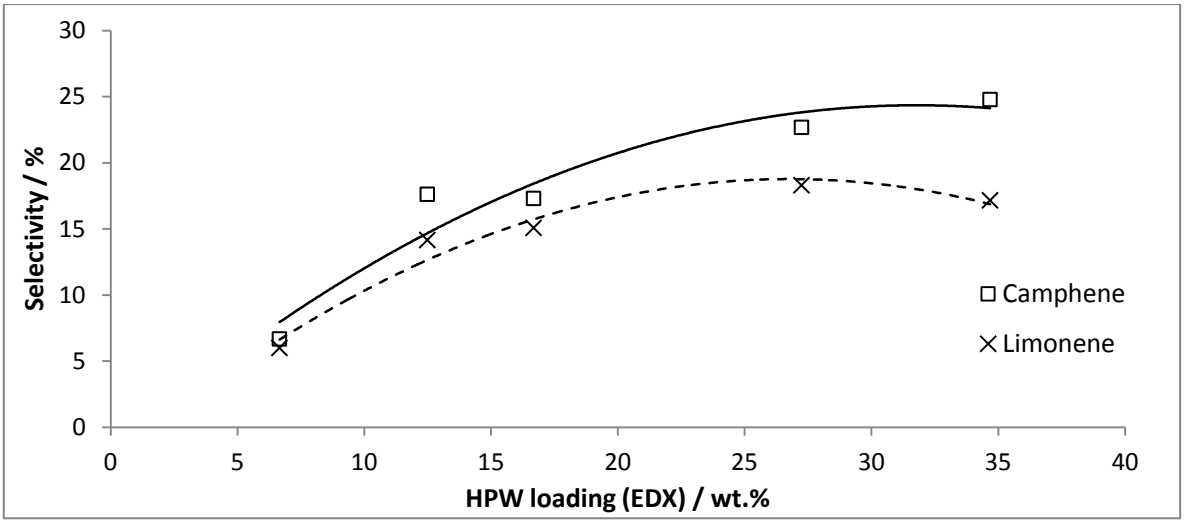

Fig. 72 Selectivities of CsPW catalysts on SBA-15.

4. Conclusions

Heteropoly acids (HPAs) are among the most promising heterogeneous catalysts for the manufacture of biofuels, due to their low cost, strong acidity and stability under a range of reaction conditions. To maximise their surface area and protect against leaching effects, solid HPAs are commonly dispersed onto materials with a high degree of porosity, such as the ordered silicas SBA-15 and KIT-6. Previous studies have investigated the catalytic properties of HPAs on a wide variety of supports.[37, 42, 47, 48, 94] However, there have been few attempts to quantify the variation in activity as a function of physical parameters such as surface area, pore volume and catalyst loading. The aim of this investigation was to analyse the influence of different silica supports on the performance of a common HPA catalyst, 12-phosphotungstic acid (HPW), and thus obtain a model from which the activities of similar supported catalysts may be accurately predicted.

HPW was dispersed on fumed silica and SBA-15 and KIT-6 silicas via a wet impregnation procedure. For each support, at least ten different catalysts were prepared, with loadings (measured by energy-dispersive X-ray spectroscopy, EDX) ranging from 5 to 75 wt.%. Raman and powder X-ray diffraction (PXRD) measurements indicate that impregnation leaves the chemical structure of HPW unchanged: the supported materials produce diffraction lines at the same positions as bulk HPW, and there is no evidence of decomposition products such as tungsten(VI) oxide. Transmission electron microscopy (TEM) images and nitrogen porosimetry measurements also confirm that the ordered pore structures of SBA-15 and KIT-6 remain intact up to HPW loadings of at least 50 wt.%.

The original aim of the project was to develop supported HPW catalysts for the synthesis of biofuels from alcohols and plant oils. However, when the prepared materials were washed with methanol, their catalyst loadings (as measured by EDX) were found to decrease by over 95%. Leaching of HPW was confirmed by UV-vis spectroscopic analysis of the filtered solution. To avoid such effects, the activities of the catalysts were measured in a test reaction involving only non-polar reagents: the acid-promoted isomerisation of neat alpha-pinene. When added to the stirred reaction mixture at 35^{o}C to achieve a concentration of 25 mg ml^{-1}, almost all the catalysts delivered complete conversion of the starting material within six hours. The reactions proceeded with zero-order kinetics for the first 60 - 120 minutes, yielding camphene and limonene as the major products. Monocyclic species, such as para-cymene and alpha-terpinene, and high-molecular-weight compounds (likely oligomers) were favoured at later times.

Conversion of alpha-pinene was monitored by reaction sampling and gas chromatography (GC) analysis. When normalised to the mass of support, the initial reaction rates were found to increase

with HPW content, reaching maximum values between 30 and 40 wt.%. Below loadings of 50 wt.%, the fumed silica catalysts were 1.5 to 3.5 times less active (per mass of catalyst) than the corresponding SBA-15 and KIT-6 materials; however, at high loadings the supports were similarly effective. These differences are unlikely to be attributable to changes in the active species, as little variation was observed in the selectivities of the catalysts or the positions of the major resonances in their Raman spectra. Likewise, inverse gas chromatography (IGC) and thermogravimetric analysis (TGA) data suggest the hydrophobicities and surface silanol concentrations of the pure supports are only marginally dissimilar. It may be deduced that the activity of the catalysts is primarily governed by the geometry of the HPW deposits, the strength of their interaction with the silica support, and the ease with which reactants may access the active species.

It has previously been suggested that HPW is deposited on fumed silica as a monolayer, such that coverage of the support surface reaches a maximal value at a bulk loading of approximately 30 wt.%.[38] The results of this work corroborate these findings, and suggest that HPW exhibits similar behaviour on the ordered mesoporous silicas SBA-15 and KIT-6. Scherrer analysis of PXRD patterns indicate that HPW particles increase in size as the bulk loading on the support is increased, and are considerably larger on fumed silica than on the ordered supports. However, the Scherrer dimensions are in all cases larger than the modal diameters of the support mesopores, as estimated by porosimetry. Furthermore, although the Brunauer-Emmett-Teller (BET) surface areas and Barrett-Joyner-Holenda (BJH) pore volumes of the materials decrease with increasing HPW content, the changes observed between loadings of 20 and 40 wt.% are relatively small. It may be concluded that the measured HPW particle sizes primarily reflect the two-dimensional spread of monolayer "islands" over the support surface. These deposits only weakly affect the area and volume accessible to adsorbates, as their thickness (one Keggin unit, 1.2 nm in diameter) is much less than the diameter of the host pores.

To further investigate the structure of HPW deposits on the silica supports, samples were probed by X-ray photoelectron spectroscopy (XPS), a surface-sensitive technique for compositional analysis. XPS allows the concentration of HPW at the catalyst-support interface to be estimated, as direct interaction between W=O groups and silica leads to a perturbation of the W 4f photoelectron binding energy. XPS data obtained in this study confirm the presence of substantial interfacial deposits on SBA-15 and KIT-6. The absolute interfacial loading increases as total HPW content rises to 35 wt.% but plateaus or falls at higher bulk loadings, where multilayer deposition is expected to predominate. These results provide further evidence that the maximum density of accessible HPW is reached at loadings of 30 - 40 wt.%. However, as only photoelectrons from external particle

surfaces can be detected, measurements from XPS may not be representative of catalyst deposits within the support pores. It must also be noted that the degree of absorption affecting each XPS signal cannot be accurately known, so the observed trends in elemental concentrations are not reliable indicators of the absolute variations in surface composition, contrary to previous reports.[38]

A more direct analysis of the internal HPW deposits is provided by nitrogen porosimetry. Given that the decrease in BJH pore volume with increasing loading far exceeds the volume of HPW added (as estimated from EDX and lattice parameter measurements), it was surmised that the presence of HPW in the pores of the supports must render a fraction of unfilled space inaccessible to adsorbates. This pore blocking effect was quantified by means of a modified normalised pore volume (*NPV*) calculation, in which the pore volume of a catalyst is normalised to the mass of support (estimated by EDX) then expressed as a fraction of the pore volume in the pure support. If the HPW is assumed to be uniformly distributed in the pores, the *NPV* value may be corrected to account for the volume occupied by catalyst deposits. For both the SBA-15 and KIT-6 series, corrected *NPV* values, NPV_{corr}, decrease with increasing HPW content, tending towards a minimum value of approximately 0.3 at the highest catalyst loadings. The pattern of variation at intermediate loadings, however, is different for the two supports: while KIT-6 experiences a monotonous increase in pore blocking with loading, the SBA-15 materials exhibits near-constant NPV_{corr} values in the range 15 - 35 wt.%. The plateau in the SBA-15 profile is consistent with the formation of a HPW monolayer, which the major mesopores can readily accommodate. This effect is not apparent in the KIT-6 series because the pores of the support are more highly connected, so are "cut off" from adsorbates more gradually as blockages develop.

To account for pore-blocking effects and differences in support area, the reaction rate of each catalyst was normalised to the area of support accessible to reagents. The normalisation factor was estimated by multiplying the total mass of catalyst by the silica loading (measured by EDX), the BET surface area of the support (measured by nitrogen porosimetry) and, in the case of the SBA-15 and KIT-6 materials, the NPV_{corr} value. The normalised reaction rates, k_{area}^{acc}, were plotted against the mass of HPW per unit area of support. Strikingly, the plots for the three supports almost exactly converge at HPW loadings below 40 wt.%. Moreover, the increase in reaction rate with HPW loading is approximately linear, indicating that each mole of accessible HPW delivers a constant turnover frequency irrespective of loading. From the gradient of this trend (0.6 mol g_{HPW}^{-1} h^{-1} or 1700 mol mol_{HPW}^{-1} h^{-1}, where the quantity of HPW is that present in accessible pores only) it should be possible to predict the activity of any silica-supported HPW material from simple nitrogen porosimetry and EDX measurements, provided the catalyst loading is sufficiently low.

It is worth emphasising that estimates of pore blocking do not account for the accumulation of multilayer deposits, and are limited in their application to materials containing uniform pores. Though Scherrer analysis of PXRD data indicates that HPW particles on fumed silica may be larger than those on SBA-15 and KIT-6, a lack of quantitative information regarding the geometries of the particles makes it impossible to incorporate this effect into reaction rate calculations. Furthermore, variables neglected in the above analysis may become significant at high loadings or on low-area supports: for example, decreases in camphene yields at loadings above 40 wt.% suggest that acid strength is augmented by multilayer deposition, in agreement with findings in the literature. As a result of these and other limitations, the k_{area}^{acc} values of catalysts with disordered pore structures or high HPW loadings are highly variable, and the reaction rates of such materials cannot be predicted. Nonetheless, it may be noted that, as HPW loading increases, the fumed silica catalysts tend towards a maximum k_{area}^{acc} value of 6.5×10^{-4} mol h^{-1} m^{-2}. Since this value is in excess of all other measured reaction rates, it is reasonable to suppose that it represents the maximum achievable k_{area}^{acc} value for materials of this type: the limit of activity for the saturated HPW monolayer.

Despite contradictory reports in the literature,[37, 66-68] silica-supported HPW catalysts were found to be highly soluble in polar media and therefore unsuitable for use in biodiesel production. However, preliminary experiments have shown that partial replacement of the acidic protons with caesium ions can generate an active catalyst that is far less susceptible to leaching. As catalysts for the isomerisation of alpha-pinene, materials comprising $Cs_2HPW_{12}O_{40}$ (CsPW) and SBA-15 were considerably less effective than the corresponding HPW materials, but their activities were still sufficiently high to deliver complete conversion after six hours. Furthermore, selectivity data suggest that the salts display lower pK_a values than their HPW counterparts, perhaps making them more compatible with reactions in which a strong acid catalyst is required.

Given the expense of manufacturing ordered mesoporous supports, catalysts based on SBA-15 and KIT-6 are unlikely to represent economic alternatives to conventional supported acid catalysts. Nonetheless, by providing a fair and quantitative comparison between chemically similar supported catalysts with varying pore systems, this investigation usefully illustrates how the choice of support may influence catalytic performance. In addition to confirming previous models of HPW deposition on silica,[38] the study has shown that differences in activity can be explained with reference to a simple pore-filling model, wherein plugging of channels causes a fraction of pore space to become inaccessible to adsorbates. Thus, it may now be possible to predict the activity of HPW on a mesoporous silica support from loading and porosimetry measurements alone. Applying a similar analysis to different catalysts and reaction schemes would allow the generality of the model to be

tested, and produce normalised measurements from which the effects of other physical variables – such as the acidity of the support material or shape of the pore channel – might be more accurately gauged.

5. Further work

Catalytic testing in this investigation was, in most cases, limited to a single reaction under a fixed set of conditions. To evaluate the susceptibility of the catalysts to leaching or degeneration, samples could be extracted from the reaction mixture, washed with a non-polar solvent, and reused in further trials. For catalysts with low activities per gram (such as those with very high loadings), the reactions could also be repeated with larger masses of catalyst to minimise the error in the measurements of initial rate. Repeating the reaction trials would further allow the standard errors of the data to be determined, such that the reliability of the trends in catalytic performance might be quantitatively assessed.

Thermodynamic analysis of the alpha-pinene isomerisation might also be useful. Varying the temperature of the reaction would allow for the construction of Arrhenius plots, from which estimates of the activation energy may be derived. These data could be correlated against measurements of acid strength, obtained by means of Hammett indicators or ammonia desorption experiments, in order to more fully explain the variation in selectivity with increasing HPW loading. Base titration experiments could also be used to quantify the surface concentrations of accessible acid sites, against which reaction rates might be normalised to evaluate the absolute turnover frequencies of the supported catalysts.[15, 38]

Silica-supported HPW catalysts were found to be unsuitable for use in biodiesel production due to their susceptibility to leaching in polar solvents. To address this problem, a small number of supported caesium salts of HPW were prepared. To further evaluate their usefulness, a larger series of materials should be generated, with differing loadings and Cs/HPW ratios, and tested as catalysts for esterification and transesterification reactions. The support and substrate could be varied to investigate the effect of pore structure on activity and recyclability. Smaller pores, for example, might be expected to experience more extensive blockage by catalyst particles, or less rapid diffusion of bulky reagents. It could also be worthwhile exploring, by means of detailed TEM and porosimetry experiments, how CsPW and HPW differ in their modes of deposition. PXRD and XPS experiments in this investigation indicate that CsPW forms larger particles and fewer interfacial deposits on silica supports, but further studies are needed to determine the generality of these results.

A major outcome of this investigation is the discovery that differences between silica-supported HPW catalysts can be quantitatively predicted from measurements of porosity and composition. Analysing other series of supported catalysts would allow the general applicability of this approach

to be tested. Where the model is found to break down, it could be extended by incorporating measurements of other significant factors. In particular, catalyst dispersions might be estimated from titration experiments, and accurate particle sizes obtained by analysis of high-resolution TEM images. Ultimately, the aim would be to construct, for a given supported catalyst, a formula describing the impact of all important solid-state parameters on catalytic activity.

6. References

1. Y. Izumi, K. Urabe and M. Onaka, *Zeolite, clay, and heteropoly acid in organic reactions*, Kodansha, 1992.
2. M. N. Timofeeva, *Appl. Catal. A-Gen.*, 2003, **256**, 19-35.
3. I. K. Song, M. S. Kaba and M. A. Barteau, *Langmuir*, 2002, **18**, 2358-2362.
4. J. F. Keggin, *Proc. R. soc. Lond. Ser. A-Contain. Pap. Math. Phys. Character*, 1934, **144**, 0075-0100.
5. G. M. Brown, M. R. Noe-Spirlet, W. R. Busing and H. A. Levy, *Acta Crystallogr. Sect. B-Struct. Commun.*, 1977, **33**, 1038-1046.
6. P. S. N. Rao, K. T. Venkateswara Rao, P. S. Sai Prasad and N. Lingaiah, *Catal. Commun.*, 2010, **11**, 547-550.
7. V. W. Godói Silva, L. O. Laier and M. J. da Silva, *Catal. Lett.*, 2010, **135**, 207-211.
8. T. Okuhara, M. Kimura and T. Nakato, *Appl. Catal. A-Gen.*, 1997, **155**, L9-L13.
9. T. Nakato, Y. Toyoshi, M. Kimura and T. Okuhara, *Catal. Today*, 1999, **52**, 23-28.
10. Z. Y. Hou and T. Okuhara, *Chem. Commun.*, 2001, 1686-1687.
11. M. T. Pope, *Heteropoly and isopoly oxometalates*, Springer-Verlag, 1983.
12. S. Zullaikah, C. C. Lai, S. R. Vali and Y. H. Ju, *Bioresour. Technol.*, 2005, **96**, 1889-1896.
13. J. H. Clark and D. J. Macquarrie, *Handbook of Green Chemistry and Technology*, Wiley, 2002.
14. T. Nakato, M. Kimura, S. Nakata and T. Okuhara, *Langmuir*, 1998, **14**, 319-325.
15. K. Narasimharao, D. R. Brown, A. F. Lee, A. D. Newman, P. F. Siril, S. J. Tavener and K. Wilson, *J. Catal.*, 2007, **248**, 226-234.
16. J. S. Santos, J. A. Dias, S. C. L. Dias, F. A. C. Garcia, J. L. Macedo, F. S. G. Sousa and L. S. Almeida, *Appl. Catal. A-Gen.*, 2011, **394**, 138-148.
17. J. Haber, K. Pamin, L. Matachowski, B. Napruszewska and J. Poltowicz, *J. Catal.*, 2002, **207**, 296-306.
18. L. R. Pizzio and M. N. Blanco, *Microporous Mesoporous Mat.*, 2007, **103**, 40-47.
19. L. Pesaresi, D. R. Brown, A. F. Lee, J. M. Montero, H. Williams and K. Wilson, *Appl. Catal. A-Gen.*, 2009, **360**, 50-58.
20. C. Pazé, S. Bordiga and A. Zecchina, *Langmuir*, 2000, **16**, 8139-8144.
21. A. Bielański, J. Datka, B. Gil, A. Malecka-Lubańska and A. Micek-Ilnicka, *Catal. Lett.*, 1999, **57**, 61-64.
22. A. Micek-Ilnicka, *J. Mol. Catal. A-Chem.*, 2009, **308**, 1-14.
23. G. J. Kearley, R. P. White, C. Forano and R. C. T. Slade, *Spectroc. Acta Pt. A-Molec. Biomolec. Spectr.*, 1990, **46**, 419-424.
24. S. Ganapathy, M. Fournier, J. F. Paul, L. Delevoye, M. Guelton and J. P. Amoureux, *J. Am. Chem. Soc.*, 2002, **124**, 7821-7828.
25. V. Z. Sasca, O. Verdes, L. Avram, A. Popa, A. Erdőhelyi and A. Oszko, *Appl. Catal. A-Gen.*, 2013, **451**, 50-57.
26. G. Mestl, T. Ilkenhans, D. Spielbauer, M. Dieterle, O. Timpe, J. Kröhnert, F. Jentoft, H. Knözinger and R. Schlögl, *Appl. Catal. A-Gen.*, 2001, **210**, 13-34.
27. L. Matachowski, A. Drelinkiewicz, E. Lalik, D. Mucha, B. Gil, Z. Brożek-Mucha and Z. Olejniczak, *Microporous Mesoporous Mat.*, 2011, **144**, 46-56.
28. G. Chen, C.-Y. Guo, X. Zhang, Z. Huang and G. Yuan, *Fuel Process. Technol.*, 2011, **92**, 456-461.
29. S. van Donk, A. H. Janssen, J. H. Bitter and K. P. de Jong, *Catal. Rev.-Sci. Eng.*, 2003, **45**, 297-319.
30. T. F. Degnan, *J. Catal.*, 2003, **216**, 32-46.
31. V. P. Zhdanov and B. Kasemo, *Catal. Lett.*, 1998, **50**, 131-134.
32. M. O. Coppens and G. F. Froment, *Chem. Eng. Sci.*, 1995, **50**, 1027-1039.
33. J. Grumelard, A. Taubert and W. Meier, *Chem. Commun.*, 2004, 1462-1463.

34. Z. H. Dai and H. X. Ju, *Trac-Trends Anal. Chem.*, 2012, **39**, 149-162.
35. D. Y. Zhao, J. L. Feng, Q. S. Huo, N. Melosh, G. H. Fredrickson, B. F. Chmelka and G. D. Stucky, *Science*, 1998, **279**, 548-552.
36. F. Kleitz, S. H. Choi and R. Ryoo, *Chem. Commun.*, 2003, 2136-2137.
37. C. S. Caetano, I. M. Fonseca, A. M. Ramos, J. Vital and J. E. Castanheiro, *Catal. Commun.*, 2008, **9**, 1996-1999.
38. A. D. Newman, D. R. Brown, P. Siril, A. F. Lee and K. Wilson, *PCCP Phys. Chem. Chem. Phys.*, 2006, **8**, 2893-2902.
39. F. Jing, B. Katryniok, E. Bordes-Richard and S. Paul, *Catal. Today*, 2013, **203**, 32-39.
40. J. Zhang, M. Kanno, Y. Wang, H. Nishii, Y.-k. Miura and Y. Kamiya, *J. Phys. Chem. C*, 2011, **115**, 14762-14769.
41. E. Rafiee and S. Eavani, *J. Mol. Catal. A-Chem.*, 2013, **373**, 30-37.
42. L. R. Pizzio, C. V. Caceres and M. N. Blanco, *Appl. Catal. A-Gen.*, 1998, **167**, 283-294.
43. L. R. Pizzio, C. V. Caceres and M. N. Blanco, *Appl. Surf. Sci.*, 1999, **151**, 91-101.
44. C. Yuan and J. Chen, *Chin. J. Catal.*, 2011, **32**, 1191-1198.
45. D. P. Sawant, A. Vinu, N. E. Jacob, F. Lefebvre and S. B. Halligudi, *J. Catal.*, 2005, **235**, 341-352.
46. A. Taguchi and F. Schüth, *Microporous Mesoporous Mat.*, 2005, **77**, 1-45.
47. C. F. Shi, R. W. Wang, G. S. Zhu, S. L. Qiu and J. Long, *Eur. J. Inorg. Chem.*, 2005, 4801-4807.
48. V. Dufaud, F. Lefebvre, G. P. Niccolai and M. Aouine, *J. Mater. Chem.*, 2009, **19**, 1142-1150.
49. Y. M. Luo, Z. Y. Hou, R. T. Li and X. M. Zheng, *Microporous Mesoporous Mat.*, 2008, **109**, 585-590.
50. Y. Izumi, M. Ono, M. Kitagawa, M. Yoshida and K. Urabe, *Microporous Mater.*, 1995, **5**, 255-262.
51. J. M. Tatibouët, C. Montalescot, K. Brückman, J. Haber and M. Che, *J. Catal.*, 1997, **169**, 22-32.
52. A. S. Tipnis, D. K. Deodhar and S. D. Samant, *Indian J. Chem. Sect B-Org. Chem. Incl. Med. Chem.*, 2010, **49**, 340-345.
53. N. Scarlat, J. F. Dallemand and M. Banja, *Renewable and Sustainable Energy Reviews*, 2013, **18**, 595-606.
54. J. Janaun and N. Ellis, *Renewable and Sustainable Energy Reviews*, 2010, **14**, 1312-1320.
55. L. Azócar, G. Ciudad, H. J. Heipieper and R. Navia, *Appl. Microbiol. Biotechnol.*, 2010, **88**, 621-636.
56. A. I. Bamgboye and A. C. Hansen, *Int. Agrophys.*, 2008, **22**, 21-29.
57. D. Y. C. Leung and Y. Guo, *Fuel Process. Technol.*, 2006, **87**, 883-890.
58. F. R. Ma and M. A. Hanna, *Bioresour. Technol.*, 1999, **70**, 1-15.
59. S. Glišić, I. Lukic and D. Skala, *Bioresour. Technol.*, 2009, **100**, 6347-6354.
60. S. Baroutian, M. K. Aroua, A. A. Raman and N. M. Sulaiman, *Bioresour. Technol.*, 2011, **102**, 1095-1102.
61. J. A. Melero, J. Iglesias and G. Morales, *Green Chem.*, 2009, **11**, 1285-1308.
62. M. K. Lam, K. T. Lee and A. R. Mohamed, *Biotechnol. Adv.*, 2010, **28**, 500-518.
63. K. Suwannakarn, E. Lotero, J. G. Goodwin and C. Q. Lu, *J. Catal.*, 2008, **255**, 279-286.
64. J. M. Marchetti, V. U. Miguel and A. F. Errazu, *Fuel Process. Technol.*, 2008, **89**, 740-748.
65. A. H. West, D. Posarac and N. Ellis, *Bioresour. Technol.*, 2008, **99**, 6587-6601.
66. V. Brahmkhatri and A. Patel, *Appl. Catal. A-Gen.*, 2011, **403**, 161-172.
67. A. I. Tropecêlo, M. H. Casimiro, I. M. Fonseca, A. M. Ramos, J. Vital and J. E. Castanheiro, *Appl. Catal. A-Gen.*, 2010, **390**, 183-189.
68. D. P. Sawant, A. Vinu, S. P. Mirajkar, F. Lefebvre, K. Ariga, S. Anandan, T. Mori, C. Nishimura and S. B. Halligudi, *J. Mol. Catal. A-Chem.*, 2007, **271**, 46-56.
69. A. D. Newman, A. F. Lee, K. Wilson and N. A. Young, *Catal. Lett.*, 2005, **102**, 45-50.
70. M. A. Ecormier, K. Wilson and A. F. Lee, *J. Catal.*, 2003, **215**, 57-65.

71. B. Atalay and G. Gündüz, *Chem. Eng. J.*, 2011, **168**, 1311-1318.
72. K. A. D. Rocha, P. A. Robles-Dutenhefner, I. V. Kozhevnikov and E. V. Gusevskaya, *Appl. Catal. A-Gen.*, 2009, **352**, 188-192.
73. M. Zabeti, W. Daud and M. K. Aroua, *Fuel Process. Technol.*, 2009, **90**, 770-777.
74. V. Meynen, Y. Segura, M. Mertens, P. Cool and E. F. Vansant, *Microporous Mesoporous Mat.*, 2005, **85**, 119-128.
75. S. Chytil, L. Haugland and E. A. Blekkan, *Microporous Mesoporous Mat.*, 2008, **111**, 134-142.
76. J. W. Beeckman and G. F. Froment, *Industrial & Engineering Chemistry Fundamentals*, 1979, **18**, 245-256.
77. T. Mochizuki, D. Atong, S. Y. Chen, M. Toba and Y. Yoshimura, *Catal. Commun.*, 2013, **36**, 1-4.
78. M. Zheng, S. L. Chen, J. H. Zhang, Y. Liu, L. Sang, J. You and X. D. Wang, *Pet. Sci.*, 2013, **10**, 112-119.
79. L. Pinard, S. Hamieh, C. Canaff, F. F. Madeira, I. Batonneau-Gener, S. Maury, O. Delpoux, K. Ben Tayeb, Y. Pouilloux and H. Vezin, *J. Catal.*, 2013, **299**, 284-297.
80. S. van Donk, J. H. Bitter and K. P. de Jong, *Appl. Catal. A-Gen.*, 2001, **212**, 97-116.
81. P. Forzatti and L. Lietti, *Catal. Today*, 1999, **52**, 165-181.
82. M. Bonne, S. Pronier, F. Can, X. Courtois, S. Valange, J. M. Tatibouët, S. Royer, P. Marécot and D. Duprez, *Solid State Sci.*, 2010, **12**, 1002-1012.
83. S. Lowell, *Characterization of Porous Solids and Powders: Surface Area, Pore Size and Density*, Springer, 2004.
84. T. M. Eggenhuisen, J. Zečević, H. Talsma, K. P. de Jong and P. E. de Jongh, *J. Phys. Chem. C*, 2012, **116**, 7480-7490.
85. K. Morishige, H. Yasunaga, R. Denoyel and V. Wernert, *J. Phys. Chem. C*, 2007, **111**, 9488-9495.
86. J. Riikonen, J. Salonen, M. Kemell, N. Kumar, D. Y. Murzin, M. Ritala and V. P. Lehto, *J. Phys. Chem. C*, 2009, **113**, 20349-20354.
87. M. Baca, E. de la Rochefoucauld, E. Ambroise, J. M. Krafft, R. Hajjar, P. P. Man, X. Carrier and J. Blanchard, *Microporous Mesoporous Mat.*, 2008, **110**, 232-241.
88. M. V. Landau, L. Vradman, A. Wolfson, P. M. Rao and M. Herskowitz, *C. R. Chim.*, 2005, **8**, 679-691.
89. A. Zukal, H. Šiklová and J. Čejka, *Langmuir*, 2008, **24**, 9837-9842.
90. L. Vradman, M. V. Landau, M. Herskowitz, V. Ezersky, M. Talianker, S. Nikitenko, Y. Koltypin and A. Gedanken, *J. Catal.*, 2003, **213**, 163-175.
91. M. O. Coppens, *Catal. Today*, 1999, **53**, 225-243.
92. H. Friedrich, J. R. A. Sietsma, P. E. de Jongh, A. J. Verkleij and K. P. de Jong, *J. Am. Chem. Soc.*, 2007, **129**, 10249-10254.
93. A. H. Janssen, C. M. Yang, Y. Wang, F. Schüth, A. J. Koster and K. P. de Jong, *J. Phys. Chem. B*, 2003, **107**, 10552-10556.
94. E. Rafiee, S. Eavani, S. Rashidzadeh and M. Joshaghani, *Inorganica Chimica Acta*, 2009, **362**, 3555-3562.
95. P. Carniti, A. Gervasini, S. Biella and A. Auroux, *Chem. Mat.*, 2005, **17**, 6128-6136.
96. R. E. Dinnebier and S. J. L. Billinger, *Powder Diffraction: Theory and Practice*, Royal Society of Chemistry, 2008.
97. Y. Waseda, E. Matsubara and K. Shinoda, *X-Ray Diffraction Crystallography: Introduction, Examples and Solved Problems*, Springer Berlin Heidelberg, 2011.
98. C. Suryanarayana and G. Norton, *X-Ray Diffraction: A Practical Approach*, Springer, 1998.
99. A. A. Coelho, *J. Appl. Crystallogr.*, 2003, **36**, 86-95.
100. M. U. Cohen, *Rev. Sci. Instrum.*, 1935, **6**, 68-74.
101. G. Spinolo and F. Maglia, *Powder Diffr.*, 1999, **14**, 208-212.
102. C. Dong, F. Wu and H. Chen, *J. Appl. Crystallogr.*, 1999, **32**, 850-853.

103. K. Brandenburg, W. Richter, M. H. J. Koch, H. W. Meyer and U. Seydel, *Chem. Phys. Lipids*, 1998, **91**, 53-69.
104. K. Schumacher, P. I. Ravikovitch, A. Du Chesne, A. V. Neimark and K. K. Unger, *Langmuir*, 2000, **16**, 4648-4654.
105. L. Vradman, L. Titelman and M. Herskowitz, *Microporous Mesoporous Mat.*, 2006, **93**, 313-317.
106. D. C. Bell and A. J. Garratt-Reed, *Energy Dispersive X-ray Analysis in the Electron Microscope*, BIOS, 2003.
107. P. van der Heide, *X-ray Photoelectron Spectroscopy: An Introduction to Principles and Practices*, Wiley, 2011.
108. L. F. Wang and R. T. Yang, *J. Phys. Chem. C*, 2011, **115**, 21264-21272.
109. I. G. Shenderovich, G. Buntkowsky, A. Schreiber, E. Gedat, S. Sharif, J. Albrecht, N. S. Golubev, G. H. Findenegg and H. H. Limbach, *J. Phys. Chem. B*, 2003, **107**, 11924-11939.
110. A. T. Hubbard, in *Encyclopedia of Surface and Colloid Science*, CRC Press, 2002, pp. 2842-2855.
111. *Advanced instrumentation for the characterisation of particulates, fibres and thin-films*, http://www.thesorptionsolution.com/files/IGC%20Brochure%202002.pdf, Surface Measurement Systems, 2002.
112. M. Ruckriem, A. Inayat, D. Enke, R. Glaser, W. D. Einicke and R. Rockmann, *Colloid Surf. A-Physicochem. Eng. Asp.*, 2010, **357**, 21-26.
113. Y. C. Yang and P. R. Yoon, *Mater. Trans.*, 2007, **48**, 1548-1553.
114. C. Liu and Q. Zhao, *Langmuir*, 2011, **27**, 9512-9519.
115. A. J. Bridgeman, *Chem. Phys.*, 2003, **287**, 55-69.
116. A. Popa, V. Sasca and I. Holclajtner-Antunović, *Microporous Mesoporous Mat.*, 2012, **156**, 127-137.
117. C. W. Hu, M. Hashimoto, T. Okuhara and M. Misono, *J. Catal.*, 1993, **143**, 437-448.
118. J. M. R. Gallo, C. Bisio, G. Gatti, L. Marchese and H. O. Pastore, *Langmuir*, 2010, **26**, 5791-5800.